UNIVERSIDAD POLITÉCNICA DE MADRID
Escuela Técnica Superior de Ingeniería Aeronáutica y del Espacio

New Methods for Co-orbital Modelling and Periodic Orbit Design

DOCTORAL THESIS

Submitted for the degree of Doctor by:

Alicia Martínez Cacho
Master's Degree in Aeronautical Engineering

Madrid, 2025

UNIVERSIDAD POLITÉCNICA DE MADRID
Escuela Técnica Superior de Ingeniería Aeronáutica y del Espacio

Doctoral Degree in Aerospace Engineering

New Methods for Co-orbital Modelling and Periodic Orbit Design

D O C T O R A L T H E S I S

Submitted for the degree of Doctor by:

Alicia Martínez Cacho
Master's Degree in Aeronautical Engineering

Under the supervision of:
Dr. Claudio Bombardelli

Madrid, 2025

Title: New Methods for Co-orbital Modelling and Periodic Orbit Design

Author: Alicia Martínez Cacho

Doctoral Programme: Aerospace Engineering

Thesis Supervision:

Dr. Claudio Bombardelli, Associate Professor, Universidad Politécnica de Madrid (Supervisor)

External Reviewers:

Thesis Defense Committee:

Thesis Defense Date:

"This thesis has been partially supported by Universidad Politécnica de Madrid through Programa Propio 2020"

A la memoria de mi madre

Acknowledgement

I would like to thank Claudio Bombardelli, my thesis advisor, for the opportunity to pursue this PhD and his guidance throughout this work. I am also grateful to Prof. Kathleen Howell and all the members of her research group for hosting me and for their support during my research stay at Purdue University.

Abstract

The increasing interest in deep space exploration has placed planetary moons at the forefront of several recent and upcoming space missions, such as MMX, JUICE, Europa Clipper, and Dragonfly, which are set to conduct close-range operations around the moons of Mars, Jupiter and Saturn. Among these bodies, Mars' Phobos, Jupiter's Europa, and Saturn's Titan stand out as promising targets for investigating the origins of the Solar System and assessing conditions for habitability. To support these objectives, quasi-satellite orbits (QSOs), also known as distant retrograde orbits (DRO), have emerged as ideal candidates for extended scientific exploration. These orbits are a type of co-orbital motion formed by periodic solutions to the restricted three-body problem and are characterized by retrograde motion and higher stability relative to other periodic orbits in this dynamical model. Despite their relevance, certain aspects of QSOs, particularly asymmetric QSOs and resonant periodic solutions, have received limited attention in the literature.

This dissertation aims to advance the modeling and understanding of QSOs within three different frameworks: the elliptic restricted three-body problem (ER3BP), the circular restricted three-body problem (CR3BP) and the Hill three-body problem (H3BP). The study covers a wide range of planetary systems of current scientific interest, namely Mars–Phobos, Sun–Mars, Jupiter–Europa, and Saturn–Titan. Moreover, an innovative aspect of this work is the use of curvilinear coordinates, specifically cylindrical coordinates, in the modeling of the three-body problem, in order to leverage their inherent curvature to better match that of orbital trajectories, following insights from previous investigations in other areas of astrodynamics.

The work first evaluates the use of curvilinear coordinates in the two-body relative motion by deriving a solution to a linearized model analogous to the classical Yamanaka-Ankersen solution. The resulting state transition matrix on cylindrical coordinates is then compared with its Cartesian counterpart in uncertainty propagation applications, demonstrating improved realism for typical spacecraft configurations, especially in cases of limited eccentricity. Building on this foundation, a set of differential corrector techniques is derived and implemented for the continuation of periodic orbits in the CR3BP and ER3BP using cylindrical coordinates.

A comprehensive characterization of planar periodic QSO and their families is performed within both the CR3BP and H3BP models. This includes a geometrical classification based on symmetry properties and topological features, as well as an analysis of their relation to each family multiplicity. The study also assesses the differences between these families in the CR3BP and the H3BP and how the latter can be utilized in the understanding and computation of QSOs in the more complex CR3BP. In this sense, a key finding is the different bifurcation behaviors of the families composed of asymmetric QSOs in the two models, which represents one of the main contributions of this work.

In the context of the ER3BP, a global numerical search is conducted to identify and classify periodic resonant QSOs across the selected planetary systems. This classification extends that of the circular case by incorporating additional geometrical features and organizing solutions by resonance triplets. The influence of key system parameters, such as orbital eccentricity and

mass ratio, is examined, revealing bifurcation phenomena, including fold bifurcations, which affect the transition of some QSOs to the ER3BP. Furthermore, in the CR3BP, the mass ratio limits the existence of asymmetric QSOs, since it influences the origin of asymmetric families and the period range they span.

Resumen

El creciente interés por la exploración del espacio profundo ha situado a las lunas planetarias en el punto de mira de numerosas misiones recientes y futuras, como MMX, JUICE, Europa Cliper y Dragonfly, diseñadas para operar en las inmediaciones de las lunas de Marte, Júpiter y Saturno. Entre estos cuerpos, Fobos (Marte), Europa (Júpiter) y Titán (Saturno) destacan como objetivos prometedores para el estudio de los orígenes del Sistema Solar y de las condiciones necesarias para la habitabilidad. Para esto, las órbitas cuasisatélite (QSO), también conocidas como orbitas retrógradas distantes (DRO), han surgido como candidatas idóneas para la exploración científica prolongada. Estas órbitas son soluciones periódicas co-orbitales del problema restringido de los tres cuerpos, con un movimiento retrógrado y mayor estabilidad que otras órbitas del mismo modelo. No obstante, pese a su relevancia, ciertos aspectos de las QSO, en particular las órbitas asimétricas y las soluciones periódicas resonantes, han recibido escasa atención en la literatura.

Esta tesis tiene como objetivo avanzar en la modelización y la comprensión de las QSO en tres modelos dinámicos distintos: el problema restringido de los tres cuerpos elíptico (ER3BP), el circular (CR3BP) y el problema de Hill de los tres cuerpos (H3BP). El estudio abarca varios sistemas planetarios de gran interés científico: Marte-Fobos, Sol-Marte, Júpiter-Europa y Saturno-Titán. Además, un aspecto innovador de este trabajo es el uso de coordenadas curvilíneas, específicamente cilíndricas, para la formulación del problema de los tres cuerpos, con la intención de aprovechar su curvatura inherente para adaptarse mejor a la curvatura de las trayectorias orbitales, siguiendo indicios obtenidos en estudios previos en otras áreas de la astrodinámica.

En primer lugar, se estudia el uso de coordenadas curvilíneas en el movimiento relativo del problema de los dos cuerpos, mediante una solución linealizada análoga a la solución clásica de Yamanaka-Ankersen. La matriz de transición de estado resultante en coordenadas cilíndricas se compara con su equivalente cartesiano en tareas de propagación de incertidumbre, mostrando un mayor realismo en configuraciones típicas de vehículos espaciales, especialmente en casos de excentricidad moderada. Sobre esta base, se implementan técnicas numéricas para la continuación de órbitas periódicas tanto en el CR3BP como en el ER3BP, empleando coordenadas cilíndricas.

A continuación, se realiza una caracterización detallada de las QSO planas y sus familias dentro de los modelos del CR3BP y el H3BP. Esto incluye una clasificación geométrica basada en propiedades de simetría y características topológicas, y un análisis de su relación con la multiplicidad de cada familia. Además, se estudian las diferencias entre las familias en ambos modelos y cómo el H3BP puede emplearse para para mejorar el conocimiento y facilitar el cálculo de órbitas QSO en el modelo CR3BP, de mayor complejidad. Una de las mayores contribuciones de esta tesis, es la diferencia significativa hallada en los mecanismos de bifurcación de las familias de órbitas asimétricas entre ambos problemas.

En el marco del ER3BP, se lleva a cabo una búsqueda numérica global de QSO resonantes en los sistemas planetarios considerados. Durante este proceso, se realiza una clasificación de estas órbitas que amplía la desarrollada para el caso circular, incorporando nuevas características

geométricas y organizando las soluciones en tripletes de resonancia. Además, se examina la influencia de parámetros clave del sistema, como la razón de las masas y la excentricidad, revelando fenómenos como las bifurcaciones tipo "fold", que condicionan la transición de ciertas órbitas al ER3BP. Finalmente, en el CR3BP, se muestra que la razón de masas de los primarios limita la existencia de QSO asimétricas, ya que afecta a la ubicación del principio de las familias asimétricas y, por tanto, al intervalo de periodos que abarcan.

Table of Contents

List of Figures

List of Tables

Abbreviations and acronyms

2D Two-dimensional

3D Three-dimensional

4D Four-dimensional

6D Six-dimensional

A Asymmetric

Bif Bifurcation

Br Branch

Cart Cartesian

CR3BP Circular Restricted Three-Body Problem

CvM Cramer-von Mises

Curv Curvilinear

C-W Clohessy-Wiltshire

DA Down-Asymmetric

DNA Down-Narrow-Asymmetric

DPO Distant prograde orbit

DRO Distant Retrograde Orbit

DS Doubly.symmetric

DWA Down-Wide-Asymmetric

EDS Exterior-Doubly-Symmetric

ER3BP Elliptic Restricted Three-Body Problem

ESA European Space Agency

Fam Family

GEO Geosynchronous Equatorial Orbit

GNC Guidance, Navigation, and Control

H3BP Hill Three-Body Problem

IDS Interior-Doubly-Symmetric

JAXA Japan Aerospace Exploration Agency

JC Jacobi Constant

JE Jupiter–Europa

JUICE Jupiter Icy Moons Explorer

LEO Low Earth Orbit

LM Linear Model

LNSS Left-Narrow-Single-Symmetric

LPO Low prograde orbit

LSS Left-Single-Symmetric

LVLH Local-Vertical Local-Horizontal

LWSS Left-Wide-Single-Symmetric

M Mirrored

Mix Mixed

MMX Martian Moons eXploration

MP Mars–Phobos

NA Narrow Asymmetric

NASA National Aeronautics and Space Administration

NSS Narrow Single Symmetric

Orig Original

P2 Period-doubling

P3 Period-tripling

P4 Period-quadrupling

P5 Period-quintupling

P6 Period-sixtupling

P7 Period-septupling

QSO Quasi-Satellite Orbit

RNSS Right-Narrow-Single-Symmetric

RSS Right-Single-Symmetric

RWSS Right-Wide-Single-Symmetric

SM Sun–Mars

SS Single-symmetric

ST Saturn–Titan

STM State Transition Matrix

SVD Singular value decomposition

TB Tangent bifurcation

T–H Tschauner-Hampel

TLE Two-Line Element

UA Up-Asymmetric

UNA Up-Narrow-Asymmetric

UPM Universidad Politécnica de Madrid

UWA Up-Wide-Asymmetric

WA Wide-Asymmetric

WSS Wide-Single-Symmetric

Y–A Yamanaka-Ankersen

Chapter 1

Introduction

1.1 Motivation

In recent years, deep space missions beyond the Moon have attracted increasing interest from both the scientific and technological aspects. These missions aim to address fundamental questions regarding the search for habitable environments and the formation and evolution of the Solar System. A major focus of such missions is the study of planetary moons. According to NASA's sources, to date, Jupiter hosts 95 moons, Saturn has 274 natural satellites, 28 moons are already known for Uranus and even Mars possesses two enigmatic satellites, whose origins remain uncertain. These celestial bodies represent a vast and mostly unexplored territory that offers unique opportunities for investigation.

Among the most significant recent and upcoming deep space missions is the Jupiter Icy Moons Explorer (JUICE), launched by the European Space Agency (ESA) in 2023 [1]. This mission is designed to conduct a detailed exploration of Jupiter's three large icy moons: Europa, Ganymede, and Callisto. One of the main objectives of JUICE is to study the characteristics of the the moon's hydrosphere, with special focus on Ganymede, and to assess their potential habitability [2]. Complementary to this effort, NASA's Europa Clipper mission, launched last year, will perform multiple flybys of Jupiter's moon Europa [3]. The main objective of this mission is to characterize Europa's ice shell and confirm the existence of a subsurface ocean [4]. Beyond the Jupiter system, Saturn's largest moon, Titan, has emerged as a high-priority target due to its dense atmosphere and complex organic chemistry [5]. NASA's upcoming Dragonfly mission, part of the New Frontiers program and set to be launched in the upcoming years, will deploy a rotorcraft lander to explore Titan. This mission will provide unprecedented data on the prebiotic chemistry, habitability, and biosignatures of Titan [6].

Similarly, the Martian Moons eXploration (MMX) mission, led by the Japan Aerospace eXploration Agency (JAXA) and scheduled to be launched next year, is designed to study the origin and composition of Mars' two small moons: Phobos and Deimos [7]. This mission will collect surface samples from Phobos and return them to Earth, allowing scientists to determine whether these moons are captured asteroids or remnants of a giant impact event [8]. Understanding the nature of these satellites has profound implications for planetary formation

theories and Mars's evolutionary history [9]. Notably, this mission will employ quasi-satellite orbits (QSOs) as a stationary orbit around Phobos for its observation [10]. Among the vast possibilities of periodic orbits found in this type of scenario, QSOs are the main focus of this work.

In addition, this investigation examines QSOs not only for the Planet–Moon system of Mars–Phobos, but also for Jupiter–Europa and Saturn–Titan systems, due to their mentioned relevance in deep space missions. Moreover, the Sun–Mars system, with its similar relative mass characteristics, is also essential when considering such missions, so it will also be included in this work. In addition, rather than the usual Cartesian coordinates, in this work curvilinear coordinates are used, in order to utilize their advantages on linear dynamics.

1.2 State of the Art

1.2.1 Quasi-Satellite Orbits in the Three-Body Problem

Quasi-satellite orbits (QSOs), also known as distant retrograde orbits (DROs), first investigated by John Jackson as far back as 1913 [11], are an important class of periodic or quasi-periodic solutions of the three-body problem of great relevance for space missions and celestial mechanics. They arise from a 1:1 resonance of the third body with the second primary (co-orbital motion) with a librating guiding center and with the orbit of the third body well outside the Hill sphere ([12], [13]). The in-situ exploration of Mars' satellites Phobos and Deimos, for instance, would hardly be possible without resorting to QSOs [14]–[17]. Moreover, the benefits of these types of orbits for the exploration of Jupiter's moon Europa [18], [19] and the binary asteroid Didymos [20], as well as for the establishment of parking orbits in the Earth-Moon system [21], [22], have motivated their further investigation.

Among the different families of QSOs, planar single-period QSOs are known to be particularly stable, which makes them suitable parking orbits for an intermediate mission phase as well as safe and robust orbits for prolonged scientific exploration. Ideally, QSOs with periodic or nearly periodic behavior are preferred in order to simplify operations and provide long-term stability against environmental perturbations [8], [23], [24].

In the framework of the circular restricted three body problem, (CR3BP) a broad classification of planar periodic orbits not limited to QSOs was conducted by Michel Hénon in a sequel of three articles, an early work [25] and two much more recent ones [26], [27]. Employing the classical Hill's approximation, the first article of Hénon identified different families of planar prograde and retrograde periodic orbits. The five Hénon families include libration-point based orbits (termed a and c families), as well as periodic solutions originating from retrograde orbits around the second primary (the f family) and from prograde orbits (the g and g' family). Hénon's f family is the same as one already studied by Jackson and corresponds to an orbit that does not intersect itself (i.e. a *Jordan curve* in mathematical terminology) and will be referred to as a steady QSO in the present investigation.

On the other hand, in the work [26], Hénon studied what he called N-periodic orbits, in which there are more than two intersections with the syzygy-axix. Among these orbits, fully

retrograde symmetric orbits with several revolutions around the second primary were found in this work. This type of orbits have been referred to as swing QSOs or multi-revolution periodic QSOs by some authors ([15], [16], [28], [29]). These are orbits whose librating guiding center motion results in a trajectory that intersects itself in several points along its periodic evolution. Some, but not all, swing QSOs belong to a set of periodic orbits identified by Hénon as the $g3$ family [26]. These orbits, which are all symmetric with respect to the syzygy-axis, can be more easily obtained through a period-multiplying bifurcation from steady QSOs (see for instance [30], [15]). Although Hénon did also find some periodic asymmetric orbits in the CR3BP ([27]), they are strongly unstable prograde orbits, very different from QSOs, passing very close to the second primary and with limited applicability.

Russell [18] conducted an extensive search of symmetric periodic orbits for the Jupiter–Europa CR3BP obtaining several types of planar steady and swing QSOs without investigating asymmetric solutions. The work of Pushparaj et al. [15] addressed symmetric and asymmetric QSOs in the CR3BP for orbit transfer purposes in the exploration of Phobos. Chen et al. [31] also studied the stability of planar and spatial QSOs in the framework of the CR3BP thereby identifying areas of robust and safe operations for spacecraft missions around Phobos.

Moving onto the elliptic problem, Antoniadou et al. [32] addressed bifurcation aspects of symmetric and asymmetric resonant periodic orbits in the ER3BP. Lidov and Vashkov'yak ([33], [34]) addressed and computed several symmetric QSO orbits of both the steady and the swing type in the ER3BP with special emphasis on the Mars–Phobos system and applied perturbation theory to obtain approximate analytical solutions of the problem. Their work extended the original derivations by Kogan [35], who first demonstrated the stability of QSO orbits when Phobos is in a circular orbit around Mars by means of linearization and averaging techniques. A more accurate and sophisticated analytical solution for QSOs in the Hill-approximated planar CR3BP has been recently obtained by Lara ([36]) using perturbation theory. Similarly, Baresi et al. [37] employed the method of averaging to develop approximate analytical solutions of the 3-dimensional Hill-approximated ER3BP. Baresi et al. [14] also numerically continued QSO orbits into their two-dimensional quasi-periodic substitutes that replace the original periodic solutions once the eccentricity of a moon like Phobos is taken into account. As for the investigation of QSOs in the framework of the general (not restricted) elliptic three-body problem, Broucke and Boggs [38] and Broucke [39] computed a number of planar periodic orbits including a few QSOs and clarified important mathematical aspects of the problem including symmetry properties.

1.2.2 Curvilinear Coordinates

Traditional methods for modeling co-orbital motion predominantly rely on Cartesian coordinates. However, because orbital trajectories naturally follow curved arcs, there has been growing interest in using curvilinear coordinates, which could better capture the inherent curvature of these trajectories [40]–[43]. Recent studies have demonstrated some advantages of curvilinear formulations, particularly in improving the accuracy of linearized motion models for both two-body relative dynamics and the three-body problem. Most of these studies focus on circular reference orbit scenarios, with still more work to be done for elliptic cases. Below are the most relevant works about curvilinear coordinates in these areas.

In the two-body relative motion, one of the most use sets of equations is the Clohessy-Wiltshire (C–W) equations [44]. These equations, which represent the linearized two-body relative motion with the reference body or chief in a circular orbit, are written in the classical Cartesian coordinates. This model is less accurate than higher-order or more complex methods, but is still used today owing to its simplicity. The analogue equations written in curvilinear coordinates, both spherical and cylindrical, can be found in several works [42], [45], [46]. DeBruijn et al. [46] showed an improvement in performance with the curvilinear coordinates for along-track formations; Alfriend et al. [45] established a reduction on the nonlinearities with the use of the curvilinear coordinates; and Geller and Lovell [42] achieved observability with angles-only measurements in cylindrical coordinates, contrary to the Cartesian results. Beyond linearized motion, but still for a circular reference, Bombardelli et al. [47] and Hernando-Ayuso and Bombardelli [40] offered higher-order approximations with improved accuracy compared to other Cartesian approximations. Another work that assesses the use of curvilinear coordinates for relative motion is the one of Vallado et al. [43], where the transformation between the Cartesian and curvilinear frame for relative motion is studied. This work shows how this transformation can be used for a better orientation of the covariance ellipsoid.

For elliptic reference orbits, the Tschauner–Hempel (T–H) equations serve as the elliptical counterpart to the C–W equations in Cartesian coordinates. A significant advancement in this area is the work of Yamanaka and Ankersen (hereafter Y–A) [48], who developed a fully analytical state transition matrix (STM) for linearized relative motion with respect to a Keplerian elliptic reference orbit. This STM is applicable for arbitrary values of the nominal orbit eccentricity, marking it as a milestone contribution in the field of astrodynamics. As a result, the Y–A STM has been widely adopted in the literature. A critical, and often overlooked, aspect of Y–A's derivation is the use of a "pulsating" reference length unit. This approach is conceptually similar to that found in the Nechvíle curvilinear coordinates used in the restricted three-body problem. In this direction, recently, Han et al. [49] developed a spherical formulation of the T–H equations and an analogue of the Y–A STM, showing better accuracy than the original Y–A STM for large along-track separations. Willis et al. [50] extended this work to a second-order solution that compared with its Cartesian counterpart showed, again, a better behavior when the along-track distance is considerable.

In the context of the three-body problem, curvilinear formulations have also proven valuable. Notably, Bombardelli and Bernal Mencía [41] presented a cylindrical version of the CR3BP that is used for the extension of Yoder's formula on the boundary of the guiding center motion. For the ER3BP, Gil Calvo [51] extended Bombardelli and Bernal's work by performing an expansion on eccentricity to obtain the equations of motion in curvilinear coordinates.

1.3 Objectives

Motivated by the current needs of deep space missions, the main goal of this thesis is to advance the understanding and modeling of quasi-satellite orbits (QSOs) within the framework of the three-body problem. Building upon previous contributions, this investigation places particular emphasis on asymmetric QSOs, which have received limited attention in the literature, and

resonant QSOs that give rise to periodic orbits in the ER3BP, potentially suitable for parking, transfer, and science orbits in future mission design. Additionally, this thesis aims to leverage the advantages of curvilinear coordinates, previously observed in the study of the co-orbital motion, to drive this investigation. To this end, a new STM in cylindrical coordinates is developed for relative motion. Its promising results in uncertainty propagation highlight its potential for futre applications in autonomous guidance, navigation, and control (GNC) systems.

To achieve this goal, the thesis pursues the following specific objectives:

- **Evaluate curvilinear coordinates for modeling relative motion.** Assess the use of curvilinear coordinates for the linearized two-body relative motion, by evaluating their performance in uncertainty propagation applications and comparing them with Cartesian coordinates. Since this work primarily focuses on planar motion, relative motion equations are formulated in pulsating cylindrical coordinates to exploit their in-plane and out-of-plane decomposition, instead of using the spherical formulation already found in the literature. These equations are then linearized to obtain a curvilinear analogue of the T–H equations, followed by the derivation of a cylindrical analogue of the Y–A STM.
- **Develop the CR3BP and ER3BP equations of motion in curvilinear coordinates.** Formulate the exact equations of motion for both the CR3BP and the ER3BP, as well as all other related equations required for the continuation of periodic orbits in these models, using cylindrical curvilinear coordinates. All numerical tools for orbit continuation were developed through an in-house implementation, without the use of third-party software, to allow full flexibility and integration with the curvilinear formulation.
- **Construct and analyze periodic QSO families.** Develop and characterize families of periodic QSOs, including both steady and swing types, not only in the CR3BP but also in the H3BP, with the aim of gaining a deeper understanding of complex phenomena such as the emergence of asymmetric QSO families. Three-dimensional QSOs in the H3BP are also studied. This study includes an analysis of orbital stability and a classification of the various family branches from a geometric point of view, by focusing on symmetry properties and other salient geometric features, and examining their relationships with the corresponding multiplicity.
- **Identify and classify periodic resonant QSOs in the ER3BP.** Conduct a global search and characterization of periodic resonant QSOs in the planar ER3BP, up to a reasonable resonance ratio, for both symmetric and asymmetric QSOs and across a set of representative systems covering a wide range of mass ratios, namely Mars–Phobos, Sun–Mars, Jupiter–Europa and Saturn–Titan. A unified and straightforward classification is provided, from both the resonance ratio perspective (by introducing a new nomenclature based on resonance triplets) and a geometric point of view, extending the classification developed for the branches in the circular problem. Furthermore, the influence of system parameters such as the mass ratio and orbital eccentricity is examined, identifying relevant bifurcation phenomena, such as fold bifurcations in the

ER3BP.

1.4 Thesis Outline

This thesis is structured as follows:

- **Chapter 2.** In this chapter, the formulation of curvilinear coordinates, particularly cylindrical coordinates, is introduced. As a previous step to the rest of the work, where the restricted three-body problem is addressed, in this chapter the equations of the two-body relative motion are derived in curvilinear coordinates. A linearization of these equations is performed to obtain a cylindrical curvilinear analogue of the Y–A STM. Afterwards, a detailed comparison between Cartesian and curvilinear approaches is presented in the task of orbit uncertainty propagation, showing an improvement in uncertainty realism compared to the Cartesian case in the great majority of relevant space situational awareness applications.
- **Chapter 3.** This chapter provides an extensive overview of the dynamical models used in the study of periodic orbits throughout the rest of the thesis, including the Elliptic Restricted Three-Body Problem (ER3BP), the Circular Restricted Three-Body Problem (CR3BP) and the Hill's approximation of the Three-Body Problem (H3BP). This chapter also introduces the notation and terminology used along the remainder of this work.
- **Chapter 4.** This chapter includes the numerical methodologies employed in the computation and study of periodic orbits in the introduced dynamical systems. First, the continuation methods used in this investigation are explained. After that, the concept of linear stability of a periodic orbit is introduced as well as the role that it has on the bifurcations between families of orbits.
- **Chapter 5.** In this chapter, the QSOs are studied in the H3BP. This includes not only the steady QSO or DRO family, but also the families bifurcated from it both in-plane and out-of-plane.
- **Chapter 6.** This chapter studies the differences found between the families of planar QSOs in the CR3BP and the H3BP. This includes the existence of broken bifurcations and a different origin of the families of asymmetric QSOs.
- **Chapter 7.** In this chapter, resonant QSOs are studied for the in-plane motion. This orbits are derived not only in the H3BP and the CR3BP as previously done, but also in the ER3BP. Different phenomena are analyzed in this chapter, like the influence of the mass ratio of the system on the existence of asymmetric resonant QSOs, or the existence of fold bifurcations in the ER3BP.
- **Chapter 8.** In this chapter, a discussion of the results obtained throughout the previous chapter is done.
- **Chapter 9.** Finally, this chapter summarizes the results and conclusions of this dissertation. In addition, some potential future works are suggested.

1.5 List of Publications and Conferences

As a result of the research activities carried out throughout the development of this dissertation, the following peer-reviewed journal papers and conferences have been done:

Journal papers

- A. Martínez-Cacho, D. Gil Calvo, C. Bombardelli, and N. Baresi, "Planar retrograde periodic orbits in the elliptic restricted three-body problem", *Acta Astronautica*, vol. 229, pp. 430–465, 2025. doi: https://doi.org/10.1016/j.actaastro.2025.01.006.
- J. Hernando-Ayuso, C. Bombardelli, G. Baù, and A. Martínez-Cacho, "Near-linear orbit uncertainty propagation using the generalized equinoctial orbital elements", *Journal of Guidance, Control, and Dynamics*, vol. 46, no. 4, pp. 654–665, 2023. doi: https://doi.org/10.2514/1.G006864.

Conference proceedings

- C. Bombardelli, A. Martínez-Cacho, and R. Russell, "Quadratic models for keplerian relative motion", in *AAS/AIAA Astrodynamics Specialist Conference*, Aug. 2024.

Workshop Presentations (without proceedings)

- A. Martínez-Cacho and C. Bombardelli, "A curvilinear generalization of the Yamanaka-Ankersen state transition matrix", in *5th International Workshop on Key Topics in Orbit Propagation applied to Space Situational Awareness (KePASSA)*, Logroño, La Rioja, Spain, Jun. 2022.
- C. Bombardelli and A. Martínez-Cacho, "Quadratic model for analytical uncertainty propagation", in *6th International Workshop on Key Topics in Orbit Propagation applied to Space Situational Awareness (KePASSA)*, Arras, France, Jun. 2024.

Chapter 2

Curvilinear Coordinates: Relative Motion

In this chapter, curvilinear coordinates are studied and compared to Cartesian coordinates through the equations of relative motion in the two-body problem. This serves as a preliminary analysis for the remainder of the dissertation, where curvilinear coordinates are used in the formulation of the restricted three-body problem. Among the different types of curvilinear coordinates, and given that most of this dissertation focuses on planar motion, cylindrical coordinates are adopted. In addition, since the reference orbit considered in both the relative motion and the restricted-three body problem is elliptical, a "pulsating" reference length unit is required. Accordingly, "pulsating cylindrical" coordinates are employed in this work.

The study in this chapter follows the sequence outlined below. First, the conditions of the system used are introduced and the pulsating curvilinear coordinates are defined. Then, the nonlinear equations of relative motion are derived in these coordinates and subsequently linearized to obtain a curvilinear version of the well-known Tschauner-Hemple (T–H) equations. A solution to the linearized model is obtained by following the same procedure used to derive the well-known Yamanaka-Ankersen (Y–A) STM that solves the Tschauner-Hemple equations. This results in a cylindrical analogue of the Y–A STM. Finally, the performance of the Y–A Cartesian STM is compared with that of the derived curvilinear analogue for uncertainty propagation, using a Cramer-von Mises (CvM) test of Uncertainty Realism.

2.1 System Definition

In the relative motion of the two-body problem, the reference orbit is the one performed by the target around the central body, in this case the Earth, and following the two-body dynamical model. Therefore, it is, in general, a Keplerian elliptic orbit that is defined by the orbital elements $(a, e, i, \Omega, \omega, M)$: where a and e are the semi-major and the eccentricity of the orbit, respectively; i corresponds to the inclination of the orbit with respect to the equator; Ω is the longitude of the ascending node; ω is the argument of periapsis; and finally M corresponds to the mean anomaly at epoch. Among these elements, the first two determine the shape of

the orbit, the next three angular quantities orientate this orbit within the space, and finally the last element corresponds to the position within the orbit. For a two-body unperturbed problem, like the one considered in this chapter, the first 5 elements are constant in time and only the last one varies as the target moves within the orbit. In this work, sometimes instead of the semi-major axis, the periapsis distance r_p is used.

In this work, nondimensional quantities are used. To achieve this, the parameters of the reference orbit are employed, particularly the semi-major axis, a, and the mean motion, $n = \sqrt{\dfrac{Gm_E}{a^3}}$, to establish the unit of length and time

$$LU = a, \qquad TU = \frac{1}{n} = \sqrt{\frac{a^3}{Gm_E}}, \tag{2.1}$$

where m_E is the mass of Earth, which is the central body considered in this chapter. This leads to the nondimensional time, denoted by τ. Regarding the remaining variables, capital letters are generally used to denote dimensional magnitudes, and lowercase letters for nondimensional ones.

However, following the same procedure used for the T–H equations or [52] and [53]) for the three-body problem, pulsating coordinates are required to better represent the equations of motion. Accordingly, a new pulsating unit of length is defined by the instant position of the target

$$LU^P = R_T = \frac{p}{\gamma} = \frac{a(1-e^2)}{1+e\cos\nu}, \tag{2.2}$$

where p is the semi-latus rectum of the reference orbit and $\gamma = 1 + e\cos\nu$. This pulsating unit of length is used for any pulsating coordinate, while the standard unit is used for non-pulsating ones. The relation between these two units of length is

$$\frac{LU^P}{LU} = \frac{p}{a\gamma} = \frac{(1-e^2)}{1+e\cos\nu}. \tag{2.3}$$

This is more clearly expressed by introducing the nondimensional semi-latus rectum, denoted by $\tilde{p}$, so that

$$\frac{LU^P}{LU} = \frac{\tilde{p}}{\gamma}. \tag{2.4}$$

With the pulsating rescaling, and using the dimensionless time τ as the independent variable, the target describes a non-uniform circular motion with respect to a central body. Furthermore, a uniform circular motion can be obtained by adopting the true anomaly ν as the independent variable (fictitious time), so it will be the one used in this work for pulsating coordinates. Therefore, to differentiate between the use of the nondimensional time τ and the true anomaly ν in the derivatives, the ones with respect to τ are indicated by dots and the ones with respect to ν by primes.

Following all of this, both the pulsating Cartesian coordinates (used in the T–H equations) and the curvilinear ones can be defined. The pulsating Cartesian state (x, y, z, x', y', z') is defined with respect to the local-vertical local-horizontal (LVLH) frame $\mathcal{L}$ with orthonormal

basis $\{\mathbf{i}, \mathbf{j}, \mathbf{k}\}$, represented in Figure 2.1. The LVLH frame is centered at the target and with $\mathbf{i}$ pointing opposite to the central body. Regarding the cylindrical state $(\rho, \theta, z, \rho', \theta', z')$, it is defined using the $\mathcal{H}$ frame with orthonormal basis $\{\mathbf{u}_\rho, \mathbf{u}_\theta, \mathbf{k}\}$, also observed in Figure 2.1. This frame is centered at the central body and with $\mathbf{u}_\rho$ pointing towards the chaser C. Note that, as shown in the literature [54], the $\mathcal{H}$ frame is particularly useful when dealing with curvilinear coordinates as opposed to the classical Cartesian frame. Both frames share the vector $\mathbf{k}$, which points towards the angular momentum of the motion of the target around the central body, completing a right-handed orthonormal triad for each.

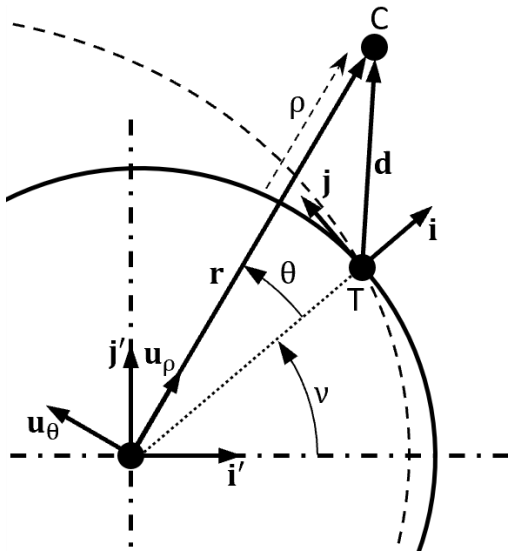

Figure 2.1: Relative motion geometry using the instant position of the target as the unit of distance.

Moreover, in the figure also the basis $\{\mathbf{i}', \mathbf{j}', \mathbf{k}'\}$ is shown and corresponds to the perifocal coordinate system and it will be used as the reference inertial frame $\mathcal{I}$. In addition, the circular orbit obtained thanks to the pulsating unit of length is shown in the figure. In addition, the dashed line shows the elliptical motion of the target as how the trajectory would be seen with the instantaneous dimensionalization.

After this, it is important to derive the relation between the derivatives with respect to τ and ν. For that, first the expression of the time derivatives of the true anomaly are needed

$$\dot{\nu} = \frac{\gamma^2}{\tilde{p}^{3/2}}, \qquad \ddot{\nu} = -\frac{2\gamma^3 e \sin\nu}{\tilde{p}^3}. \tag{2.5}$$

With that, the time derivative of the first two curvilinear coordinates are related to their derivatives with respect to the true anomaly as follows

$$\begin{pmatrix} \dot{\rho} \\ \dot{\theta} \end{pmatrix} = \dot{\nu} \begin{pmatrix} \rho' \\ \theta' \end{pmatrix} = \frac{\gamma^2}{\tilde{p}^{3/2}} \begin{pmatrix} \rho' \\ \theta' \end{pmatrix} \tag{2.6}$$

$$\begin{pmatrix} \ddot{\rho} \\ \ddot{\theta} \end{pmatrix} = \dot{\nu}^2 \begin{pmatrix} \rho'' \\ \theta'' \end{pmatrix} + \ddot{\nu} \begin{pmatrix} \rho' \\ \theta' \end{pmatrix} = \frac{\gamma^4}{\tilde{p}^3} \begin{pmatrix} \rho'' \\ \theta'' \end{pmatrix} - \frac{2\gamma^3 e \sin\nu}{\tilde{p}^3} \begin{pmatrix} \rho' \\ \theta' \end{pmatrix}. \tag{2.7}$$

These equations will be used in the following section, where the equations of motion are derived in pulsating curvilinear coordinates.

Finally, the non-pulsating Cartesian state $(\tilde{x}, \tilde{y}, \tilde{z}, \dot{\tilde{x}}, \dot{\tilde{y}}, \dot{\tilde{z}})$, often used in the derivation of the equations of relative motion, is also used throughout the work, in particular for plotting the trajectories in the rotating frame. The transformation between Cartesian and pulsating cylindrical coordinates is shown in Appendix A.

2.2 Equations of Relative Motion in Curvilinear Coordinates

In order to obtain the equations of the relative motion, first let express the position of the chaser in curvilinear coordinates

$$\mathbf{r} = \frac{\tilde{p}}{\gamma} \left(r_\rho \, \mathbf{u}_\rho + z \, \mathbf{k} \right), \tag{2.8}$$

where

$$r_\rho = 1 + \rho.$$

The velocity and acceleration of the chaser with respect to the $\mathcal{H}$ frame are obtained by differentiation of Eq. (2.8) and taking into account Eqs. (2.6, 2.7)

$$\left.\frac{d\mathbf{r}}{d\tau}\right|_{\mathcal{H}} = \left(\frac{\gamma}{\tilde{p}^{1/2}} \rho' + r_\rho \frac{e \sin\nu}{\tilde{p}^{1/2}} \right) \mathbf{u}_\rho + \left(\frac{\gamma}{\tilde{p}^{1/2}} z' + z \frac{e \sin\nu}{\tilde{p}^{1/2}} \right) \mathbf{k} \tag{2.9}$$

$$\left.\frac{d^2\mathbf{r}}{d\tau^2}\right|_{\mathcal{H}} = \left(\frac{\gamma^3}{\tilde{p}^2} \rho'' + \frac{\gamma^2}{\tilde{p}^2} r_\rho e \cos\nu \right) \mathbf{u}_\rho + \left(\frac{\gamma^3}{\tilde{p}^2} z'' + \frac{\gamma^2}{\tilde{p}^2} z e \cos\nu \right) \mathbf{k}. \tag{2.10}$$

The exact equations of motion of the chaser can now be obtained by writing the acceleration relative to $\mathcal{H}$ as

$$\left.\frac{d^2\mathbf{r}}{d\tau^2}\right|_{\mathcal{H}} = \left.\frac{d^2\mathbf{r}}{d\tau^2}\right|_{\mathcal{I}} - 2\boldsymbol{\omega}_{\mathcal{H}} \times \left.\frac{d\mathbf{r}}{d\tau}\right|_{\mathcal{H}} - \boldsymbol{\omega}_{\mathcal{H}} \times (\boldsymbol{\omega}_{\mathcal{H}} \times \mathbf{r}) - \boldsymbol{\alpha}_{\mathcal{H}} \times \mathbf{r},$$

where $\boldsymbol{\omega}_{\mathcal{H}}$ and $\boldsymbol{\alpha}_{\mathcal{H}}$ are the vector angular rate and the angular acceleration of $\mathcal{H}$ with respect to $\mathcal{I}$, respectively. All the variables of this equation can be easily obtained. First, the acceleration in the inertial frame is the one corresponding to the two-body problem

$$\left.\frac{d^2\mathbf{r}}{d\tau^2}\right|_{\mathcal{I}} = -\frac{\mathbf{r}}{r^3}, \tag{2.11}$$

where

$$r = \frac{\tilde{p}}{\gamma} \sqrt{r_\rho^2 + z^2}. \tag{2.12}$$

Second, the angular rate and angular acceleration of $\mathcal{H}$ with respect to an inertial frame can be written, by use of Eqs. (2.6, 2.7) as

$$\boldsymbol{\omega}_{\mathcal{H}} = \dot{\nu} + \dot{\theta} = \frac{\gamma^2}{\tilde{p}^{3/2}} \left(1 + \theta'\right) \mathbf{k} \tag{2.13}$$

$$\boldsymbol{\alpha}_{\mathcal{H}} = \ddot{\nu} + \ddot{\theta} = \left[\frac{\gamma^4}{\tilde{p}^3}\theta'' - 2\frac{\gamma^3}{\tilde{p}^3}e\sin\nu\,(1+\theta')\right]\,\mathbf{k}. \tag{2.14}$$

After developing the above equations taking into account the previous kinematic relations in Eqs.(2.8-2.14) and projecting them onto $\{\mathbf{u}_\rho,\,\mathbf{u}_\theta,\,\mathbf{k}\}$, the exact differential equations for the three pulsating curvilinear variables with the true anomaly as independent variable are finally obtained

$$\begin{cases} \rho'' = r_\rho\,(2+\theta')\,\theta' + \dfrac{r_\rho}{\gamma}\left(1 - \dfrac{1}{\tilde{r}^3}\right) \\ \theta'' = \dfrac{-2\rho'\,(1+\theta')}{r_\rho} \\ z'' = \dfrac{z}{\gamma}\left(-e\cos\nu - \dfrac{1}{\tilde{r}^3}\right) \end{cases}, \tag{2.15}$$

where

$$\tilde{r} = \sqrt{r_\rho^2 + z^2}. \tag{2.16}$$

By linearizing all the terms of Eq. (2.15), and following the same structure as in [47], they can be expressed as

$$\begin{cases} \rho'' - 2\theta' - \dfrac{3}{\gamma}\rho = a_{i\rho} + \dfrac{1}{\gamma}a_{g\rho} \\ \theta'' + 2\rho' = a_{i\theta} \\ z'' + z = \dfrac{1}{\gamma}a_{gz} \end{cases}, \tag{2.17}$$

where the right side contains the non-linear terms

$$\begin{aligned} a_{i\rho} &= r_\rho\theta'^2 + 2\rho\theta', \\ a_{g\rho} &= -2\rho + 1 - \frac{r_\rho}{\left[r_\rho^2 + z^2\right]^{3/2}}, \\ a_{i\theta} &= \frac{2\rho'(\rho - \theta')}{r_\rho}, \\ a_{gz} &= z - \frac{z}{\left[r_\rho^2 + z^2\right]^{3/2}}. \end{aligned} \tag{2.18}$$

2.3 Curvilinear Analogue of the Yamanaka-Ankersen State Transition Matrix

The linearized version of the relative motion equations in curvilinear coordinates, Eq. (2.17),

$$\begin{cases} \rho'' - 2\theta' - \dfrac{3}{\gamma}\rho = 0 \\ \theta'' + 2\rho' = 0 \\ z'' + z = 0. \end{cases} \tag{2.19}$$

has the exact same structure as the T–H equations

$$\begin{cases} x'' - 2y' - \dfrac{3}{\gamma}x = 0 \\ y'' + 2x' = 0 \\ z'' + z = 0. \end{cases} . \tag{2.20}$$

This similarity allows to obtain a STM similar to the one proposed by Yamanaka and Ankersen to solve the T–H equations, by following the same mathematical development followed in [48]. It is important to notice that in this paper the convention used for the LVLH frame is different than the one used in this work, with both the radial and out-of-plane axis pointing in the opposite direction and a different ordering of the axes. So, this has been adapted for this work. Hence, first, let subdivide the problem in the out-of-plane and in-plane motions, following the same process as in [48].

2.3.1 Out-of-plane

The out-of-plane axis coincides for both curvilinear and Cartesian coordinates. Therefore, the STM coincides too, being[1]

$$\begin{bmatrix} z \\ z' \end{bmatrix} = \frac{1}{\gamma(\nu - \nu_0)} \begin{bmatrix} c & s \\ -s & c \end{bmatrix}_{\nu-\nu_0} \begin{bmatrix} z_0 \\ z_0' \end{bmatrix}, \tag{2.21}$$

where $c(\nu) = \gamma(\nu)\cos(\nu)$ and $s(\nu) = \gamma(\nu)\sin(\nu)$ and $\gamma(\nu - \nu_0) = 1 + e\cos(\nu - \nu_0)$.

2.3.2 In-plane

In this motion, cylindrical and Cartesian coordinates have different definitions. However, as seen, the equations have the same structure. Therefore, the curvilinear STM can be obtained following the same procedure depicted in [48] and obtaining the same result

$$\begin{bmatrix} \rho \\ \theta \\ \rho' \\ \theta' \end{bmatrix} = \begin{bmatrix} 0 & s & c & (2 - 3esJ) \\ -1 & c\,(1 + 1/\gamma) & -s\,(1 + 1/\gamma) & -3\gamma^2 J \\ 0 & s' & c' & -3e\,(s'J + s/\gamma^2) \\ 0 & -2s & -2c + e & -3\,(1 - 2esJ) \end{bmatrix}_{\nu} \begin{bmatrix} K_1 \\ K_2 \\ K_3 \\ K_4 \end{bmatrix}, \tag{2.22}$$

with

$$\begin{bmatrix} K_1 \\ K_2 \\ K_3 \\ K_4 \end{bmatrix} = \frac{1}{e^2 - 1} \begin{bmatrix} 3e(s/\gamma)(1 + 1/\gamma) & e^2 - 1 & 2 - ec & es(1 + 1/\gamma) \\ -3(s/\gamma)(1 + e^2/\gamma) & 0 & c - 2e & -s(1 + 1/\gamma) \\ -3(c/\gamma + e) & 0 & -s & -c(1 + 1/\gamma) - e \\ 3\gamma + e^2 - 1 & 0 & es & \gamma^2 \end{bmatrix}_{\nu_0} \begin{bmatrix} \rho_0 \\ \theta_0 \\ \rho_0' \\ \theta_0' \end{bmatrix}, \tag{2.23}$$

[1] Notice that in [48] the coordinate y, which corresponds there to the out-of-plane coordinate, is oriented following the direction of $-\mathbf{h}$ (being $\mathbf{h}$ the angular momentum vector of the target) while in here z is oriented towards $\mathbf{h}$.

where

$$J(\nu) = \int_{\nu_0}^{\nu} \frac{d\nu}{\gamma^2(\nu)} = \frac{(Gm_E)^2}{h^3}(t - t_0), \tag{2.24}$$

being h the angular momentum of the target.

2.4 Cartesian vs Curvilinear Coordinates for Linear Uncertainty Propagation

One important application of the relative motion STM is the uncertainty propagation. Hence, it is of high interest the evaluation of the performance in uncertainty propagation of the curvilinear STM by comparing it with the Y–A STM's performance. This is carried out by means of the Uncertainty Realism, which is evaluated using the Cramer-von Mises (CvM) test of the Mahalanobis distance distribution. The details of this test can be found in [55].

Considering an initial Gaussian probability density function (PDF) and its corresponding set of orbital states sampled, the CvM test evaluates if the Mahalanobis distance of the samples follows a chi-squared distribution for each epoch. When this is achieved, the PDF remains Gaussian, thus the uncertainty is realistic. The Mahalanobis distance is defined as:

$$\mathcal{M}_i(\mathbf{x}_i; \mathrm{E}[\mathbf{X}], \mathbf{P}) = (\mathbf{x}_i - \mathrm{E}[\mathbf{X}])^T \mathbf{P}^{-1} (\mathbf{x}_i - \mathrm{E}[\mathbf{X}]), \tag{2.25}$$

where, at each time instance, $\mathbf{x}_i$ is the ith sample state propagated with a full nonlinear orbital dynamics model, $\mathrm{E}[\mathbf{X}]$ is the mean of the set of sample states and $\mathbf{P}$ is the linearly[2] propagated covariance matrix. The covariance matrix propagation is done by

$$\mathbf{P}(t) = \mathbf{\Phi}(t, t_0)\mathbf{P}(t_0)\mathbf{\Phi}^T(t, t_0), \tag{2.26}$$

where $\mathbf{\Phi}(t, t_0)$ is the STM in the corresponding space.

2.4.1 Test Conditions

In this work, the CvM test is performed in Cartesian coordinates using the Y–A STM and in curvilinear coordinates with the STM obtained in Section 2.3. In both cases, the set of samples has a size of $N = 10000$ and the test is performed with a 99.9% confidence level. This pair of confidence level and N implies that the covariance is realistic while the value of the CvM test statistics remains lower than 1.16204 [56]. The set of samples is propagated using Matlab's ode45 and a Keplerian dynamic model.

There are two different orbits to be studied whose initial orbital elements are shown in Table 2.1 and whose initial covariance matrices written in the LVLH frame are shown in Table 2.2. When performing the test for the curvilinear STM, the covariance matrix is transformed by the full nonlinear elements conversion.

The first case of study is a GEO with a TLE-like covariance matrix. The values of the covariance matrix have been obtained after analyzing the position and velocity uncertainty

[2]Notice that the CvM test can be used with nonlinear covariance propagation methods. Nonetheless, as the focus lies on the study of a STM, only the linear propagation has been considered

Type	r_p (km)	e	i (°)	Ω (°)	ω (°)	M_0 (°)
GEO	42164.1	0	0	0	0	0
LEO	7000	Variable	25	120	0	180

Table 2.1: Initial orbital elements

Case	σ_x (m)	σ_y (m)	σ_z (m)	$\sigma_{\dot{x}}$ (m/s)	$\sigma_{\dot{y}}$ (m/s)	$\sigma_{\dot{z}}$ (m/s)
GEO	1000	3000	5000	0.3	0.1	0.4
LEO	100	300	500	0.03	0.01	0.04

Table 2.2: Initial Covariance in LVLH frame

for different satellites in GEO, whose data were obtained as two-line elements (TLEs) from the Space-track webpage [57]. As for the second case, it corresponds to a LEO that is studied for different eccentricities: from the circular case to $e = 0.8$ in intervals of eccentricities of 0.1. The initial conditions of this LEO are always placed at the perigee, which is kept with a constant radius when changing the eccentricity. This means that the semi-major axis will vary for each eccentricity as

$$a = \frac{r_p}{1 - e}. \tag{2.27}$$

For this case, the covariance matrix selected is the GEO TLE-like covariance reduced by a factor of 10.

2.4.2 Results

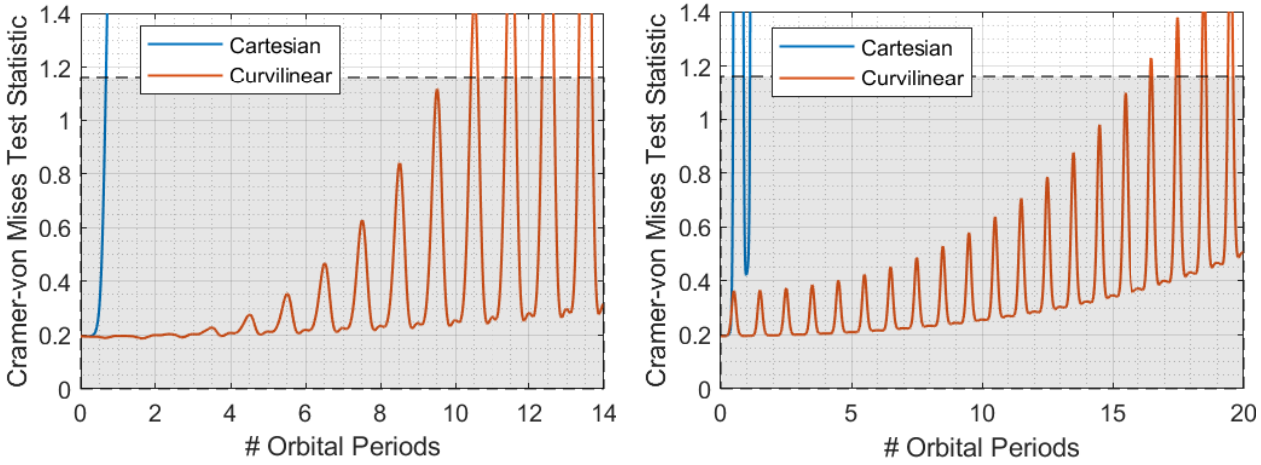

(a) GEO **(b)** LEO

Figure 2.2: CvM test statistics for circular orbits.

The Cramer-von Mises (CvM) test statistics for the circular cases, i.e. the GEO and the circular LEO, are shown in Figure 2.2. In both cases, the CvM test fails before 1 orbital period with the Cartesian Y–A STM, whereas with the curvilinear STM the realism is maintained for more than 10 orbits for GEO and more than 16 orbits for the circular LEO. Therefore, in

these cases curvilinear coordinates provide a huge improvement in realism with respect to Cartesian ones.

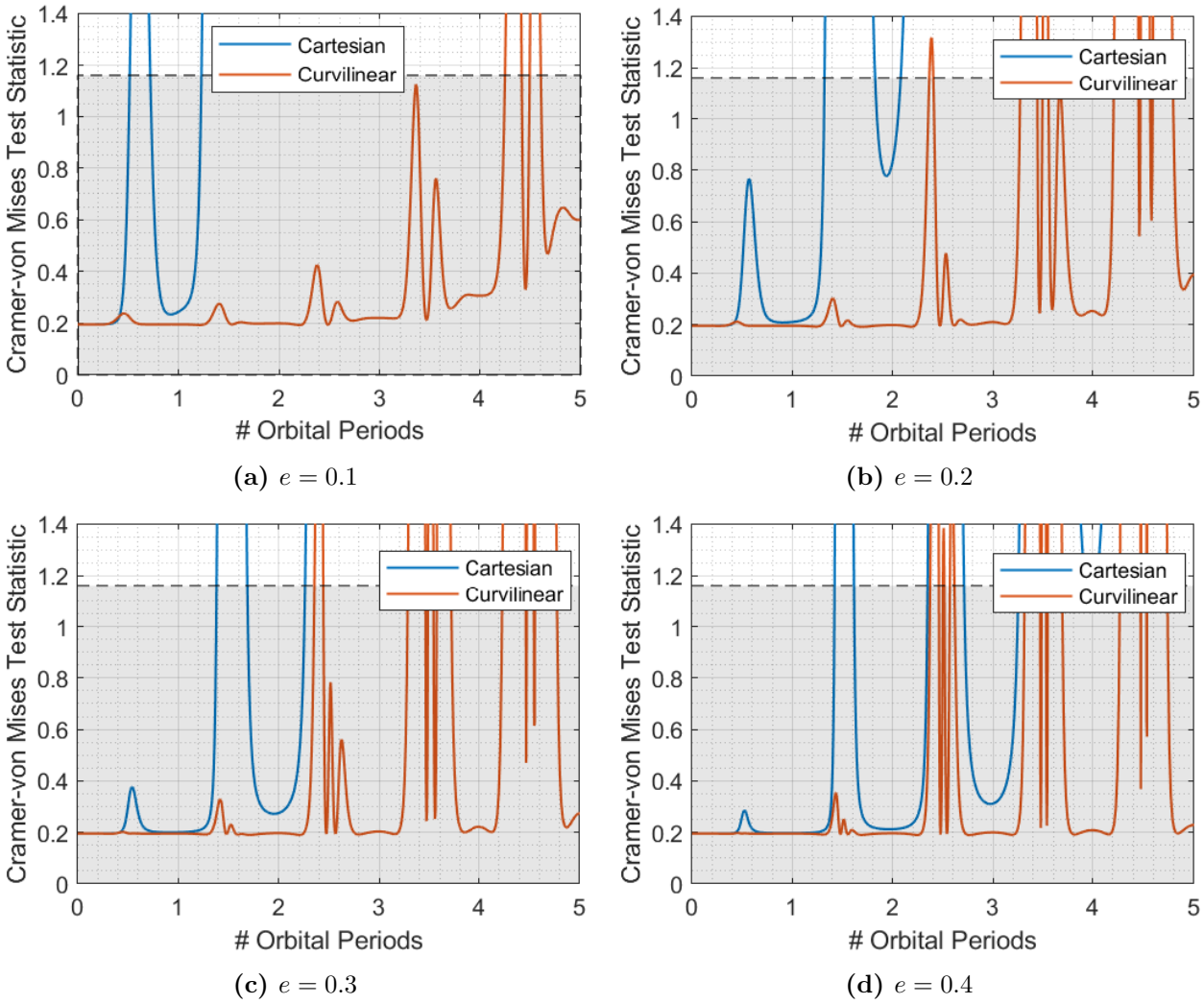

(a) $e = 0.1$ **(b)** $e = 0.2$

(c) $e = 0.3$ **(d)** $e = 0.4$

Figure 2.3: CvM test statistics for LEO for different eccentricities (Part 1).

The CvM test statistics for the 8 eccentric cases of the LEO orbit are shown in Figures 2.3 and 2.4. For $e = 0.1$ (Figure 2.3a), the realism is maintained for half an orbit for the Cartesian Y–A STM and around 4 orbits for the curvilinear one. This result entails a better performance with the curvilinear STM again. The second case is the one of $e = 0.2$ (Figure 2.3b). Compared to the previous case, the Cartesian STM performs better as it achieved to maintain the realism for around 1 more orbit, reaching the threshold for around 1 orbit and a half. The opposite takes place to the curvilinear STM, as this time it only keeps the realism for a bit more than 2 orbits. However, this is still better than the performance of the Cartesian STM. This is exactly the same situation encountered for the next four eccentricities: $e = 0.3$ (Figure 2.3c), $e = 0.4$ (Figure 2.3d), $e = 0.5$ (Figure 2.4a) and $e = 0.6$ (Figure 2.4b). For these cases the evolution of the test statistics have some differences. Nevertheless, in all the cases it crosses the threshold for around one period and a half for the Cartesian STM

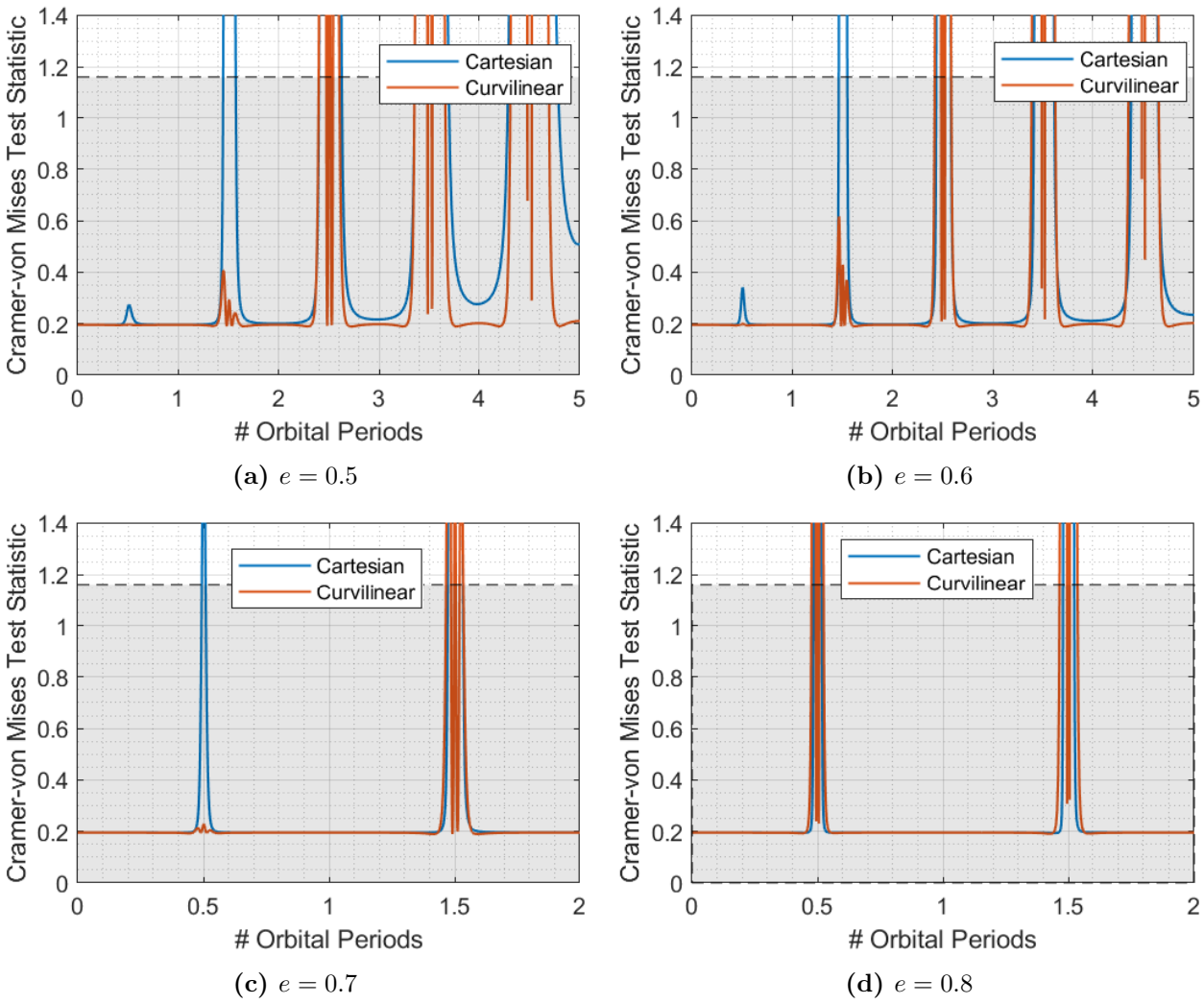

(a) $e = 0.5$ **(b)** $e = 0.6$

(c) $e = 0.7$ **(d)** $e = 0.8$

Figure 2.4: CvM test statistics for LEO for different eccentricities (Part 2).

and around two and a half for the curvilinear one. For the next case, $e = 0.7$ (Figure 2.4c), the performance of both types of coordinates worsens in one orbit. This means that now the realism is lost after only half an orbit for the original Y–A STM and one and a half for the new curvilinear one. However, curvilinear coordinates still showed a better performance. Finally, the case of $e = 0.8$ (Figure 2.4d) is the only one in which the curvilinear coordinates do not beat the Cartesian ones, since in this case both of them lose the realism after only half an orbit.

Another conclusion that can be drawn with these figures is the fact that for both coordinates, the main loss of realism takes place around the perigee, that is when the orbital periods are half-integer. In fact, for both coordinates and in all of the eccentric cases, after the test statistic leaves the gray area, indicating realism, it bounces back to the gray area after moving past the perigee, leaving a pattern of peaks. These peaks are thinner in period, when the eccentricity is higher.

Finally, the exact values for which the realism is lost in each case are collected in Table 2.3.

		LEO - Eccentricity								
STM	GEO	0	0.1	0.2	0.3	0.4	0.5	0.6	0.7	0.8
Cartesian Y–A	0.67	0.47	0.52	1.32	1.38	1.42	1.45	1.46	0.49	0.48
Curvilinear Y–A	10.42	16.48	4.25	2.37	2.35	2.37	2.4	2.42	1.47	0.48

Table 2.3: Number of orbital periods for the CvM test before failure for the GEO and all the cases of the LEO

Chapter 3

Dynamical Models

3.1 Introduction

This part of the dissertation describes the dynamical models that will be used throughout the rest of this work. The three-body problem describes the interaction of 3 bodies modeled as point-mass particles moving under their mutual gravitational attraction. Following Newton's Law of Universal Gravitation, the motion of one of these bodies with respect to a fixed point in an inertial frame, $\mathcal{I}$, can be described by

$$\frac{d^2\mathbf{r_i}}{dt^2} = -\sum_{j=1, i\neq j}^{3} G\frac{m_j \mathbf{r}_{ij}}{r_{ij}} \qquad \text{where} \quad i = 1, 2, 3; \tag{3.1}$$

where $\mathbf{r_i}$ is the position vector of the i-body relative to the origin of $\mathcal{I}$, O; m_j is the mass of the j-body; $\mathbf{r_{ij}}$ is the position vector of the i-body with respect to the j-body; and G is the universal gravitational constant of value $G = 6.67408 \cdot 10^{-20}\,\mathrm{km^3 kg^{-1} s^{-2}}$. These differential equations involve 18 variables (3 position coordinates and 3 velocity coordinates per body), while having only 10 known integrals of motion, corresponding to the conservation of the whole system's linear momentum (6 integrals), angular momentum (3) and energy (1). Thus, no closed-form solution exists for the three-body problem.

Because of this complexity of the full three-body problem, different approaches have been applied for the study of the three-body problem through simpler models that depend on specific situations. The first approach that could arise is the study of it through a perturbed two-body problem. This approach can be applied when studying the motion of an object orbiting a massive body in a region where the third body influence is much smaller than the first, but yet relevant. In this way, the actual orbit of the perturbed problem still resembles a conic section, which is the path of the two-body problem. The most common application to this is high-altitude Earth satellites where the Lunar and even Sun gravitational effects impact their motion. However, in this investigation the study is centered on the motion around bodies, where the third body influence is so big that a three-body model is needed. This situation includes the motion around natural satellites of some Solar System's planets or missions to Mars where the Sun's influence is considerable. Nevertheless, due to the complexity of

considering the whole three-body problem, some other simpler models are typically used for this study. In particular, in this investigation, 3 different models are used that, from higher fidelity to lower, are: the Elliptic Restricted Three-Body Problem (ER3BP), the Circular Restricted Three-Body Problem (CR3BP) and the Hill Three-Body Problem (H3BP).

3.2 System Definition

Before studying in detail each of the three models used in this work, let first define a common system that will serve as a starting point for the three of them. The restricted three-body problem has mainly one simplification assumption with respect to the general three-body problem, but with high implications in terms of complexity reduction. Let P_1,P_2 and P_3 be the three bodies, with masses of m_1, m_2 and m_3, respectively, where $m_1 \geq m_2 \geq m_3$. Let assume that the mass of the third body is negligible compared to the one of P_1 and P_2, which will for now be called primaries, i.e. $m_3 \ll m_2$. This allows to remove the gravitational influence of P_3 on the motion of the two primaries from the formulation, which implies that the primaries' motion is described by the closed-form solution of the two-body problem. This is the similar situation for the reference orbit as the one described in the previous chapter. Even though the two-body problem determines that the bodies move along a conic that, in general, can be a closed curve (ellipse or circle) or an open one (parabola or hyperbola), only closed curves, i.e. an ellipse (the circle can be considered the limit case of an ellipse with $e = 0$), are considered in the restricted three-body problem. This is the reason behind the "elliptic" and "circular" in the name of the ER3BP and CR3BP, respectively.

Therefore, the two primaries move along a Keplerian elliptic orbit with a semi-major axis, a, and a mean motion, $n = \sqrt{G(m_1 + m_2)/a^3}$. In this sense, the units of length and time are equivalent to those of the two-body relative motion. In addition to the unit of mass, which is also needed in the three-body problem, the reference units are

$$LU = a, \qquad LU^P = \frac{p}{\gamma}, \qquad MU = m_1 + m_2, \qquad TU = \frac{1}{n} = \sqrt{\frac{a^3}{G(m_1 + m_2)}}. \tag{3.2}$$

With these normalized units, the mass ratio of the two primaries, $\mu = m_2/(m_1 + m_2)$, is defined as an essential parameter in the restricted three-body problem.

In order to ease the derivation of the equations of motion, these are derived in a rotating frame, where the two primaries are fixed, like it happened in the previous chapter. In this sense, the two same rotating frames are needed, $\mathcal{H}$ and $\mathcal{L}$, and are shown in Figure 3.1 along the inertial frame $\mathcal{I}$ that has the basis $\{\mathbf{i}', \mathbf{j}', \mathbf{k}\}$. This inertial frame has its origin in the barycenter of the primaries, around which they described elliptic orbits contained in the orbital plane that is shown in the figure.

3.3 The Elliptic Restricted Three-Body Problem

The ER3BP is the highest fidelity model of the ones used in this investigation and, therefore, also the most complex one. As in this model the reference orbit is an elliptic orbit, the

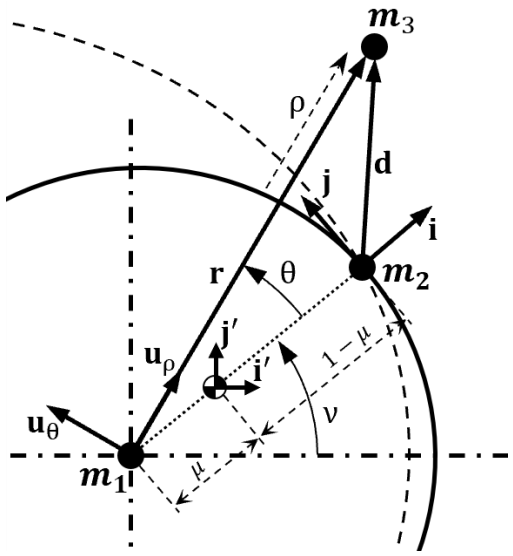

Figure 3.1: ER3BP parametrization and description of the different reference frames.

distance between the two primaries varies in time and the pulsating coordinates are used to define the system.

3.3.1 Derivation of the Equations of Motion in Curvilinear Coordinates

The derivation of the equations of motion of the ER3BP can be done following the same procedure as in Section 2.2 with some additional considerations. The first change is in the acceleration in the inertial frame

$$\left.\frac{d^2\mathbf{r}}{d\tau^2}\right|_{\mathcal{I}} = -\left(1-\mu\right)\frac{\mathbf{r}}{r^3} - \mu\frac{\mathbf{d}}{d^3}, \tag{3.3}$$

where $\mathbf{r}$ is the position of m_3 relative to the first primary and $\mathbf{d}$ its position with respect to m_2. The expression of $\mathbf{r}$ is the same as in the previous section defined by Eq. (2.8), while $\mathbf{d}$ can be written as

$$\mathbf{d} = \frac{\tilde{p}}{\gamma}\left(d_\rho \mathbf{u}_\rho + d_\theta \mathbf{u}_\theta + z\,\mathbf{k}\right), \tag{3.4}$$

with

$$d_\rho = r_\rho - \cos\theta, \qquad d_\theta = \sin\theta,$$

and

$$d = \frac{\tilde{p}}{\gamma}\sqrt{(r_\rho - \cos\theta)^2 + \sin^2\theta + z^2}. \tag{3.5}$$

Another difference is that this time the origin of the rotating frame $\mathcal{H}$ and the inertial frame $\mathcal{I}$ is not the same, the m_3 acceleration relative to $\mathcal{H}$ is now expressed as

$$\left.\frac{d^2\mathbf{r}}{d\tau^2}\right|_{\mathcal{H}} = \left.\frac{d^2\mathbf{r}}{d\tau^2}\right|_{\mathcal{I}} - \mathbf{a}_{\mathcal{H}} - 2\boldsymbol{\omega}_{\mathcal{H}} \times \left.\frac{d\mathbf{r}}{d\tau}\right|_{\mathcal{H}} - \boldsymbol{\omega}_{\mathcal{H}} \times (\boldsymbol{\omega}_{\mathcal{H}} \times \mathbf{r}) - \boldsymbol{\alpha}_{\mathcal{H}} \times \mathbf{r}, \tag{3.6}$$

where $\mathbf{a}_{\mathcal{H}}$ is the acceleration of m_1 (which is the origin of the $\mathcal{H}$ frame) with respect to the inertial frame $\mathcal{I}$, centered at the primaries' center of mass, and can be written as

$$\mathbf{a}_{\mathcal{H}} = \frac{\mu\left(\mathbf{r}-\mathbf{d}\right)}{\left|\mathbf{r}-\mathbf{d}\right|^3} = \left[\frac{\gamma^2}{\tilde{p}^2}\mu\left(r_\rho - d_\rho\right)\right]\mathbf{u}_\rho - \frac{\gamma^2}{\tilde{p}^2}\mu d_\theta \mathbf{u}_\theta. \tag{3.7}$$

Regarding the rest of the variables implicated, they have the same expressions as in the previous section and can be obtained by means of Eqs. (2.13), (2.14), (2.9) and (2.10). Therefore, replacing all these expressions together with Eq. (3.7) and (3.3) into Eq. (3.6), the differential equations for the ER3BP in pulsating curvilinear coordinates are finally obtained

$$\begin{cases} \rho'' = r_\rho\left(2+\theta'\right)\theta' + \dfrac{1}{\gamma}\left[(1-\mu)r_\rho\left(1-\dfrac{1}{\tilde{r}^3}\right) + \mu(r_\rho-\cos\theta)\left(1-\dfrac{1}{\tilde{d}^3}\right)\right] \\ \theta'' = \dfrac{1}{r_\rho}\left[-2\rho'\left(1+\theta'\right) + \dfrac{\mu\sin\theta}{\gamma}\left(1-\dfrac{1}{\tilde{d}^3}\right)\right] \\ z'' = \dfrac{z}{\gamma}\left[-e\cos\nu - \dfrac{1-\mu}{\tilde{r}^3} - \dfrac{\mu}{\tilde{d}^3}\right] \end{cases}, \tag{3.8}$$

where

$$\tilde{d} = \sqrt{(r_\rho - \cos\theta)^2 + \sin^2\theta + z^2}. \tag{3.9}$$

3.3.2 Characteristics of the System

The ER3BP is a non-autonomous system, as the period appears explicitly in the equations of motion through the true anomaly ν. As a consequence, for a given eccentricity, periodic orbits in the rotating frame appear as isolated solutions, with the period being an integer number of revolutions of the two primaries [58]. This implies that the period must be $T = 2\pi N$, where N is an integer, indicating a mean-motion resonance between the motion of the third body and that of the primaries. In this work, such orbits are simply referred to as resonant orbits. This terminology must not be confused with that used by some authors to describe orbits in the restricted three-body problem that are originated from a resonance in the two-body problem. In those cases, the period of the orbits does not need to be perfectly commensurate with that of the primaries.

However, when the eccentricity is allowed to vary, periodic orbits form infinite one-parameter varieties with a fixed period. Each of these varieties is referred to by various names in the literature, but in this work they will be called families. Each family usually shares a set of common dynamical properties but can be subdivided into branches separated by critical points, such as bifurcations or collision orbits, in which some of these properties may change.

3.3.3 Symmetries

Following a similar reasoning to Lukianov [59] but with curvilinear coordinates, the symmetries of the system can be studied. The first symmetry that arises is around the orbital plane, in which

$$(\rho, \theta, z, \rho', \theta', z', \rho'', \theta'', z'', \nu) \leftrightarrow (\rho, \theta, -z, \rho', \theta', -z', \rho'', \theta'', -z'', \nu)\ . \tag{3.10}$$

As a consequence, spatial orbits that are not symmetric with respect to the x-y LVLH plane, have associated another orbit that is mirrored to this one. This mirrored orbit can be easily obtained by applying a change of variable $z \to -z$.

The second symmetry comes from the called Mirror Theorem, that is characteristic of the N-body problem. This symmetry surges from the moment in which all the bodies possess a perpendicular velocity vector with respect to the radius vector to the center of mass [60], which established the origin of a reflective symmetry. The first condition needed for this is the alignment of the bodies with respect to the orbital plane, that in the ER3BP is indicated by the x-z plane of the LVLH frame. Owing to the elliptic nature of the primaries' orbit, the symmetry condition only takes place at both apses, i.e. $\nu = 0$ or $\nu = \pi$. From these restrictions, two different situations fulfill the Mirror Theorem condition. The first is when the state indicates a perpendicular crossing with respect to the x-z LVLH plane. This is achieved by a symmetry with respect to this plane accompanied by a change of the direction of ν, and corresponds to the second symmetry established by [59]

$$(\rho, \theta, z, \rho', \theta', z', \rho'', \theta'', z'', \nu) \leftrightarrow (\rho, -\theta, z, -\rho', \theta', -z', \rho'', -\theta'', z'', -\nu) \ . \tag{3.11}$$

The second condition takes place when the state corresponds to a x-axis perpendicular crossing. Again, this is achieved by a symmetry with respect to the axis for a reverse direction of time.

$$(\rho, \theta, z, \rho', \theta', z', \rho'', \theta'', z'', \nu) \leftrightarrow (\rho, -\theta, -z, -\rho', \theta', z', \rho'', -\theta'', -z'', -\nu) \ . \tag{3.12}$$

This condition can also be obtained by the combination of Eq. (3.10) and Eq. (3.11). Finally, when working with planar orbits, the Mirror Theorem turns into

$$(\rho, \theta, \rho', \theta', \rho'', \theta'', \nu) \leftrightarrow (\rho, -\theta, -\rho', \theta', \rho'', -\theta'', -\nu) \ . \tag{3.13}$$

This relation, which will be very important for the rest of the work, shows that the symmetric orbits can be propagated mirrored with respect to the x-axis of the LVLH frame or syzygy-axis, resulting in the same orbit. On the other hand, mirroring an asymmetric one leads to a different QSO, as will be observed later.

3.4 The Circular Restricted Three-Body Problem

The CR3BP is similar to the ER3BP, but, as the name establishes, it considers the two primaries to be in a circular motion. Hence, the CR3BP is considered a specific case of the ER3BP but with $e = 0$ and, consequently, its equations of motion in curvilinear coordinates are obtained by setting in Eq. (3.8) $e = 0$, $\tilde{p} = 1$, $\gamma = 1$ and $\tau = \nu$

$$\begin{cases} \ddot{\rho} = r_\rho \left(2 + \dot{\theta}\right) \dot{\theta} + (1-\mu) r_\rho \left(1 - \dfrac{1}{r^3}\right) + \mu (r_\rho - \cos\theta) \left(1 - \dfrac{1}{d^3}\right) \\ \ddot{\theta} = \dfrac{1}{r_\rho} \left[-2\dot{\rho} \left(1 + \dot{\theta}\right) + \mu \sin\theta \left(1 - \dfrac{1}{d^3}\right) \right] \\ \ddot{z} = -(1-\mu) \dfrac{z}{r^3} - \mu \dfrac{z}{d^3} \end{cases} . \tag{3.14}$$

Comparing the set of equations for the ER3BP (Eq. (3.8)) and CR3BP (Eq. (3.14)), an important difference arises. Whereas the ER3BP is defined by a set of non-autonomous differential equations where time appears explicitly, the CR3BP is defined by an autonomous one. Thus, CR3BP possesses an extra energy-like integral of motion known as the Jacobi constant. The Jacobi constant is derived by means of the pseudo-potential function. In Cartesian coordinates the derivation of the Jacobi constant is based on the function used by Szebehely [61] to describe the CR3BP. In Cartesian coordinates, this function is written as

$$U^*(x,y,z) = \frac{(1-\mu)}{r} + \frac{\mu}{d} + \frac{(x+1-\mu)^2 + y^2}{2}, \tag{3.15}$$

where $r = \sqrt{(x+1)^2 + y^2 + z^2}$ and $d = \sqrt{x^2 + y^2 + z^2}$. Taking into account that the potential function for the CR3BP in the inertial frame is

$$U(x,y,z) = \frac{(1-\mu)}{r} + \frac{\mu}{d}, \tag{3.16}$$

the U^* function is also called the pseudo-potential function. In curvilinear coordinates, the expression of the function is

$$U^*(\rho,\theta,z) = \frac{(1-\mu)}{r} + \frac{\mu}{d} + \frac{r_\rho^2 - 2\mu r_\rho \cos\theta + \mu^2}{2}. \tag{3.17}$$

Using the gradient of this function, Eq. (3.14) can be rewritten as

$$\begin{cases} \ddot{\rho} - r_\rho \left(2 + \dot{\theta}\right) \dot{\theta} = \dfrac{\partial U^*}{\partial \rho} \\ r_\rho \ddot{\theta} + 2\dot{\rho}\left(1 + \dot{\theta}\right) = \dfrac{1}{r_\rho}\dfrac{\partial U^*}{\partial \theta} \\ \ddot{z} = \dfrac{\partial U^*}{\partial z} \end{cases}. \tag{3.18}$$

In order to obtain the Jacobi constant, the expression of the velocity in cylindrical coordinates is used as an auxiliary tool

$$\mathbf{v} = \dot{\rho}\mathbf{u}_\rho + r_\rho \dot{\theta}\mathbf{u}_\theta + \dot{z}\mathbf{u}_z. \tag{3.19}$$

Taking the dot product of this expression and Eq. (3.18) yields

$$\dot{\rho}\ddot{\rho} - r_\rho \left(2 + \dot{\theta}\right)\dot{\rho}\dot{\theta} + r_\rho^2 \dot{\theta}\ddot{\theta} + 2r_\rho \left(1 + \dot{\theta}\right)\dot{\rho}\dot{\theta} + \dot{z}\ddot{z} = \dot{\rho}\frac{\partial U^*}{\partial \rho} + \dot{\theta}\frac{\partial U^*}{\partial \theta} + \dot{z}\frac{\partial U^*}{\partial z}$$

$$\dot{\rho}\ddot{\rho} + r_\rho^2 \dot{\theta}\ddot{\theta} - r_\rho \dot{\rho}\dot{\theta} + \dot{z}\ddot{z} = \dot{\rho}\frac{\partial U^*}{\partial \rho} + \dot{\theta}\frac{\partial U^*}{\partial \theta} + \dot{z}\frac{\partial U^*}{\partial z}. \tag{3.20}$$

The Jacobi constant, JC, is then obtained by integrating both sides of Eq. (3.20) with respect to time, noting that the pseudo-potential function does not depend explicitly on time

$$\frac{1}{2}\left(\dot{\rho}^2 + r_\rho^2 \dot{\theta}^2 + \dot{z}\right) = U^* - \frac{JC}{2}. \tag{3.21}$$

Thus, incorporating U^* from Eq. (3.17), the final expression of the Jacobi constant in cylindrical coordinates is

$$JC = 2\frac{(1-\mu)}{r} + 2\frac{\mu}{d} + r_\rho^2 - 2\mu r_\rho \cos\theta + \mu^2 - \left(\dot{\rho}^2 + r_\rho^2\dot{\theta}^2 + \dot{z}^2\right). \tag{3.22}$$

The preceding Jacobi constant can be employed to establish a more convenient three-body energy parameter defined in [62]

$$\Gamma = \frac{JC - JC^{L_1}}{JC^{L_4} - JC^{L_1}}, \tag{3.23}$$

where JC^{L_1} and JC^{L_4} are the Jacobi constant evaluated at the Lagrangian points L_1 and L_4 or L_5, respectively. Conveniently for later use, Γ takes a value of 0 when the energy of m_3 equals to that of L_1 and increases for higher values of the energy, contrary to the classical Jacobi constant.

Thanks to this extra energy-like constant, unlike the ER3BP, in the CR3BP, for a given system, periodic orbits form one-parameter varieties or families. This characteristic facilitates the study of periodic orbits via continuation methods, which will be explained in the next chapter. In the case that the mass ratio μ is allowed to vary, one extra degree of freedom is added, so the solutions form a two-parameter variety. However, in this work, when the mass ratio is allowed to change, the period is fixed instead. Therefore, the extra degree of freedom is removed, and families corresponding to one-parameter varieties arise again.

Finally, the same symmetries showed for the ER3BP applied also to the CR3BP. The main difference is that the condition derived from the Mirror Theorem works no matter the position in which the perpendicular crossing is located with respect to the primaries' orbit.

3.5 The Hill Three-Body Problem

The final model used in this investigation is the H3BP, also known as the Hill approximation of the CR3BP or, simply, the Hill Problem. This system describes the motion of P_3 when moving in the proximity of the second primary and while the mass of this body is considerably smaller than the first primary, i.e., $\mu \ll 1$. In addition, this model considers the two primaries to move on a circular orbit, similarly to the CR3BP. Consequently, starting from the CR3BP in the LVLH frame, that is in Cartesian coordinates of the rotating frame with the origin in the second primary, Hill simplified the equations such that the equations of motion of the H3BP with the actual nondimensionalization are

$$\begin{cases} \ddot{x} = 2\dot{y} + 3x - \mu\dfrac{x}{d^3} \\ \ddot{y} = -2\dot{x} - \mu\dfrac{y}{d^3} \\ \ddot{z} = -z - \mu\dfrac{z}{d^3} \end{cases}. \tag{3.24}$$

Nonetheless, Hill used a different scaling so that the equations would not depend on any external variable, that is, that μ would disappear from the formulation. This is accomplished

by changing the length unit from a to

$$LU_H = a \cdot \mu^{1/3}. \tag{3.25}$$

Following the same nomenclature as Hénon used in [25], the new Hill Cartesian variables (ξ, η, ζ) relate with the classical Cartesian LVLH variables (x, y, z) by

$$x = \mu^{1/3}\xi, \qquad y = \mu^{1/3}\eta, \qquad z = \mu^{1/3}\zeta. \tag{3.26}$$

In this manner, the equations of motion for the H3BP become

$$\begin{cases} \ddot{\xi} = 2\dot{\eta} + 3\xi - \dfrac{\xi}{\varrho^3} \\ \ddot{\eta} = -2\dot{\xi} - \dfrac{\eta}{\varrho^3} \\ \ddot{\zeta} = -\zeta - \dfrac{\zeta}{\varrho^3} \end{cases}, \tag{3.27}$$

where $\varrho = \sqrt{\xi^2 + \eta^2 + \zeta^2}$.

Analogous to the Jacobi constant used in the CR3BP, Hill's approximation has its counterpart defined by Hénon [25], [26] for the planar case. In the full three-dimensional (3D) case, this constant is

$$JC_H = 3\xi^2 - \zeta^2 + \frac{2}{\varrho} - \left(\dot{\xi}^2 + \dot{\eta}^2 + \dot{\zeta}^2\right) \tag{3.28}$$

and it is related to the CR3BP Jacobi constant as

$$JC = 3 + \mu^{2/3} JC_H. \tag{3.29}$$

Similarly to the Γ parameter defined for the CR3BP, one can define

$$\Gamma_H = 1 - \frac{JC_H}{JC_H^{L_1}}. \tag{3.30}$$

This definition differs from the CR3BP one owing to the fact that Hill's problem does not admit the triangular equilibrium points. However, it still maintains the two main characteristics of the parameter, since it is also 0 when the energy is that of L_1 and it is directly proportional to the energy.

In addition, the behavior of the system is the same as that observed in the CR3BP. Therefore, it is an autonomous dynamical system, as it is defined by a system of equations in which the time does not appear explicitly. Moreover, periodic orbits form one-parameter families.

Finally, it is important to point out that it is not possible to obtain a "curvilinear analogue" of Hill's equations of motion where the dependency of the parameter μ can be made to disappear.

3.5.1 Symmetries

The same symmetries applied to both the CR3BP and the ER3BP, also apply to the H3BP. Accordingly, adapting them to the Hill's coordinates, the two symmetry conditions result

$$\left(\xi, \eta, \zeta, \dot{\xi}, \dot{\eta}, \dot{\zeta}, \ddot{\xi}, \ddot{\eta}, \ddot{\zeta}, \tau\right) \leftrightarrow \left(\xi, \eta, -\zeta, \dot{\xi}, \dot{\eta}, -\dot{\zeta}, \ddot{\xi}, \ddot{\eta}, -\ddot{\zeta}, \tau\right) , \tag{3.31}$$

$$\left(\xi, \eta, \zeta, \dot{\xi}, \dot{\eta}, \dot{\zeta}, \ddot{\xi}, \ddot{\eta}, \ddot{\zeta}, \tau\right) \leftrightarrow \left(\xi, -\eta, \zeta, -\dot{\xi}, \dot{\eta}, -\dot{\zeta}, \ddot{\xi}, -\ddot{\eta}, \ddot{\zeta}, -\tau\right) . \tag{3.32}$$

These two symmetries conditions can again be combined to obtain the third one

$$\left(\xi, \eta, \zeta, \dot{\xi}, \dot{\eta}, \dot{\zeta}, \ddot{\xi}, \ddot{\eta}, \ddot{\zeta}, \tau\right) \leftrightarrow \left(\xi, -\eta, -\zeta, -\dot{\xi}, \dot{\eta}, \dot{\zeta}, \ddot{\xi}, -\ddot{\eta}, -\ddot{\zeta}, -\tau\right) . \tag{3.33}$$

And in the case of a planar orbit, the same symmetry condition as in the other models applied

$$\left(\xi, \eta, \dot{\xi}, \dot{\eta}, \ddot{\xi}, \ddot{\eta}, \tau\right) \leftrightarrow \left(\xi, -\eta, -\dot{\xi}, \dot{\eta}, \ddot{\xi}, -\ddot{\eta}, -\tau\right) . \tag{3.34}$$

Apart from these conditions, the H3BP has an extra symmetry condition. This condition is analogous to the reflection of the x-z plane already studied, but to the y-z plane

$$\left(\xi, \eta, \zeta, \dot{\xi}, \dot{\eta}, \dot{\zeta}, \ddot{\xi}, \ddot{\eta}, \ddot{\zeta}, \tau\right) \leftrightarrow \left(-\xi, \eta, \zeta, \dot{\xi}, -\dot{\eta}, -\dot{\zeta}, -\ddot{\xi}, \ddot{\eta}, \ddot{\zeta}, -\tau\right) . \tag{3.35}$$

Again, this symmetry can be combined with the out-of-plane symmetry to obtain an equivalent symmetry condition

$$\left(\xi, \eta, \zeta, \dot{\xi}, \dot{\eta}, \dot{\zeta}, \ddot{\xi}, \ddot{\eta}, \ddot{\zeta}, \tau\right) \leftrightarrow \left(-\xi, \eta, -\zeta, \dot{\xi}, -\dot{\eta}, \dot{\zeta}, -\ddot{\xi}, \ddot{\eta}, -\ddot{\zeta}, -\tau\right) . \tag{3.36}$$

Finally, for the planar orbits, in addition to the condition 3.13, the extra condition is written as

$$\left(\xi, \eta, \dot{\xi}, \dot{\eta}, \ddot{\xi}, \ddot{\eta}, \tau\right) \leftrightarrow \left(-\xi, \eta, \dot{\xi}, -\dot{\eta}, -\ddot{\xi}, \ddot{\eta}, -\tau\right) . \tag{3.37}$$

Chapter 4

Numerical Methods for Periodic Orbits

Since there is no closed-form solution for any of the three dynamical systems used in this investigation, the computation of periodic orbits in these models requires the use of numerical techniques, such as differential correction algorithms. Moreover, periodic orbits are not isolated solutions, but rather come as a part of an infinite set of solutions. Accordingly, continuation schemes can be employed to generate a family of solutions starting from a single periodic orbit. As previously mentioned, this is the case in all three dynamical models employed in this work, as even in the ER3BP, in which strictly the solutions are isolated, families of orbits are found when the eccentricity is allowed to change. Among the various continuation methods proposed in the literature, the most commonly used are those based on differential correction algorithms. However, alternative techniques such as differential algebra mapping may also be employed, particularly in applications where computational efficiency is prioritized over accuracy [63], [64]. For these reasons, the computation of periodic orbits in this work, in particular periodic QSOs, will be based on the use of different continuation schemes, which are presented in the first part of this chapter. After that, the second part of the chapter focuses on the concept of linear stability, given its importance for detecting bifurcations between families of period orbits.

All the numerical techniques presented in this chapter were built in MATLAB (version 2022b) by the author. These in-house scripts were used to produce all the results presented throughout this thesis, with no third-party software employed.

4.1 Numerical Continuation Schemes

In this work, different numerical continuation schemes are used. These can be classified into two big categories, depending on the strategy followed when stepping into the new periodic orbit. These two schemes are the natural parameter continuation and the pseudo-arclength continuation, and they will be explained in detail below.

4.1.1 Natural Parameter Continuation: The Poincaré Method

The natural parameter continuation is composed of two steps, a first one where a step into one of the parameters of the system is done, hence the name, and a second step where a corrector is applied to close the orbit, keeping the stepping parameter fixed. The complexity in the first step can vary a lot from one methodology to another, where it can go to a pure step in the mentioned parameter with no other modification, to a predictor scheme where the rest of parameters are updated accordingly. This last approach is the one included in this work, where a fast and accurate numerical continuation scheme has been developed using a modified version of the predictor-corrector algorithm of Lara & Peláez (see [65]).

Regarding the specific continuation strategies employed in this investigation using natural parameter continuation, a wide range of possibilities is considered. First, there is the case of families of periodic orbits obtained within a specific system in the CR3BP or in the μ-independent H3BP. In such cases, any of the initial variables can be used as the stepping parameter, as well as the period of the orbit. Any other parameter of the periodic orbit could also be used for this task, such as the energy, but it is not considered in this work. A different situation arises when the family is obtained by changing the conditions of the system. This occurs in several contexts, including the transition between different planetary systems within the CR3BP, and the computation of periodic orbits in the ER3BP starting from solutions in the CR3BP. In these two cases, the stepping parameter is a physical parameter of the system: the mass ratio of the primaries, for the first case, or the eccentricity for the ER3BP. Another situation where μ is used as the continuation parameter is in transitioning an orbit from the H3BP to a certain system in the CR3BP. The reason behind this is the need to use an intermediate system with a smaller μ for the initial transition, which is then continued in μ. Due to its greater complexity, the continuation scheme is described in the following using the ER3BP as dynamical model and the eccentricity e as the continuation parameter, which will be represented by σ throughout this chapter.

Another aspect of the continuation that can vary is the targeting scheme used. For this explanation, a general periodicity constraint that can be utilized for any periodic orbit is used. However, later on, other targeting strategies that will simplify the continuation when symmetries can be leveraged will be explained.

Before the in-depth derivation of the equations of the predictor-corrector algorithm, since the continuation used in this work is based on Taylor's expansion, it will be essential to study the linear behavior of the system. In this sense, the State Transition Matrix (STM) becomes of great interest and, therefore, it will be introduced first.

The State Transition Matrix

The state transition matrix is a fundamental matrix of an orbital trajectory, and, in this work, of a periodic orbit, that linearly maps an initial deviation at an initial time ν_0 to a certain time ν. In this sense, considering the state vector

$$\mathbf{s} = (\rho, \theta, z, \rho', \theta', z')^T , \tag{4.1}$$

the mapping is defined by

$$\delta\mathbf{s}(\nu) = \Phi(\nu)\delta\mathbf{s}_0. \tag{4.2}$$

So the expression of the STM is

$$\Phi(\nu) = \frac{\partial \mathbf{s}}{\partial \mathbf{s}_0} = \begin{bmatrix} \frac{\partial\rho}{\partial\rho_0} & \frac{\partial\rho}{\partial\theta_0} & \frac{\partial\rho}{\partial z_0} & \frac{\partial\rho}{\partial\rho_0'} & \frac{\partial\rho}{\partial\theta_0'} & \frac{\partial\rho}{\partial z_0'} \\ \frac{\partial\theta}{\partial\rho_0} & \frac{\partial\theta}{\partial\theta_0} & \frac{\partial\theta}{\partial z_0} & \frac{\partial\theta}{\partial\rho_0'} & \frac{\partial\theta}{\partial\theta_0'} & \frac{\partial\theta}{\partial z_0'} \\ \frac{\partial z}{\partial\rho} & \frac{\partial z}{\partial\theta} & \frac{\partial z}{\partial z} & \frac{\partial z}{\partial\rho'} & \frac{\partial z}{\partial\theta'} & \frac{\partial z}{\partial z'} \\ \frac{\partial\rho'}{\partial\rho_0} & \frac{\partial\rho'}{\partial\theta_0} & \frac{\partial\rho'}{\partial z_0} & \frac{\partial\rho'}{\partial\rho_0'} & \frac{\partial\rho'}{\partial\theta_0'} & \frac{\partial\rho'}{\partial z_0'} \\ \frac{\partial\theta'}{\partial\rho_0} & \frac{\partial\theta'}{\partial\theta_0} & \frac{\partial\theta'}{\partial z_0} & \frac{\partial\theta'}{\partial\rho_0'} & \frac{\partial\theta'}{\partial\theta_0'} & \frac{\partial\theta'}{\partial z_0'} \\ \frac{\partial z'}{\partial\rho_0} & \frac{\partial z'}{\partial\theta_0} & \frac{\partial z'}{\partial z_0} & \frac{\partial z'}{\partial\rho_0'} & \frac{\partial z'}{\partial\theta_0'} & \frac{\partial z'}{\partial z_0'} \end{bmatrix}. \tag{4.3}$$

For the ER3BP, as well as for the CR3BP and the HR3BP, no analytical expression of the STM exists, so it must be obtained numerically. In order to do so, Eq. (4.2) is derived with respect to the independent variable

$$\delta\mathbf{s}'(\nu) = \Phi'(\nu)\delta\mathbf{s}_0. \tag{4.4}$$

Taking into account that the derivative of the state vector corresponds to the equations of motion $\mathbf{s}' = \boldsymbol{F}(\mathbf{s}, \nu)$ and performing a linear expansion, the Jacobian Matrix of the system, $\partial\boldsymbol{F}/\partial\boldsymbol{s}$, which possesses an analytical expression found in Appendix B for the ER3BP in curvilinear coordinates[1] and the Appendix C for the H3BP, can be utilized as

$$\frac{\partial\boldsymbol{F}}{\partial\mathbf{s}}(\nu)\delta\mathbf{s}(\nu) = \Phi'(\nu)\delta\mathbf{s}_0. \tag{4.5}$$

Finally, applying Eq. (4.2) to replace $\delta\mathbf{s}(\nu)$ and simplifying, the differential equation needed to obtain the STM numerically is obtained

$$\Phi' = \frac{\partial\boldsymbol{F}}{\partial\mathbf{s}}\Phi. \tag{4.6}$$

This equation is solved with the initial condition

$$\Phi(0) = \mathcal{I}. \tag{4.7}$$

[1]The expression of the Jacobian Matrix for the CR3BP in curvilinear coordinates can be obtained by just substituting $e = 0$ and considering that $\tau = \nu$ in this model.

Equations of the Predictor

In this section, the equations for the predictor step are derived. Consider the set of elliptic restricted three-body problems

$$\mathbf{s}' = \boldsymbol{F}\left(\mathbf{s}, \nu, \sigma\right), \tag{4.8}$$

where $\mathbf{s}\left(\mathbf{s}_0, \nu, \sigma\right) = \left(\rho, \theta, z, \rho', \theta', z'\right)^T$ is the curvilinear coordinates state vector, which depends on the initial state $\mathbf{s}_0$ and the true anomaly ν, and the parameter σ is the eccentricity. The ER3BP equations not only depend on the eccentricity but also on the mass ratio. However, as when working on the ER3BP the mass ratio is always fixed, it is not included in this formulation. Associate with the preceding set of differential equations the closure error function or periodicity constraint

$$\mathbf{g}(\mathbf{s}_0, T, \sigma) = \mathbf{s}_T - \mathbf{s}_0, \tag{4.9}$$

where $\mathbf{s}_T$ is the initial state $\mathbf{s}_0$ propagated for a period T, measured in terms of the true anomaly.

Assuming that, for the parameter value σ^0 and with initial conditions $\mathbf{s}_0^0$, a periodic solution $\mathbf{s}^0\left(\mathbf{s}_0^0, \nu, \sigma^0\right)$ of the preceding set of differential equations of period T^0 exists, one has

$$\mathbf{g}(\mathbf{s}_0^0, T^0, \sigma^0) = \mathbf{s}_{T^0}^0 - \mathbf{s}_0^0 = \mathbf{0}. \tag{4.10}$$

Now, apply a small change in the parameter $\sigma = \sigma^0 + \delta\sigma$ and seek the new initial conditions $\mathbf{s}_0^c = \mathbf{s}_0^0 + \delta\mathbf{s}_0$ corresponding to a periodic solution of period $T^c = T^0 + \delta T$. A "predicted" correction $(\delta\mathbf{s}_0^p, \delta T^p)$ (denoted with the 'p' superscript) can be computed expanding the closure error function about $\mathbf{s}_0^0$, T^0, σ^0

$$\mathbf{g}(\mathbf{s}_0^1, T^1, \sigma) \simeq \mathbf{g}(\mathbf{s}_0^0, T^0, \sigma^0) + \left[\frac{\partial \mathbf{g}}{\partial \boldsymbol{s}_0}\right]^0 \delta\mathbf{s}_0^p + \left[\frac{\partial \mathbf{g}}{\partial T}\right]^0 \delta T^p + \left[\frac{\partial \mathbf{g}}{\partial \sigma}\right]^0 \delta\sigma, \tag{4.11}$$

where $[.]^0$ indicates that the partials are evaluated at $(\mathbf{s}_0^0,\ T^0,\ \sigma^0)$. Since both $\mathbf{s}^0\left(\mathbf{s}_0^0, \nu, \sigma^0\right)$ and $\mathbf{s}^1\left(\mathbf{s}_0^1, \nu, \sigma\right)$ are periodic, Eq. (4.11) reduces to

$$\left[\frac{\partial \mathbf{g}}{\partial \boldsymbol{s}_0}\right]^0 \delta\mathbf{s}_0^p + \left[\frac{\partial \mathbf{g}}{\partial T}\right]^0 \delta T^p + \left[\frac{\partial \mathbf{g}}{\partial \sigma}\right]^0 \delta\sigma \simeq \mathbf{0}. \tag{4.12}$$

The first partial derivative appearing in Eq.(4.12) is a matrix and can be computed as

$$\left[\frac{\partial \mathbf{g}}{\partial \boldsymbol{s}_0}\right]^0 = \left[\frac{\partial \mathbf{s}_T}{\partial \boldsymbol{s}_0}\right]^0 - \left[\frac{\partial \mathbf{s}_0}{\partial \boldsymbol{s}_0}\right]^0 = \mathcal{M}^0 - \mathcal{I},$$

where $\mathcal{I}$ is the identity matrix and $\mathcal{M}^0$ is the monodromy matrix of the periodic solution $\mathbf{s}^0$. The monodromy matrix corresponds to the STM Φ propagated by one period T^0

$$\mathcal{M}^0 \equiv \Phi(T^0). \tag{4.13}$$

The second partial derivative in Eq. (4.12) is the state vector time derivative of $\mathbf{s}^0$ evaluated after one period

$$\boldsymbol{f}^0 = \left[\frac{\partial \mathfrak{g}}{\partial T}\right]^0 = \left[\frac{\partial \mathbf{s}_T}{\partial T}\right]^0 = [\mathbf{s}'_T]^0 = \boldsymbol{F}\left(\mathbf{s}^0_{T^0}, T^0, \sigma^0\right).$$

Finally, the third partial derivative in Eq. (4.12) is the partial derivative of the state vector with respect to the system parameter σ for the zero-order solution after one period

$$\boldsymbol{h}^0 = \left[\frac{\partial \mathfrak{g}}{\partial \sigma}\right]^0 = \left[\frac{\partial \mathbf{s}_T}{\partial \sigma}\right]^0$$

and can be obtained by a similar reasoning than the monodromy matrix. First, the vector function $\mathbf{q} = \partial \mathbf{s}/\partial \sigma$ is defined, in a similar way than the STM. After that, this function is propagated by means of its differential equation (see [65])

$$\mathbf{q}' = \frac{\partial \boldsymbol{F}}{\partial \boldsymbol{s}}\mathbf{q} + \frac{\partial \boldsymbol{F}}{\partial \sigma}, \qquad \mathbf{q}(0) = \mathbf{0}. \tag{4.14}$$

Finally, the desired vector corresponds to this function propagated by one period T^0

$$\boldsymbol{h}^0 \equiv \mathbf{q}(T^0).$$

Rearranging Eq. (4.12) in matrix form

$$A^0 \begin{bmatrix} \delta \mathbf{s}^p_0 \\ \delta T^p \end{bmatrix} = -\mathbf{h}^0 \delta\sigma, \tag{4.15}$$

where the 6×7 matrix is defined as

$$A^0 = \begin{bmatrix} \mathcal{M}^0 - \mathcal{I} & \boldsymbol{f}^0 \end{bmatrix}.$$

Eq. (4.15) represents a system of 6 algebraic equations with 7 unknowns (6 initial state variables corrections + 1 period corrections), that is, an under-determined system with an infinite number of solutions. This agrees with the analysis made until now, as in the ER3BP with variable eccentricity, the periodic orbits exist in families with infinite solutions.

In addition, this system of equations is general, so it can be adapted to other scenarios, such as the continuation in μ within the CR3BP, by just means of establishing $\sigma = \mu$ and simplifying the notation. In addition, this continuation procedure is also applicable for a fixed system in the CR3BP or the H3BP when the natural parameter is one of the parameters of the periodic orbit. In this case, even for the CR3BP the μ is fixed, so it is removed from the formulation. The selected parameter should be first removed from the unknowns, and then established as the stepping parameter σ. Using as an example the period as the continuation parameter, the system of equations would be

$$A^0 \delta \mathbf{s}^p_0 = -\mathbf{f}^0 \delta T, \tag{4.16}$$

with

$$A^0 = \begin{bmatrix} \mathcal{M}^0 - \mathcal{I} \end{bmatrix}.$$

In this case, there are 6 equations and 6 unknowns, but the system is still under-determined. The reason behind this is that as both are autonomous systems, they have a constant of motion represented by the Jacobi constant and, therefore, only 5 of the 6 equations are linearly independent. This, again, agrees with the fact that in this models the periodic orbits are organized in one-parametric families of infinite solutions.

After this point, two different strategies can be taken. First, this system can be augmented by incorporating some additional constraints such as phase or period constraints compatible with the specific problem at hand. Second, some of the unknowns or free variables can be removed from the formulation for the same reason. Continue with the main example presented here. For the continuation in eccentricity in the ER3BP, two different constraints are included. The first is that the period must be fixed, and the second constraint is made to determine the initial position within the orbit. In addition, for this example the planar case is considered, so the out-of-plane coordinates can be removed. Accordingly, one solution is to remove the period correction δT and, for example, the correction of θ', i.e. $\delta\theta'$, so that the system can be reduced to a 4×3 one

$$\tilde{A}^0 \begin{bmatrix} \delta\rho_0^p \\ \delta\theta_0^p \\ (\delta\rho_0')^p \end{bmatrix} = - \begin{bmatrix} h_1^0 \\ h_2^0 \\ h_4^0 \\ h_5^0 \end{bmatrix} \delta\sigma, \tag{4.17}$$

where

$$\tilde{A}^0 = \begin{bmatrix} m_{11}^0 - 1 & m_{12}^0 & m_{14}^0 \\ m_{21}^0 & m_{22}^0 - 1 & m_{24}^0 \\ m_{41}^0 & m_{42}^0 & m_{44}^0 - 1 \\ m_{51}^0 & m_{52}^0 & m_{54}^0 \end{bmatrix},$$

where m_{ij} represents the entry in the i-th row and j-th column of the monodromy matrix $\mathcal{M}$. The second strategy involves introducing the linear constraints as additional equations. Each additional constraint is written in general as

$$p_i(\mathbf{s}^0, T^0, \delta\mathbf{s}_0^p, \delta T^p) = \boldsymbol{\ell}_i^\top(\mathbf{s}^0, T^0) \begin{bmatrix} \delta\mathbf{s}_0^p \\ \delta T^p \end{bmatrix} = \mathbf{0}. \tag{4.18}$$

By adding the mentioned two constraint, the resulting system becomes a 6×5 one

$$\tilde{A}^0 \begin{bmatrix} \delta\rho_0^p \\ \delta\theta_0^p \\ (\delta\rho_0')^p \\ (\delta\theta_0')^p \\ \delta T^p \end{bmatrix} = - \begin{bmatrix} h_1^0 \\ h_2^0 \\ h_4^0 \\ h_5^0 \\ 0 \\ 0 \end{bmatrix} \delta\sigma, \tag{4.19}$$

where

$$\tilde{A}^0 = \begin{bmatrix} m_{11}^0 - 1 & m_{12}^0 & m_{14}^0 & m_{15}^0 & f_1^0 \\ m_{21}^0 & m_{22}^0 - 1 & m_{24}^0 & m_{25}^0 & f_2^0 \\ m_{41}^0 & m_{42}^0 & m_{44}^0 - 1 & m_{45}^0 & f_4^0 \\ m_{51}^0 & m_{52}^0 & m_{54}^0 & m_{55}^0 - 1 & f_5^0 \\ 0 & 0 & 0 & 1 & 0 \\ 0 & 0 & 0 & 0 & 1 \end{bmatrix}.$$

The solution of either Eq. (4.17) or Eq. (4.19) yields a first-order prediction of the periodic solution initial coordinates

$$\mathbf{s}_0^1 = \mathbf{s}_0^0 + \delta\mathbf{s}_0^p, \tag{4.20}$$

leading to the (approximately periodic) predicted solution $\mathbf{s}^1$ with period

$$T^1 = T^0 + \delta T^p, \tag{4.21}$$

where for the first case $\delta T^p = 0$.

Equations of the Corrector

Since the predictor step is based on a linear expansion while the models are non-linear, the solution obtained there needs to be corrected to obtain a closed periodic orbit. This is done by the corrector loop defined in this section. Following a similar scheme as for the predictor, the correction on each step n $\left(\delta\mathbf{s}_0^{n+1}, \delta T^{n+1}\right)$ can be obtained by solving a similar system of equations

$$\tilde{A}^n \begin{bmatrix} \delta\mathbf{s}_0^{n+1} \\ \delta T^{n+1} \end{bmatrix} = \begin{bmatrix} -\mathfrak{g}^n \\ p_1^n \\ p_2^n \end{bmatrix}, \tag{4.22}$$

where the matrix $\tilde{A}^n$ is built as in Eq. (4.19), but starting from the state vector achieved in the previous step (for the first corrector step it corresponds to the state coming from the predictor). In the same way, the closure error vector is obtained with the state got on the previous step

$$\mathfrak{g}^n = \mathfrak{g}(\mathbf{s}_0^n, T^n, \sigma) = \mathbf{s}_{T^n}^n - \mathbf{s}_0^n.$$

Finally the non-zero quantities

$$p_i^n(\mathbf{s}^0, T^0, \delta\mathbf{s}_0^{n+1}, \delta T^{i+1}) = \boldsymbol{\ell}_i^\top(\mathbf{s}^0, T^0) \begin{bmatrix} \delta\mathbf{s}_0^c \\ \delta T^c \end{bmatrix} = -\boldsymbol{\ell}_i^\top(\mathbf{s}^0, T^0) \begin{bmatrix} \mathbf{s}_0^n - \mathbf{s}_0^0 \\ T^n - T^0 \end{bmatrix} \tag{4.23}$$

are the constraints' violation terms corresponding to a corrector-induced variation of state variables that have been imposed as constant in Eq. (4.18). If instead of adding the additional constraints, they are used to remove some of the unknowns (Eq. (4.17)), they are still out in the corrector formulation.

The solution of Eq. (4.22) provides a new set of corrected initial coordinates

$$\mathbf{s}_0^{n+1} = \mathbf{s}_0^n + \delta\mathbf{s}_0^{n+1}, \tag{4.24}$$

leading to a nearly periodic solution with period

$$T^{n+1} = T^n + \delta T^{n+1}. \tag{4.25}$$

The corrector (Eq. (4.22)) has to be solved iteratively until a perfectly periodic orbit (within numerical precision) can be obtained

$$\mathbf{s}_0^c = \mathbf{s}_0^0 + \delta\mathbf{s}_0^p + \sum_n \delta\mathbf{s}_0^{n+1} \tag{4.26}$$

$$T^c = T^0 + \delta T^p + \sum_n \delta T^{n+1}. \tag{4.27}$$

In this work, a precision of at least 10^{-10} for the Euclidean norm of the error function has been used.

4.1.2 Pseudo-Arclength Continuation

Contrary to natural parameter continuation, in pseudo-arclength continuation the stepping is made along the tangent of the family, rather than stepping along a certain parameter. This approach, introduced by Keller [66], can be shown to be more robust in certain situations, but gives less control toward the process. In this way, the pseudo-arclength scheme cannot be used when trying to obtain a periodic orbit with a specific characteristic, such as a resonant period. For this reason, in this work, pseudo-arclength continuation is not used for continuing orbits in mass ratio μ or eccentricity e where a specific value is targeted, but for the continuation of families in the H3BP and the CR3BP within a specific system.

Like with the natural parameter continuation, pseudo-arclength is also divided into predictor and corrector, with a very similar formulation. To describe the scheme, this time a completely different situation is used as an example to cover a broad spectrum of algorithms. In this sense, the symmetries of each model studied in the previous chapter can be leveraged for symmetric orbits by the use of perpendicular crossing constraints. So, in the CR3BP, a symmetric orbit with respect to the x–z plane, possesses two perpendicular crossings to this plane, that separate the orbit into two symmetric parts. Therefore, starting from one of those orthogonal crossings

$$\mathbf{s}_0 = (\rho_0, 0, z_0, 0, \theta_0', 0)^T, \tag{4.28}$$

the other perpendicular crossing must be placed after half a period, leading to the perpendicular condition

$$\mathbf{g}(\mathbf{s}_0, T_{1/2}) = \begin{bmatrix} \theta_{T_{1/2}} \\ \rho'_{T_{1/2}} \\ z'_{T_{1/2}} \end{bmatrix} = \mathbf{0}.$$

This leads to a problem with 4 free variables collected in the vector $\mathbf{x} = (\rho_0, z_0, \theta_0', T/2)^T$.

From these constraints, following a similar procedure than the one applied to obtain Eq. (4.15), the equation for the predictor step of the pseudo-arclength continuation is obtained

$$\begin{bmatrix} \phi^0_{21}(T/2) & \phi^0_{23}(T/2) & \phi^0_{25}(T/2) & \theta'_{T/2} \\ \phi^0_{41}(T/2) & \phi^0_{43}(T/2) & \phi^0_{45}(T/2) & \rho''_{T/2} \\ \phi^0_{61}(T/2) & \phi^0_{63}(T/2) & \phi^0_{65}(T/2) & z''_{T/2} \end{bmatrix} \begin{bmatrix} \delta\rho_0^p \\ \delta z_0^p \\ (\delta\theta_0')^p \\ \delta\,(T/2)^p \end{bmatrix} = \mathbf{0} \longrightarrow A^0 \delta\mathbf{x}^p = \mathbf{0}, \tag{4.29}$$

where ϕ_{ij} is an entry of the STM matrix Φ. As no specific step on a certain parameter is forced like in the natural parameter continuation, the right side of the equation is a zero vector, and the system is homogeneous. Therefore, the solution of the system, beyond the trivial solution, is obtained through the null space of the matrix of the system. As the system is composed of three linearly independent constraints and four free variables, it is underdetermined and has a null space of dimension one, represented by the unit vector $\mathbf{v}^* = Null(A^0)$. This agrees with the fact that periodic orbits form one-dimension families, where the vector $\mathbf{v}^*$ corresponds to the tangent of the family as it comes from a linear system. In order to obtain this vector, the singular value decomposition (SVD) of the matrix A^0 is used. Once the desired size of the step is established, $\tilde{s}$, the prediction of this continuation is determined

$$\mathbf{x}^1 = \mathbf{x}^0 + \delta\mathbf{x}^p = \mathbf{x}^0 + \tilde{s}\mathbf{v}^*. \tag{4.30}$$

As for the corrector loop, the pseudo-arclength continuation adds an extra constraint known as the pseudo-arclength constraint

$$(\mathbf{x}^n - \mathbf{x}^0)^T \mathbf{v}^* - \tilde{s} = 0, \tag{4.31}$$

leading to the extending constraint vector

$$\tilde{\mathfrak{g}}^n = \tilde{\mathfrak{g}}(\mathbf{x}^n) = \begin{bmatrix} \mathfrak{g}(\mathbf{x}^n) \\ (\mathbf{x}^n - \mathbf{x}^0)^T \mathbf{v}^* - \tilde{s} \end{bmatrix}. \tag{4.32}$$

Then, following reasoning similar to that used for the corrector of the natural parameter continuation, the equation for each corrector step n for pseudo-arclength is obtained

$$\begin{bmatrix} A^n \\ (\mathbf{v}^*)^T \end{bmatrix} \delta\mathbf{x}^{n+1} = -\tilde{\mathfrak{g}}^n \longrightarrow \tilde{A}^n \delta\mathbf{x}^{n+1} = -\tilde{\mathfrak{g}}^n. \tag{4.33}$$

This system is now a 4×4 system, therefore defined by a square matrix. Similar to the previous section, consequent iterations of this corrector equation are used, until the defined precision is obtained, leading to the corrected free variable vector

$$\mathbf{x}^c = \mathbf{x}^0 + \tilde{s}\mathbf{v}^* + \sum_n \delta\mathbf{x}^{n+1}. \tag{4.34}$$

4.1.3 Multiple Shooting Scheme

Until this point, all the algorithms presented corresponded to single shooting methods. However, especially when dealing with orbits of long periods or areas with a high sensitivity, utilizing a multiple-shooter algorithm can be advantageous in minimizing numerical integration errors [67]–[69]. Any of the continuation methods and types of algorithms showed previously can be utilized as a multiple shooter by the addition of "patch points" that separate the trajectory into several arcs. There are different ways in which a multiple shooting scheme can be implemented, with different levels of complexity. In this work, a very simple version is implemented, where each of the arcs in which the trajectory is subdivided is of equal time length. The total number of points needed will depend on the number of arcs that are wanted. Thus, for n arcs, a total of $n+1$ points are needed. Two of them correspond to the initial and final points already used for the single shooting method, while $n-1$ points will correspond to the added patch points. In this sense, each of these additional points adds a total of 6 new free variables, corresponding to the state of this point, and 6 constraints, which ensure the continuity between arcs. Therefore, they do not affect the behavior of the system of equations.

To show how the multiple shooting scheme is built, the example used in Section 4.1.1 is utilized. In addition, in this example only one additional patch point is used for simplicity, although any number of them can be used. First, the constraint vector is built by adding the continuity between the arcs to the single shooter constraint

$$\mathfrak{g}(\mathbf{s}_{1,0}, \mathbf{s}_{2,0}, T/2, \sigma) = \begin{bmatrix} \mathbf{s}_{1,T/2} - \mathbf{s}_{2,0} \\ \mathbf{s}_{2,T/2} - \mathbf{s}_{1,0} \end{bmatrix} = \mathbf{0}. \tag{4.35}$$

From this constraint vector, the equation for the predictor is obtained in the same way as before

$$A^0 \begin{bmatrix} \delta \mathbf{s}_{1,0}^p \\ \delta \mathbf{s}_{2,0}^p \\ \delta \left(T/2\right)^p \end{bmatrix} = - \begin{bmatrix} \mathbf{q}_1^0(T/2) \\ \mathbf{q}_2^0(T/2) \end{bmatrix} \delta\sigma, \tag{4.36}$$

where $\mathbf{q}_i$ is defined by Eq. (4.14) for each arc. In this case A^0 is the 12×13 matrix

$$A^0 = \begin{bmatrix} \Phi_1^0(T/2) & -\mathcal{I} & \boldsymbol{F}^0\left(\mathbf{s}_{1,T/2}, \nu_{1,T/2}, \sigma\right) \\ -\mathcal{I} & \Phi_2^0(T/2) & \boldsymbol{F}^0\left(\mathbf{s}_{2,T/2}, \nu_{2,T/2}, \sigma\right) \end{bmatrix}, \tag{4.37}$$

where $\mathcal{I}$ is the 6×6 identity matrix. It is important to note that the $\nu_{2,T/2}$ fictitious time is measured from $\nu_{2,0} = \nu_{1,T/2}$ where the patch point is located. Finally, the corrector equation can be defined following the same procedure as in Section 4.1.1 and the same reasoning as for the predictor.

4.2 Stability and Bifurcations

4.2.1 The Monodromy Matrix

As introduced, the Monodromy matrix of a periodic orbit is the STM propagated for exactly one period. The Monodromy matrix captures the linear stability of periodic orbits [70], so in this section their properties are studied in depth. All the dynamical models used in this work for the three-body problem are Hamiltonian systems. This implies that the Monodromy matrix is symplectic and, therefore, its eigenvalues, also known as Floquet multipliers or (characteristic) multipliers, come in reciprocal or multiplicative inverse pairs, so that the determinant is equal to 1 [71]. Additionally, as the Monodromy matrix is real, when an eigenvalue is complex, its conjugate pair is also an eigenvalue. Moreover, both the CR3BP and the H3BP are autonomous systems so they possess an extra energy-like constant and periodic orbits exist in families. As a consequence of this, two of the eigenvalues of the Monodromy matrix for these models are equal to 1 [72]. This pair is called the trivial pair. One of these trivial eigenvalues is associated with a shift in phase of the orbit, thanks to the fact that the system is time-invariant. The second of these eigenvalues is associated with the nearby solutions existing because of the integral of motion. However, the geometric multiplicity of this pair is 1 and, therefore, there is only one eigenvector associated and the pair is defective. This eigenvector corresponds to the derivative of the state vector, so it points along the tangent of the actual orbit. In order to obtain the direction corresponding to the tangent along the family, the generalized eigenvector is needed, since this direction has an associated change on the Hamiltonian and the period [70].

Focusing now on the circular case, there are two variable pairs of eigenvalues. Given the already mentioned characteristic of these eigenvalues, there are two possible situations: that each pair is independent of the other or that the values of both pairs are coupled. When they are independent, each of the pairs can be composed by either real or complex values. In the case a pair is real, the eigenvalues just have to be inverses and both are positives or negatives, i.e. λ_i and λ_i^{-1}. In the case they are complex, they need to be placed on the circular unit,

as they are the only complex numbers in which the reciprocal and conjugate are the same, i.e if $\lambda_i = a + bi$ with $|\lambda_i| = 1$ is an eigenvalue, its pair is $\bar{\lambda} = a - bi$. In order to have a complex eigenvalue that is outside of the unit circle, the two pairs must be coupled and have the same absolute value $|\lambda_i|$. In this sense, each of the members of one pair is placed on opposite sides of the unit circle and has its correspondent conjugate in the other pair. This means that if $\lambda_i = a + bi$ with $|\lambda_i| \neq 1$ is an eigenvalue of the Monodromy matrix, its pair is $\lambda_i^{-1} = (a - bi)/|\lambda_i|^2$ and also the conjugate of these two are eigenvalues, $\bar{\lambda_i} = a - bi$ and $\bar{\lambda_i}^{-1} = (a + bi)/|\lambda_i|^2$.

4.2.2 Linear Stability of Periodic Orbits

One of the main important information contained in the Monodromy matrix is that its eigenvalues measure the linear stability of the periodic orbit. In this sense, each eigenvalue can be classified into three different subspaces:

- **Unstable subspace.** Eigenvalues outside of the unit circle, $||\lambda_i| < 1$, are unstable. This means that an associated initial perturbation will grow in time far away from the periodic orbit.
- **Stable subspace.** An eigenvalue is stable when it is placed inside the unit circle, i.e. $|\lambda_i| < 1$. Perturbations within this subspace will flow back to the orbit.
- **Center subspace.** When an eigenvalue belongs to the unit circle, $|\lambda_i| = 1$, an initial perturbation in its correspondent subspace will stay in the vicinity of the orbit. This type of eigenvalues are also stable, in the sense that the perturbations remain bounded. However, they are not asymptotically stable as for the ones belonging to the stable subspace. [73] Some authors may refer to this as being marginally stable.

For a periodic orbit to be considered stable, all of their eigenvalues must be stable. Taking into account the possible scenarios for the eigenvalues described in the previous section, an orbit can only be stable if all of the eigenvalues of their Monodromy matrix belong to the center subspace, i.e. if all the eigenvalues are placed on the unit circle. The reason behind this is that, as they occur in pairs as described, for any asymptotically stable eigenvalue, their reciprocal is an unstable one. For this reason, pairs of eigenvalues outside of the unit circle are referred to as unstable in this work. In order to have a better notion on the stability of each pair of eigenvalues, a stability index can be used. Another common approach worth mentioning is the use of the Broucke stability diagram [58]. However, in this work some stability indices, introduced below, are used instead.

Stability Index

A stability index is a useful metric that gives information about the stability of a periodic orbit. There are several different definitions of stability indices in the literature, and two of them will be used in this work. The first of them is defined for each pair of eigenvalues as [73]

$$b_i = \lambda_i + \frac{1}{\lambda_i}, \tag{4.38}$$

and it is the one that will be referred to as stability index. So, each periodic orbit has three stability indices, one per each pair. The trivial pair has a value of 2. In terms of nomenclature, this pair has associated the b_3 index in this work. As for the other two pairs, depending on the value of the index, they are stable or unstable. For a pair to be stable, it has to be placed on the unit circle. This has associated a real value of the stability index of $-2 \leq b_i \leq 2$. In the case that the pair is placed on the real line, the stability index is still real, but this time it will have a value of $b_i < -2$ or $b_i > 2$, depending on whether they are located on the negative or positive side of the real axis. These values correspond to an unstable pair of eigenvalues formed by one stable and one unstable one. Finally, in the case that the two non-trivial pairs of eigenvalues are located outside of both the real line and the unit circle, the stability indices are complex and have the same real part $Re(b_1) = Re(b_2)$, which will be the one used for representation when this situation arises. Therefore, when the stability indices are complex, both pairs of non-trivial eigenvalues are unstable, no matter their value. A final aspect regarding this stability index is the order of the three indices that each orbit possesses. As mentioned, the trivial pair is always labeled as the last b_3. For 3D orbits, the other two pairs will be ordered randomly at the beginning of each family, keeping track of them afterwards to be consistent with the numeration. However, when an orbit is planar, outside of the trivial pair of eigenvalues, one of the pairs is associated with planar eigenvalues, whereas the other pair has eigenvalues with only out-of-plane components. For this reason, in planar orbits in this work, b_1 always corresponds to the in-plane motion and b_2 to the out-of-plane one.

As the b_i can reach very high levels for some orbits, which can make difficult the representation for some families, the second stability index used in this work is a derivation of that one by using a hyperbolic scale, following the same procedure as in [74]. In concrete, this index that will be referred to as hyperbolic stability index is defined as

$$s_i = \begin{cases} \dfrac{2\sinh^{-1}(b_i)}{\sinh^{-1}(2)} & \text{if} \quad b_i \in \mathbb{R} \\ \dfrac{2}{\sinh^{-1}(2)}\left(\sinh^{-1}(\mathrm{Re}(b_i)) + i\sinh^{-1}(\mathrm{Im}(b_i))\right) & \text{if} \quad b_i \in \mathbb{C}\setminus\mathbb{R} \end{cases}. \tag{4.39}$$

With this definition, the representation is better when the range of values of the stability index is extended but the limit values between stable and unstable index are the same. In this way, similar to b_i, when s_i is real $-2 \leq s_i \leq 2$ the correspondent pair of eigenvalues is stable and otherwise is unstable.

Finally, the last representation of the stability used in this work is the maximum norm of the vector of eigenvalues

$$\|\lambda\|_\infty. \tag{4.40}$$

This quantity indicates the eigenvalue with a bigger norm and, therefore the most unstable one in case that there is one. It also indicates when an orbit is completely stable, that is when it has the value of 1, which is the minimum value it can reach.

4.2.3 Bifurcations

Another important application of the Monodromy matrix's eigenvalues is their ability to detect and monitor bifurcations that may result in a new family. A bifurcation may also be associated with a change in stability. When a bifurcation leads to a new family, the so-called bifurcating orbit is common to both the original and the new family. While bifurcation theory has been thoroughly addressed in the literature (see, for example, [75] [76]), in this section, only the practical aspects of bifurcations in both the CR3BP and the H3BP needed for the rest of the work are introduced.

Type of Bifurcations

First, the different types of bifurcations that may be encountered in the circular version of the restricted three-body problem are examined. Most bifurcations in these models arise when a pair of eigenvalues, excluding the trivial pair, also reach the value 1. This situation can result from three different configurations of the involved pair of eigenvalues, each defining a distinct types of bifurcations, as represented in Figures 4.1a–4.1c:

- **Tangent bifurcation.** A tangent bifurcation takes place in a family when a pair of eigenvalues undergoes a change of stability by reaching the value $\lambda_i = 1/\lambda_i = 1$, which corresponds to a stability index of $b_i = 2$. In this situation, represented in Figure 4.1a the pair of eigenvalues goes from being on the unit circle to the positive real axis or vice-versa [77]. Depending on whether the situation leads to a new intersecting family and the stability of it, this type of bifurcation can be classified into three types:
  - Transcritical. In this type of bifurcation, a new family arises. In the same way the original family undergoes a change of stability from before to after the bifurcation, the new family also has a change of stability, but in the opposite direction than the original one. [75]
  - Pitchfork bifurcation. Like the previous type, in this bifurcation also a new family arises. This new family is divided intro two branches that emerge from the bifurcating orbit, both of them with the same stability. This bifurcation can be subdivided depending on whether the new family is stable or unstable. When it is stable, the bifurcation is a supercritical pitchfork; when it is unstable, it is called subcritical. [75]
  - Turning point or fold bifurcation. This last type is the only one of the tangent bifurcations in which there is no intersection with a new family. In addition to the change of stability occurring to the family at a fold bifurcation, a extremum in energy also takes place.
- **Period-doubling bifurcation.** This bifurcation occurs when one of the non-trivial pairs of eigenvalues reaches the value of $\lambda_i = 1/\lambda_i = -1$ or, what it is the same, a stability index of $b_i = -2$. Like it happened with the tangents bifurcation, this also has associated a change of stability with the eigenvalues switching between the negative real axis and the unit circle in either direction, as represented in Figure 4.1b. As its name indicates, this type of bifurcation takes place when the period is doubling. Hence,

following the properties of the STM, the pair of eigenvalues that were at -1 for one period, turns $\lambda^2 = 1$ for two periods. In this sense the new family that may arise from this bifurcation has twice the period of the original family and it is formed by twice the number of loops. [72]

- **Period-multiplying bifurcations.** Like it happened with the period-doubling bifurcations, for an integer number m that is higher than 2, a non-trivial pair of eigenvalues can reach the value of 1 after m periods of the original family. For this task, the mentioned pair of eigenvalues must reach a value that satisfies $\lambda = \sqrt[m]{1}$, so that $\lambda^m = 1$. All these roots are located on the unit circle and thanks to their symmetry, if λ is one of the mth-roots of 1, so it is $1/\lambda$ or, what it is the same, its conjugate. This is fulfilled when a pair of eigenvalues has the value of $\lambda_i = \cos(2\pi n/m) \pm \sin(2\pi n/m)i$, where both m and n are integer numbers and m is called multiplicity and n order. Regarding the stability index, this corresponds to a value of $b_i = 2\cos(2\pi n/m)$. Like with the previous bifurcation, this situation can result in a new family with m times a higher period and m times revolutions than the original family before reaching a periodic orbit. Unlike what happened for the period-doubling bifurcation, no change of stability takes place at this type of bifurcation, as the pair of eigenvalues of the original family stays within the unit circle, as illustrated at 4.1c. This is what makes the period-doubling bifurcation a special type of period-multiplying bifurcation, and the reason why it is studied apart. [78]

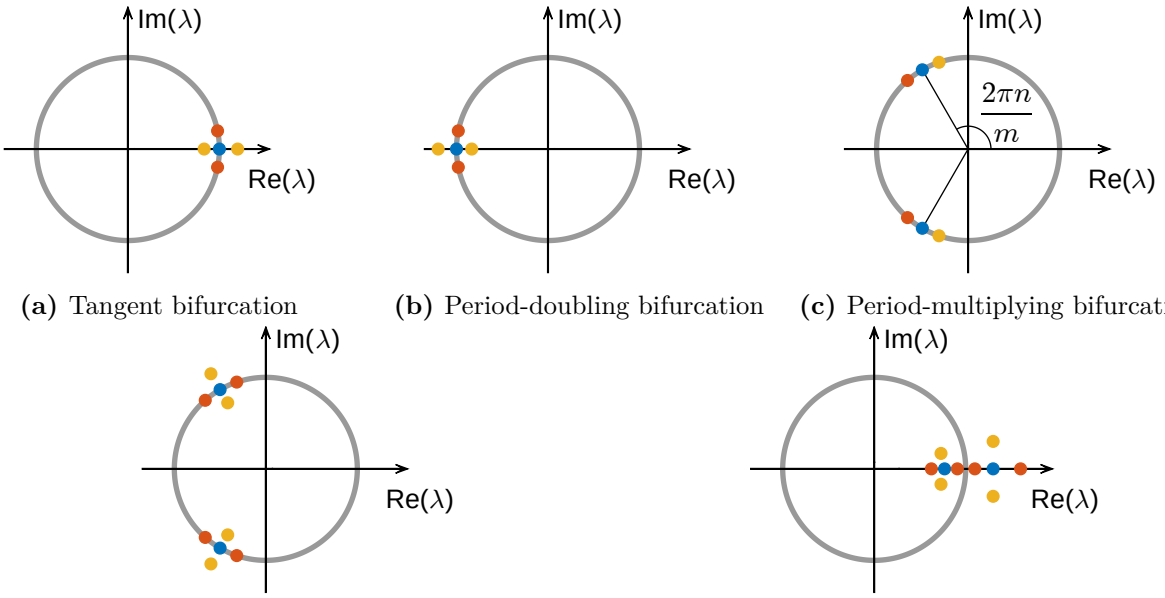

(a) Tangent bifurcation **(b)** Period-doubling bifurcation **(c)** Period-multiplying bifurcation

(d) Secondary Hopf bifurcation **(e)** Modified secondary Hopf bifurcation

Figure 4.1: Eigenvalues configuration for each type of bifurcation. Color legend: Blue indicates the bifurcation, while the other two (yellow and orange) indicate the configurations after and before the bifurcation.

Apart from these three types of bifurcations in which only one of the non-trivial pairs of eigenvalues is involved, there are other two special situations in which both non-trivial pairs are implicated:

- **Secondary Hopf bifurcation.** In this type of bifurcation, that is less common than the others, the two non-trivial pairs of eigenvalues collide anywhere on the unit circle, outside the values of ± 1. This is represented by having the two non-trivial stability indices reaching the same value comprised between -2 and 2. After that, both pairs leave the unit circle, going into the complex plane, as depicted in Figure 4.1d. While the two pairs of eigenvalues have complex values outside of the unit circle they are both coupled as mentioned before. This type of bifurcation involves a change in stability. [77]
- **Modified secondary Hopf bifurcation.** This type of bifurcation is similar than the previous one. The difference is that this time the two non-trivial pairs of eigenvalues collide at the real axis (outside of ± 1), before going into the complex plane, as represented in Figure 4.1e. Again this corresponds to an equality of both non-trivial eigenvalues, but this time outside the stable zone ($b_i < -2$ or $b_i > 2$). This time there is no change in stability. [77]

It is important to mention that, as these two types of bifurcations imply a coupling between the two non-trivial pairs of eigenvalues, they cannot be found in a planar case, where the in-plane and out-of-plane motion are completely independent. In fact, for planar orbits a four-dimensional (4D) Monodromy matrix only involving the in-plane coordinates could be used. In this case, there would be only one non-trivial pair. Nevertheless, in this work the six-dimensional (6D) Monodromy matrix is always used, in order to also have the information of the out-of-plane stability even when working with planar orbits. In contrast, tangent, period-doubling, and period-multiplying bifurcations appear in both 3D and planar cases. In fact, tangent bifurcations and period-multiplying bifurcations of multiplicity between 3 and 7 will play a significant role in this work.

Stepping into a New Family Through a Bifurcation

The last important question regarding bifurcations is how to step into the new family once a bifurcation is located. In this work all the new families obtained through a bifurcation are thanks to period-multiplying ones. Thus, as mentioned, the first thing needed is to propagate the bifurcating orbit for m periods to obtain a non-trivial pair of eigenvalues at 1. After that, the procedure for achieving an orbit that belongs to the new family varies depending on the continuation method that is used.

In the case of the natural parameter, the only information related to the new family is embedded in the eigenvectors and generalized eigenvectors associated to the eigenvalues of value 1. Nevertheless, this results in a subspace where both the new and the original family are found, as well as the direction along the orbit, as mentioned before. In this sense, the corresponding directions along the original family and the orbit are known, so they can be ruled out. However, the exact direction cannot be determined in most of the cases. One special case is that of the out-of-plane bifurcations, in which the direction of the new family is perpendicular of that of the original one, and then the direction is perfectly defined by that of the eigenvectors.

The next case is in which the continuation is done by means of pseudo-arclength. When a bifurcation leading to a new family is found and there are two pairs of eigenvalues of the

Monodromy matrix at 1, the system of differential equations built for the predictor step has a null space of two rather than one. [77] On accounting of the precision of the numerical method used to locate the bifurcation, in the SVD decomposition, the last singular value is small enough that can be considered 0. In this sense, the null space has a dimension of two and corresponds to the last two columns of the V matrix. The last one corresponds to the missing equation of the system and the second to last to the mentioned almost zero singular value. Out of them, the last column points in the direction of the original family. As for the other one, it cannot be assured that it points precisely in the direction of the new family, as it is always orthogonal to the other. However, it identifies the plane in which both families are located and usually gives a good enough initial guess to step into the new family. Therefore, when this situation arises, one must select between both basis depending on the objective. If the goal is to continue the original family, the last column should be used as $\mathbf{v}^*$. On the other hand, if the aim is to step into the new family, the second to last column must be used.

Chapter 5

Quasi-Satellite Orbits in the Hill Three-Body Problem

In the restricted-three body problem, there is a huge variety of families of periodic orbits. Among them, some of the most studied and used families are the ones around libration points, which include the famous Halo orbits. A great example of this is the NASA's Lunar Gateway which is set to be parked on a L_2 Near Rectilinear Halo Orbit (NRHO) [79]. However, in a system like Mars–Phobos, which has a very small mass ratio and in which the distance between the primaries is small, L_1 and L_2 are placed that close to the secondary that periodic orbits around them are infeasible. In this case, QSOs, also known as DROs, emerged as the best candidate as parking orbits thanks to their stability. This family of orbits is going to be the object of study of this work, as well as the different families that bifurcate from it.

As seen on the previous chapter, among the restricted-three body problem, in this work three different models are used. Out of them, two of them are based on circular orbits for the primaries, and for this reason periodic orbits in them are distributed in continuous families. Among them, the H3BP is the simplest one, and for this reason is the perfect candidate to first study the behavior of the QSOs. Accordingly, in this chapter, the main family of QSOs, as well as the different families that bifurcate from it, are studied in depth using the H3BP dynamical model. Even though the main focus of this work are planar orbits, in this chapter not only planar QSOs are studied, but also 3D ones for completeness.

5.1 Geometric Classification and Symmetry

Before starting exploring the different families of QSOs in the H3BP, it is useful to make a classification of the orbits depending on the shape that they have in this model. This geometric classification is made in the H3BP and depends on characteristics that will not be maintained when transitioning to more complex models, like the CR3BP and the ER3BP. However, for the orbits on these models the classification will be still the one according to their H3BP shape.

First, let start with the classification of the planar QSOs, that will be the main focus in

this work. The first differentiation made is between steady QSOs and swing QSOs, depending upon whether the LVLH trajectory corresponds to a simple closed curve (i.e. a Jordan curve) or it intersects itself. This will be kept for the CR3BP model, but in the ER3BP, as is well known (see, for instance, [34]), periodic orbits lead to LVLH-axes trajectories that are self-intersecting. Nevertheless, as already mentioned, all ER3BP orbits obtained starting from steady QSOs in the H3BP and CR3BP will continue to be referred to as "steady QSOs".

As will become clear in the following sections, steady QSOs formed a unique family composed by orbits with a simple and consistent shape. For this reason, there is no need for a further classification. However, the case of the swing QSOs is not as simple as it appears, as they belong to different families and have a greater variety of shapes. For this reason,it is convenient to establish a more extensive geometric classification of the different types of swing orbits.

The first level of classification is based on the degree of symmetry of the orbits in the H3BP model. Afterwards, for each degree of symmetry, the classification will be based on specific geometrical patterns of the swing motion, such as the location of the orthogonal syzygy-axis crossing point or the ratio of the maximum and minimum distance from the second primary.

With regard to the symmetry with respect to the x-axis, swing QSOs are first separated into symmetric and asymmetric. Symmetric swing QSOs are called doubly-symmetric if they are also symmetric with respect to the y-axis, and single-symmetric otherwise. The doubly-symmetric category can be further divided into two groups depending upon whether the position of the x-axis orthogonal crossing is the most external point (exterior-doubly-symmetric (EDS) or is an internal point (interior-doubly-symmetric (IDS)). As for the single-symmetric orbits, they can be mirrored around the y-axis producing a different periodic orbit. To account for these features, the prefix "left-" is added when referring to orbits extending more towards the negative x-axis and "right-" otherwise. In this way, two groups of single-symmetric swing QSOs are identified: left-single-symmetric (LSS) and right-single-symmetric (RSS). For the asymmetric QSOs, there is a similar consideration as any asymmetric orbit can be mirrored around the x-axis. This establishes two groups of asymmetric orbits: up-asymmetric (UA) and down-asymmetric (DA), where the prefix "Up-" refers to orbits extending more towards the positive y-axis and "down-" otherwise.

Among these characteristics, the symmetry with respect to the x-axis that the H3BP model possesses is shared with the CR3BP and the ER3BP. This is, however, not the case for the y-axis symmetry. The implications of these for the orbits on the CR3BP and the ER3BP are that: symmetric orbits will still be symmetric, doubly-symmetric QSOs will no longer have the y-axis symmetry, LSS and RSS QSOs will no longer be a perfect reflection of one another, and UA and DA will be still a mirror of each other.

Finally, for the 3D QSOs, the classification made for the planar orbits is kept for the two-dimensional (2D) projection of the orbits. In addition to this, the out-of-plane motion is characterized depending on the degree of symmetry with respect to the x-y plane. In this sense, the orbits that are symmetric with respect to this plane are called z-symmetric with no further characterization needed, and the orbits that are asymmetric from this plane are subdivided into two categories: northern, when they extend more towards the positive z and

southern, when they are towards the negative one. Similarly to the asymmetric QSOs, each northern QSO can be mirrored with respect to the x-y plane to obtain their southern version, as they are a perfect mirror from each other.

5.2 Steady QSOs

5.2.1 Initial Guess

For the symmetry properties mentioned, a steady planar QSO crosses the x-axis or syzygy-axis orthogonally, not only in the H3BP but also in the CR3BP. This implies that $\dot{\xi} = 0$ (or $\dot{\rho} = 0$ in the CR3BP) at the two x-axis crossing points ($\eta = 0$, $\xi \lessgtr 0$ or $y = 0$, $x \lessgtr 0$) when initial conditions can be most conveniently obtained, due to the use of perpendicular crossing algorithms. In this case, and with no loss of generality, the initial reference condition is placed at $\xi_0 < 0$. So, it is necessary to determine, for a given period, the value of x_0 and $\dot{y}_0$ closing the orbit. The first step to do this is using Baresi's "Linear Model" (LM) [37] to obtain a first guess on ξ_0 for a certain period. This model establishes a relation between the orbital frequency, n, and the size of the orbit, where the orbital frequency is related to the orbital period as

$$n = \frac{2\pi}{T}. \tag{5.1}$$

Applying this model to the negative orthogonal x-axis crossing, the relation with the frequency is

$$n_{QSO} \approx 1 + \frac{\mathcal{K}}{\pi |\xi_0|^3}, \tag{5.2}$$

$$\xi_0 \approx -\left[\frac{\mathcal{K}}{\pi\left(n^C_{steady} - 1\right)}\right]^{1/3}, \tag{5.3}$$

where $\mathcal{K}$ represents the complete elliptic integral of the first kind evaluated with a modulus $k = \sqrt{3}/2$ and has a value of $\mathcal{K} = 2.156516$. This approximation is valid as long as $|\xi_0| > 3.36$, which implies $n < 1.0181$. Choosing for the initial guess $n^0 = 1.015$, which corresponds to $T = 6.19033035190107$, one obtains $\xi_0^0 = -3.57687552763255$, where the 'zero' superscript indicates that is the first guess.

The next step is to obtain an approximation for $\dot{y}_0$. As the chosen value of frequency is close to $n = 1$, the periodic solution for the two-body relative motion is used (in the two-body problem periodic solutions of the relative motion exist only for the exact 2π relative period). This periodic solution for the planar case, in the x-axis perpendicular crossing is established by

$$\dot{y}_0 = \sqrt{\frac{1 - x_0}{1 + x_0}} - (1 + x_0)\,. \tag{5.4}$$

Due to the special non-dimensionalization of the H3BP, the first thing that is needed is an auxiliary μ to transform the initial position from ξ_0 to x_0. By choosing $\mu = 1 \cdot 10^{-8}$, transforming ξ_0 into x_0, applying Eq. (5.4) to compute $\dot{y}_0$, and transforming it back into the H3BP to obtain $\dot{\eta}_0$, the initial guessed state becomes

$$\mathbf{s}_0^0 = \begin{bmatrix} -3.57687552763255 & 0 & 0 & 0 & 7.16763983986206 & 0 \end{bmatrix}. \tag{5.5}$$

Next, a perpendicular crossing corrector is applied, in this case with the period fixed, to obtain the final QSO with $T = 0.985221674876847$ and initial state

$$\mathbf{s}_0 = \begin{bmatrix} -3.57559083288187 & 0 & 0 & 0 & 7.19020805179514 & 0 \end{bmatrix}. \tag{5.6}$$

Figure 5.1 shows the trajectory from both the initial guess state and the closed QSO from the corrected state. It can be observed that the initial guess was already close enough to the actual solution and how the corrector successfully refined it.

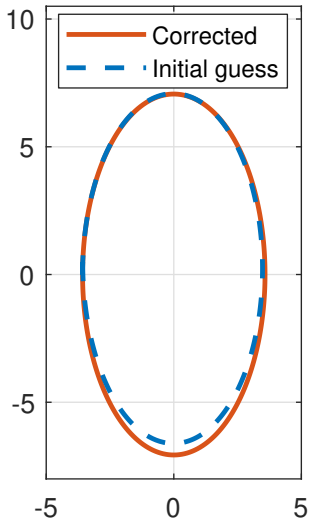

Figure 5.1: QSO of $T = 6.19033035190107$ corrected and with its initial guess.

5.2.2 Family of Steady QSOs

As explained in Chapter 3, periodic orbits within the H3BP, as well as within the CR3BP, belong to one-parameter families. As for the defined steady QSOs, they belong to one family that will be referred to as the steady QSO family (it is also known as the DRO family in the literature). Starting from the QSO obtained in the previous subsection, the rest of the family can be computed via natural parameter continuation (Section 4.1.1) or via pseudo-arclength continuation (Section 4.1.2). In this investigation, both methods have been used for the generation of families of periodic orbits in the H3BP. In addition, a single-shooting x-axis perpendicular crossing algorithm is used to compute the QSO family.

This family is shown in Figure 5.2, where in (a) some representative members of the family are shown colored by their Γ value; (b) reflects the evolution of the initial position, ξ_0, and the Γ as a function of the orbital period (normalized with the non-dimensional period of the second primary, i.e. 2π); and (c) illustrates the evolution of the stability indices with the orbital period over 2π. Figure 5.2c also includes the stability index values at which bifurcations take place. It also includes a shaded area, indicating the region of stability. This region is limited on the upper part by the 'TB' line, which corresponds to the tangent bifurcation, and on the lower part by the 'P2' line, the period-doubling bifurcation.

As it can be seen in the figure, the DRO family is characterized by stable retrograde orbits, symmetric around both the x-axis and the y-axis. The family exists for period values between

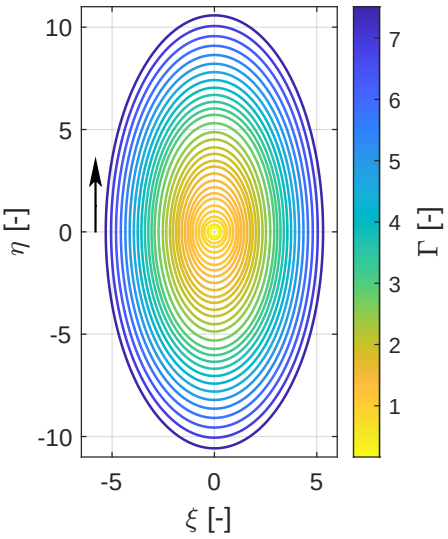

(a) Steady QSO family

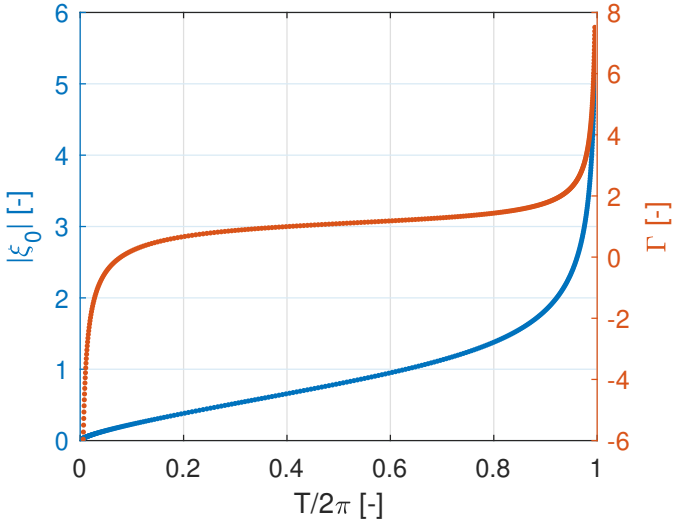

(b) Initial position and energy evolution

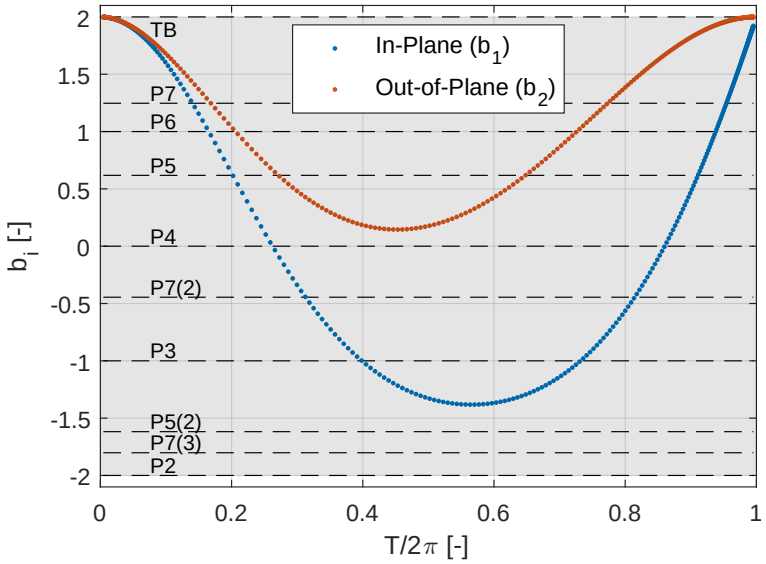

(c) Stability evolution with the bifurcations lines

Figure 5.2: QSO family in the H3BP

0 and 1. More specifically, the limits of the family are: on one side, it tends, asymptotically, to a null period and a null initial distance, with a decreasing Γ value; and on the other side, it tends asymptotically to a period of 1 with both the initial distance and the Γ value increasing. Let recall that the initial position takes place at the x-axis, in one of the two perpendicular crossings, so ξ_0 indicates the initial distance. In addition, due to the symmetry of the family and the symmetry of the model, the initial point could be at both sides of the x-axis (negative or positive), with the same absolute ξ_0. This is the reason why in Figure 5.2b $|\xi_o|$ is depicted, representing both possible initial positions.

Finally, regarding the bifurcations that arise from the QSO family, Figure 5.2c shows that for the in-plane index (i.e. the one whose eigenvectors belong to the orbital plane) there are

12 bifurcating orbits, all of them corresponding to period-multiplying bifurcations (it may look like there could be a tangent bifurcation either around period 0 or around period 1, but the family tends asymptotically to the 'TB' line for both the in-plane and the out-of-plane indices). These bifurcations for in-plane motion come in pairs, starting from the period-tripling bifurcation and going up to the period-septupling bifurcation. This last bifurcation has two different pairs, each of it corresponding to two different stability indices, i.e. two different orders of the period-septupling bifurcation.[1] More bifurcating orbits could arise for higher period-multiplying bifurcations, but in this work the maximum multiplicity considered is 7. In the following section, the families derived from these 12 bifurcation orbits are studied.

Even if in this work the main focus is the planar orbits, the 3D families that arise from the family of steady QSOs will also be derived at the end of this chapter. Therefore, Figure 5.2c shows that for the out-of-plane stability index, there are 6 different bifurcating orbits. Similarly to the in-plane case, these orbits come in pairs, being this time two for 'P5', two for 'P6' and two for 'P7' (specifically the one of order 1).

5.3 Planar Families of Swing QSOs

In this section, the different 2D families that bifurcate from the QSO single periodic family are studied. All these families of orbits come from period-multiplying bifurcations. Therefore, they are no longer formed by steady QSOs, but, in this work, they are referred to as swing QSOs, as explained. Following the classification made in Section 5.1, there are two types of families of orbits according to the x-axis symmetry, the symmetric and the asymmetric. However, it is important to remark that the so called asymmetric orbits or asymmetric families are indeed symmetric with respect to the y-axis for the H3BP model. This symmetry is possible due to the doubly-symmetry characteristic of the planar H3BP. In contrast, for the planar CR3BP and the ER3BP models there is only the symmetry around the x-axis. Therefore, the so called asymmetric orbits are certainly asymmetric in these models, and that is the reason behind this name.

5.3.1 Symmetric Swing QSOs

Starting from the 12 bifurcation orbits for the in-plane stability index stated in Figure 5.2c, different families arise. Like the QSO family, these families are computed with an x-axis perpendicular crossing targeter, but this time implementing a multiple shooting algorithm, as it aids the continuation for long period orbits such as the ones of these families. The swing families are shown in Figure 5.3, where the evolution of the initial distance to the second primary and the energy with respect to the reduced period of the orbit, T^*, over 2π is represented. The reduced period is the period divided by the number of loops or multiplicity of each family, so they can be represented together in the plot.

[1] The period-septupling bifurcation has a total of three orders but the QSO family possesses bifurcation orbits for only two of them. The period-quintupling bifurcation also has more than one order, specifically two, but only one is crossed by the in-plane index. The rest of multiplicities studied in this work have only one order.

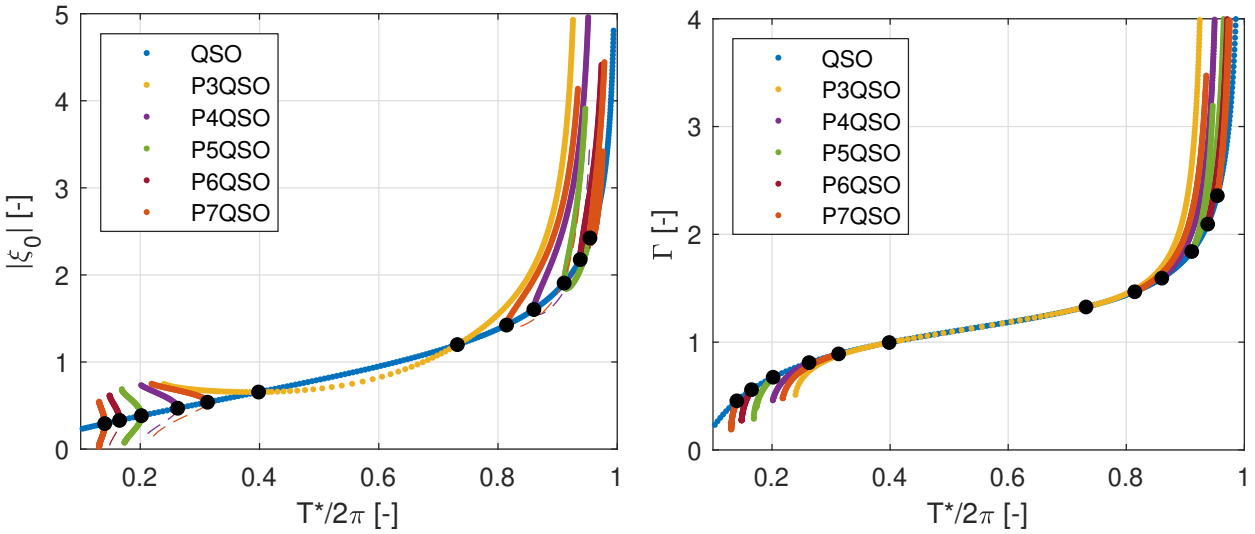

(a) Initial position evolution

(b) Energy evolution

Figure 5.3: Swing and steady QSO families tree in the H3BP

All these families will be studied thoroughly below, but there are some aspects of the figure that are worth mentioning now. The first important characteristic of the figure is the distribution of the families. There are 11 families, instead of the 12 that could be expected, as the P3QSO is an unique family that crosses the QSO twice, in each of the period-tripling bifurcating orbits. Excluding this family, which will be studied separately, the other 10 families can be divided into high-energy and low-energy ones. In this way, as each type of bifurcation comes in pairs, there is one high-energy family and one low-energy family for each type of bifurcation (counting the 'P7' bifurcation and the 'P7(2)' bifurcation as two different types). The second aspect that is important to mention is the fact that the families shown in the figure do not always represent the totality of them. As it will be seen later, some of these families lead to what is called a collision orbit that, if continued, results in orbits with prograde parts. However, in this figure only the fully retrograde orbits are shown, for clarity. The orbits that have both retrograde and prograde or direct motion are called mixed orbits in this work. Finally, some of the families have a part in which a dashed line appears. This is due to the existence of two perpendicular crossings, in which the initial position can be found, and will be explained below when those families are examined in depth.

P3QSO

The first family studied is the P3QSO that, as recalled, is a special case among the families of swing QSOs. Let the composition of this unique family be studied through Figure 5.4. This family crosses the family of steady QSOs twice, in the orbits called 'B1' and 'B2' in the figure. In addition, there is also a collision orbit, called as 'C', separating the fully retrograde orbits with orbits that have both a retrograde and a prograde motion part. With these 3 orbits as limits, there are a total of 4 characteristic branches of the orbit, 3 fully retrogrades and a final one with mixed conditions. Alongside these orbits that indicate the separation between branches, in Figure 5.4 some other orbits are remarked. For each of the three fully

retrograde branches, one orbit is selected to exemplify the behavior of the branch. In contrast, for the branch with mixed motion, three different orbits are highlighted, as the evolution of this branch is more complex. These orbits illustrate the characteristic shape of each branch and aid in understanding the family. This more in-depth study is done below with the help of Figure 5.5.

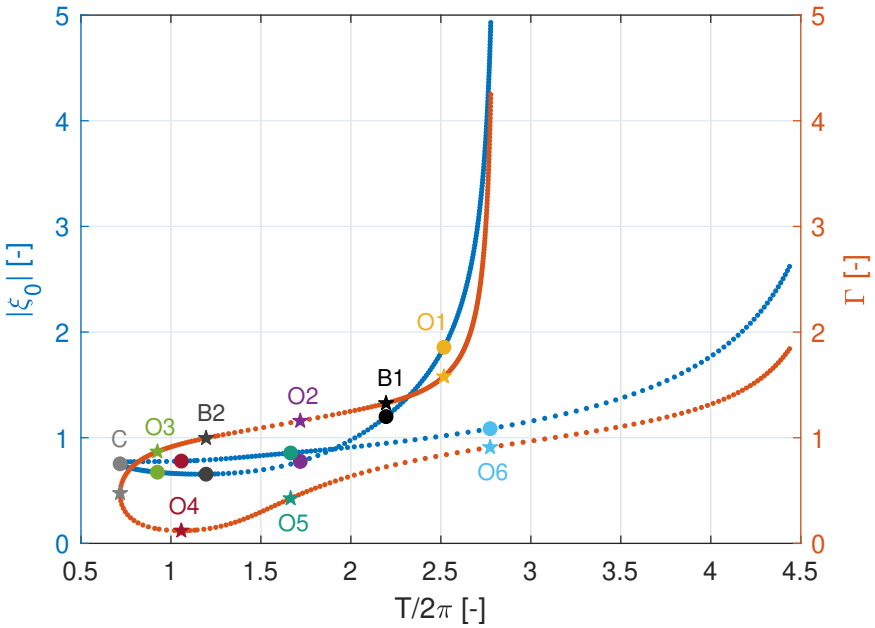

Figure 5.4: Initial position and energy evolution of the P3QSO family in the H3BP

In Figures 5.5a and 5.5b, the first 2 branches are shown. In (a), the 4 highlighted orbits of these 2 branches are shown, while in (b), the evolution of the hyperbolic stability indices, s_i, with the period over 2π is depicted, with the 4 mentioned orbits remarked. The hyperbolic stability index is used in this figure instead of the normal one due to the high values of the index, in order to improve the representation. Throughout this chapter, the use of the b_i index will be applied when possible, and only when one of the indices reaches high values (in any side of the axis), the hyperbolic one will be used as a representation tool.

The first branch starts from the 'B1' bifurcating orbit and evolves while the initial distance, energy and stability index are increasing, but it has a limit in period that is reached asymptotically. The orbit 'O1', colored in yellow, belongs to this branch and shows, in (a), that the branch is formed by doubly-symmetric orbits in which both perpendicular crossings are placed in the exterior part of the orbit. These orbits, according to the classification in Section 5.1 are called EDS. As for the linear stability of the branch, it can be studied with Figure 5.5b, where let recall that the shaded area indicates the stable or elliptic region and outside of it is the unstable or hyperbolic. With respect to the in-plane stability index, this branch starts in a stable orbit with a stability index of $s_1 = b_1 = 2$, characteristic of a tangent bifurcation, but the rest of the branch is composed of unstable orbits, in terms of the in-plane motion. As for the out-of-plane stability, starting from the bifurcating orbit, at the beginning of the branch the orbits are stable up to a certain period, but they become unstable from there. It is important to notice that, as in the figure what is represented is the hyperbolic

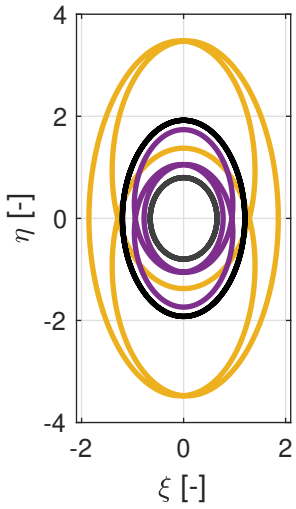

(a) 1st EDS and IDS branches

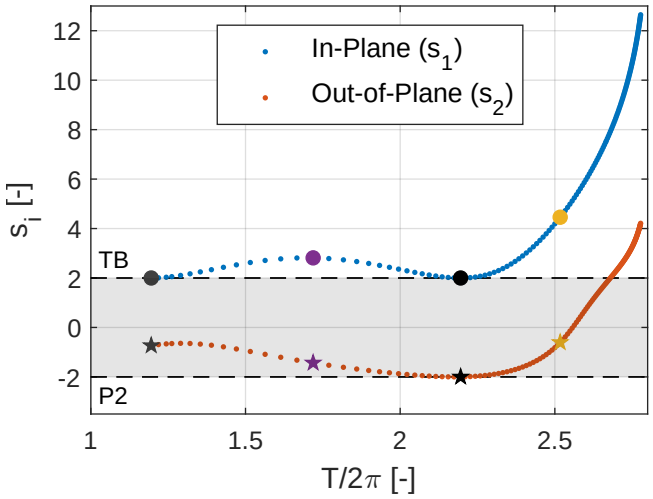

(b) Stability evolution of the 1st EDS and IDS branches

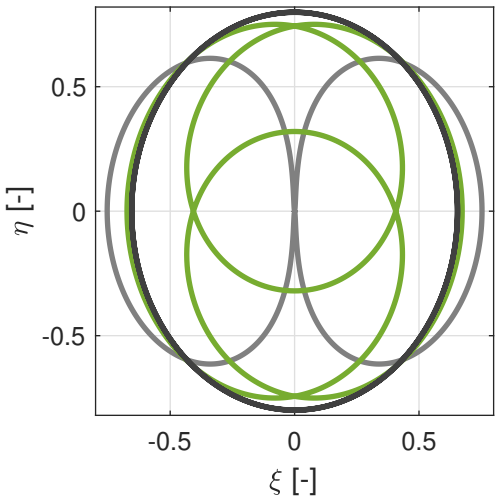

(c) 2nd EDS branch

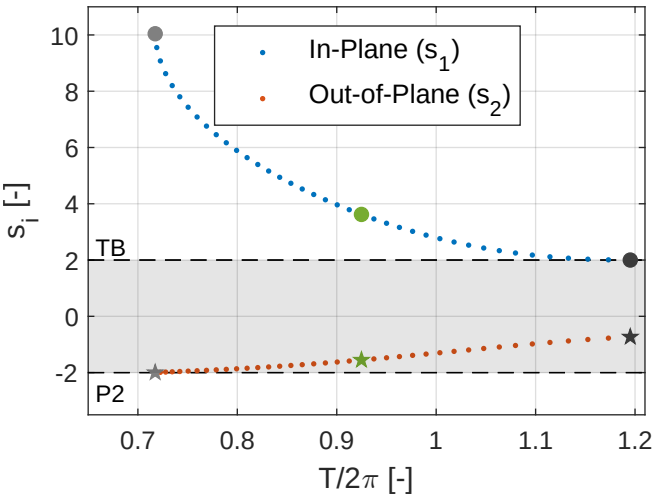

(d) Stability evolution of the 2nd EDS branch

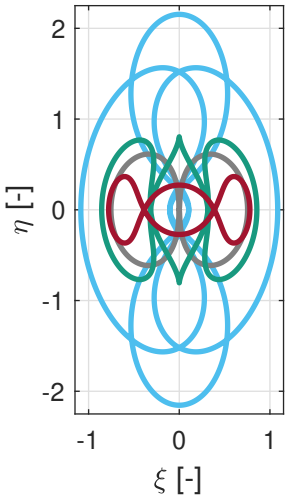

(e) Mixed EDS branch

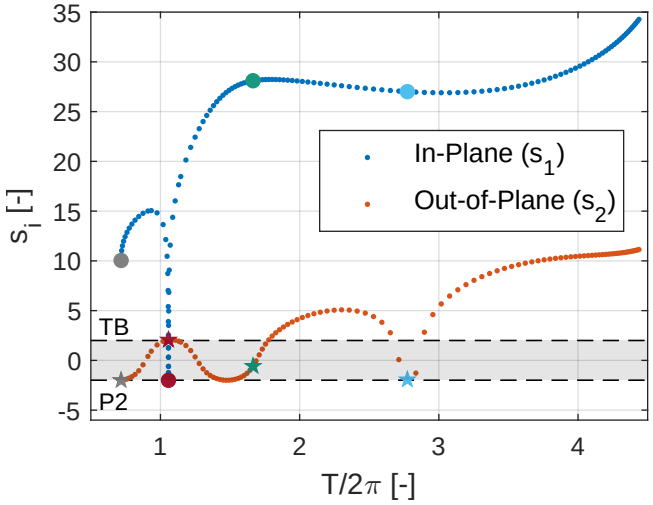

(f) Stability evolution of the mixed EDS branch

Figure 5.5: P3QSO family in the H3BP

stability index, the growth observed for high periods corresponds to an even more exponential growth of the normal stability index. Therefore, the orbits become highly unstable as the branch evolves.

The second branch is located between the two bifurcating steady QSOs, 'B1' and 'B2'. In this case, the orbit representing the branch is the 'O2' colored in purple. This second branch is formed by, again, doubly-symmetric orbits, but this time with the perpendicular crossings located in the interior part of the orbit, i.e. by IDS orbits. Another difference with the previous branch is that this one is bounded in both sides, and it has a smaller size and energy than the other. As for the linear stability, excepting the limiting bifurcating orbits that have, as mentioned, $s_1 = b_1 = 2$, the orbits are again unstable for the in-plane motion, and are stable for the out-of-plane motion in all the range of the branch. Nevertheless, this instability in-plane remains in more or less low for all the branch.

In Figures 5.5c and 5.5d, the 3rd branch, and the last with fully retrogrades orbits, is represented. This branch is bounded again, but this time only one of the limits is a bifurcating orbit, as the other one, named as 'C' and colored in light gray, is a collision orbit. The characteristic shape of this branch is EDS orbits, the same as with the first branch, this time exemplified by the light green colored 'O3' orbit. Compering the shape of the orbits of this branch with the ones of the first branch, it can be observed that in this branch the orbits are more rounded, as they have an aspect ratio close to 1. Regarding the stability indices, similarly to the second branch, it is stable for the out-of-plane motion and unstable for the in-plane one, but this time this instability grows up to a value of around $s_1 = 10$. Taking into account the hyperbolic nature of the s_i index, which is the reason why it is useful for the graphical representation of very unstable orbits, this means that the orbit 'C' is a couple of orders of magnitude more unstable than the orbits of the second branch.

Finally, in Figures 5.5e and 5.5f, the 4th branch of the P3QSO family is illustrated. The evolution of this branch is much more complex than that of the other three branches. Starting from the collision orbit, for the first part of the branch the orbits are shape-wise like the maroon colored 'O4' orbit. At this stage, the orbits have still three loops, as the rest of the family. However, not all of the loops are around the second primary. This leads to a change in the direction of the relative motion, changing from retrograde (that is how it starts from the initial conditions placed on each of the perpendicular crossings) to prograde or direct for the part of the orbit placed closer to the second primary. As the branch evolves and the orbits become bigger, the orbit 'O5', colored in dark green, becomes a limit one that separates the area where the orbits have three loops to another one, where two extra loops appear vertically in each orbit. These extra loops have consequent changes in the direction of the rotation, still keeping the central part prograde but with now four loops with retrograde motion. An example of this type of orbits is 'O6', represented in a light blue color. In this orbit some of the loops are overlapped.

Similarly to the first branch, this branch is unbounded, and when continued beyond the portion of the family shown here, it continues to grow in size and energy while approaching an asymptotic value in period, as also observed at the beginning of the family. While this growth takes place, the central loop becomes smaller and tends to the second primary. As for the in-plane stability, almost all of the branch is very unstable. Nevertheless, there is a part of

the branch, around the 'O4' orbit, that bounces back to stable and where the stability index reaches a pointed minimum, whose value is -2. Regarding the out-of-plane stability, starting from the collision orbit, the stability index oscillates inside the stable area, from an initial value of -2 for 'C', to then a value of 2 for 'O4' and then coming back to -2 before increasing again, but this time becoming unstable. After this, it bounces back again and has a small stable area, with a minimum of -2 placed around the orbit 'O6'. Finally, after that minimum the index grows again and becomes unstable, with a very high value of b_2 by the end.

High-energy Families

As seen before, except for the period-tripling bifurcation, the 2D families emerging from the in-plane bifurcations of the QSO family come in pairs. Half of these bifurcating orbits, one from each pair, is located in upper right part of Figure 5.3b, i.e., the side with a higher energy. Not only this, but the families that arise from these orbits are lower-bounded by that energy. In contrast, the other half, the remaining members of each bifurcation pair, are located in the lower left part of the figure and are upper-bounded in energy at the bifurcation point. Therefore, this energy-related distinction gives rise to a subdivision into high-energy and low-energy families, allowing for a consistent classification of each member of every pair. In addition, each family has been given a name regarding its multiplicity, along with a subindex used to differentiate them: odd numbers are assigned to high-energy families and even numbers to low-energy ones. In this section, the five high-energy families up to multiplicity 7 are studied. These families not only exhibit the highest energy among each pair, but they are also the largest in size and have the highest period, which is likewise lower-bounded by the value on the bifurcation.

The first family studied in this section is the $\mathrm{P4QSO}_1$, represented in Figure 5.6. In contrast with the QSO and the P3QSO families, the $\mathrm{P4QSO}_1$ family is comprised of single-symmetric orbits instead of doubly-symmetric ones. Therefore, the orbits of this family are not symmetric with respect to the y-axis. This implies a fundamental change compared to the previous families, namely that while these orbits still have two perpendicular crossings, they no longer have the same $|\xi_0|$. Moreover, both perpendicular crossings are placed on the same side of the orbit. This is the reason why in Figure 5.6a, for the left plot corresponding to the initial position, there are two different lines, one labeled exterior and the other one, interior. Contrary to what it may look like, these two lines do not correspond to two different branches, but represent each of the perpendicular crossings of each orbit, at which the initial condition can be placed equally. However, the family actually consists of two branches, each of them illustrated in Figures 5.6c and 5.6d, respectively. The reason behind having only one line in both Figures 5.6a and 5.6b (excluding the case of the initial position, already addressed) is that each branch mirrors the other with respect to the y-axis. Therefore, the energy, the stability, and the initial distance to the second primary of each branch are exactly the same. This is possible thanks to the symmetry that the H3BP model possesses with respect to this axis.

Each of the branches can be differentiated following the classification made in Section 5.1. In this sense, the branch with the perpendicular crossings in the negative x-axis is composed by LSS QSOs (Figure 5.6c), and the one in which the orthogonal crossings are located on the

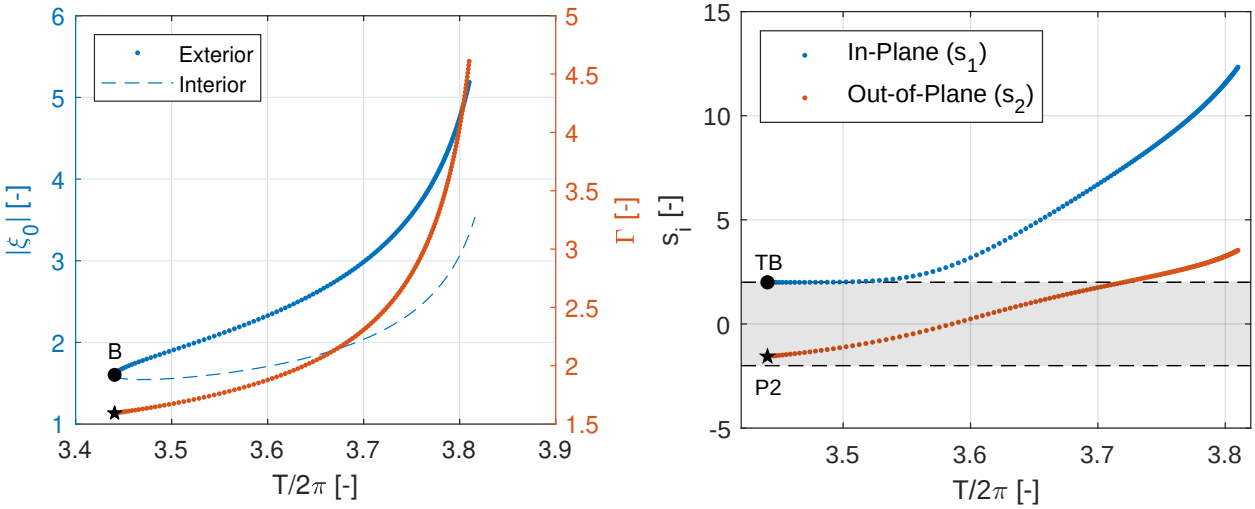

(a) Initial position and energy evolution

(b) Stability evolution

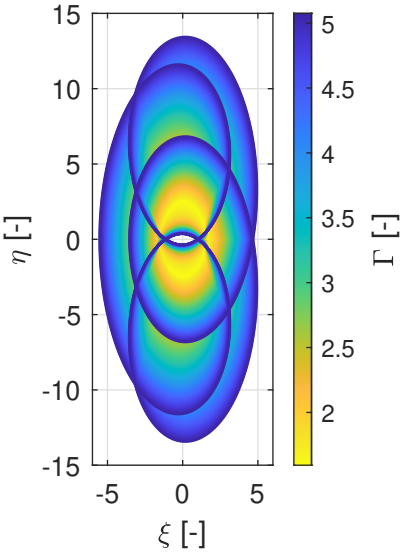

(c) LSS branch

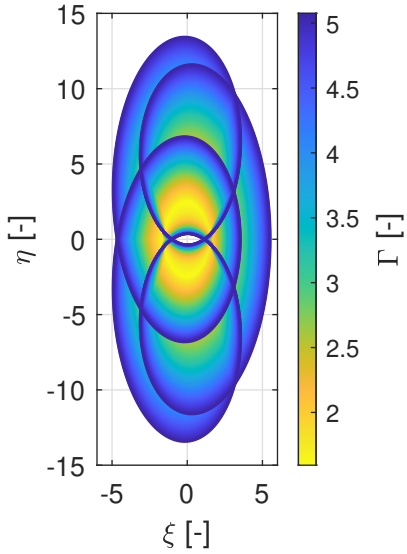

(d) RSS branch

Figure 5.6: High-energy P4QSO$_1$ family in the H3BP

positive part of the x-axis have RSS orbits (Figure 5.6c), respectively. Finally, the evolution of the different characteristics of the family is very simple. While the family evolves from the bifurcating orbit, the orbits become bigger, more energetic and more unstable for the in-plane motion. Regarding the out-of-plane stability, the orbits are stable for part of the family (the gray area showed in Figure 5.6b), but as the family grows, this motion also becomes unstable. As for the period, it also increases, but it seems to approach a maximum value asymptotically.

The next high-energy family is the P5QSO$_1$, represented in Figure 5.7. Like the P3QSO, this family is formed by double-symmetric orbits. The family is composed of two distinguished branches, as it can be observed in both (a) and (b). Additionally to the 'B' orbit, which indicates the bifurcating orbit from which the family is derived, two additional orbits are marked in these plots to exemplify the shape of each branch with the help of (c). The first

branch to be considered is the one of the yellow colored 'O1'. This branch is comprised by exterior orbits, i.e. orbits with the perpendicular crossings in the external part of the orbit, so they are EDS QSOs. The different orbits that form this branch are shown in (d), colored according to its energy parameter, Γ. The second branch, illustrated in (e), consists of IDS orbits. Both branches follow the evolution that characterize the high-energy families. Starting from 'B', they grow in size, energy and period, but approaching asymptotically a maximum in period. An important feature comparing the two branches is that for the same period, the branch with EDS orbits possesses a higher energy than the one with IDS QSOs. In addition, the EDS branch tends to a smaller value in period than the IDS one.

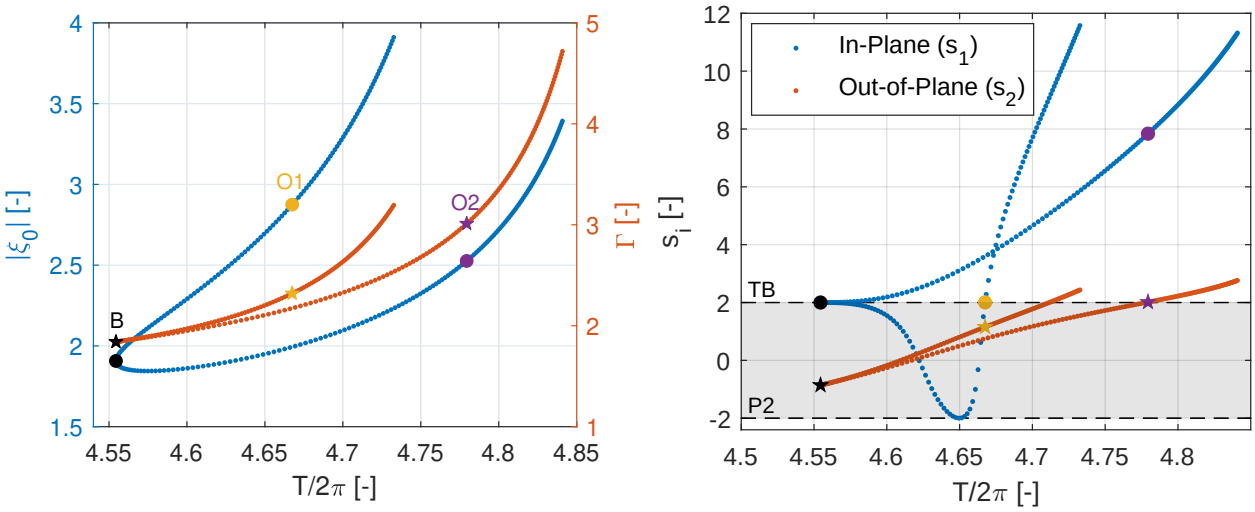

(a) Initial position and energy evolution

(b) Stability evolution

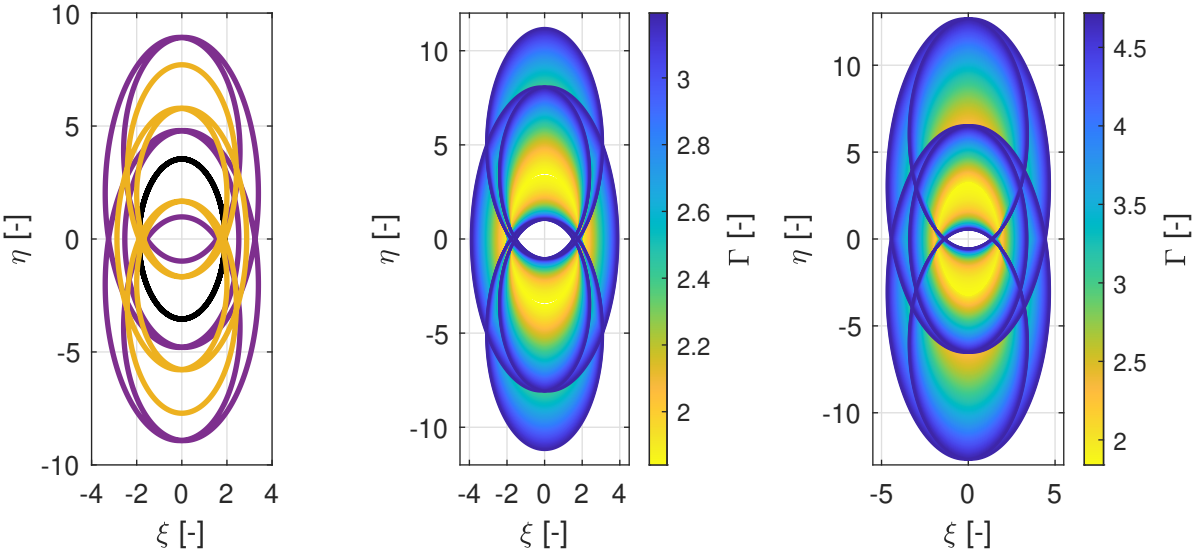

(c) Marked orbits

(d) EDS branch

(e) IDS branch

Figure 5.7: High-energy P5QSO$_1$ family in the H3BP

Finally, let study the stability of each branch separately. For the in-plane motion, the beginning of the EDS branch is stable. In this stable area, the stability index oscillates, starting in $s_1 = b_1 = 2$ for the bifurcating orbit, then decreasing until reaching a value of

$s_1 = b_1 = -2$ and finally growing back to 2 for the 'O1' yellowed orbit. All this evolution of the stability index inside the stable area corresponds to an evolution of the pair of eigenvalues around the unit circle. From the 'O1' orbit the branch becomes unstable, with a sharp increase of the hyperbolic stability index. The case of the IDS branch is simpler, as the stability index has a constant growth from the 'B' orbit, being therefore unstable for all the branch. While the growth of this branch is not as sharp as in unstable area of the EDS branch, it still reaches high values of instability among the studied range. Lastly, the out-of-plane stability of both branches is similar. They start composed of stable orbits, with the stability index rising at a constant gently rate. In both cases, the branch is stable for a large portion of it, but they become unstable eventually. A final important aspect of the family regarding stability is the fact that there is an in-plane tangent bifurcation in the EDS branch. Although, in general, the bifurcations that arise from the families of swing QSOs are not taken care of in this work, this in-plane tangent bifurcation is included under this investigation, as it will be important when transitioning these families to the CR3BP. Consequently, the family that arises from this bifurcation is studied next.

The family that bifurcates from the EDS branch of the P5QSO_1 is called $\text{P5QSO}_{1,T}$ in this work. This family is represented in Figure 5.8, where in (a) the P5QSO_1 is also illustrated to show part of the family tree. This new family is, similarly to P4QSO_1, composed of single-symmetric orbits, but this time each of the perpendicular crossings are located on opposite sides of the x-axis. Still, the same considerations as what happened with P4QSO_1 apply here. That is, the family possesses two branches that mirror each other, and two different initial conditions can be used equally for each orbit, depending whether the interior or exterior perpendicular crossing is selected. It is important to notice that the exterior in this case does not refer to whether the point the most exterior point of its side of the x-axis of the whole orbit, but it is just a comparison between both perpendicular crossings, with the one more distant from the second primary being designated as exterior and the other one as interior. In fact, both crossings are located in the external part of the orbit. If the exterior perpendicular crossing is considered, the branch with LSS orbits, (c), has the initial point in the negative part of the x-axis, and the one with RSS QSOs has it in the positive one.[2]

As for the evolution of the family, it follows the characteristics of any other high-energy family of this investigation, where it evolves from the bifurcating orbit, in this case 'B2', increasing in size, energy and period, this last asymptotically. Regarding the stability, for the out-of-plane index has an evolution similar to the one of each branch of the P5QSO_1 family. The in-plane case is a bit more complicated, with first a decrease of the hyperbolic stability index and, after reaching a minimum, an increase that ends similarly to the rest of the branches studied for high-energy families. Among this evolution, there are two different areas where the orbits are stable, however they are very restricted in period. The majority of the family is unstable, with a first area where the instability is not that high, but a second and final area where the stability index grows quite rapidly to very unstable values. Finally, as the beginning of both branches is stable for the in-plane index, the type of tangent bifurcation from which this family arises is a supercritical pitchfork.

[2]It would be the other way around if the internal crossings were selected. Moreover, selecting only the negative axis, the whole family can be obtained by changing from the external crossing for the LSS branch, to the internal point for the RSS one. It can also be reversed by selecting the positive x-axis.

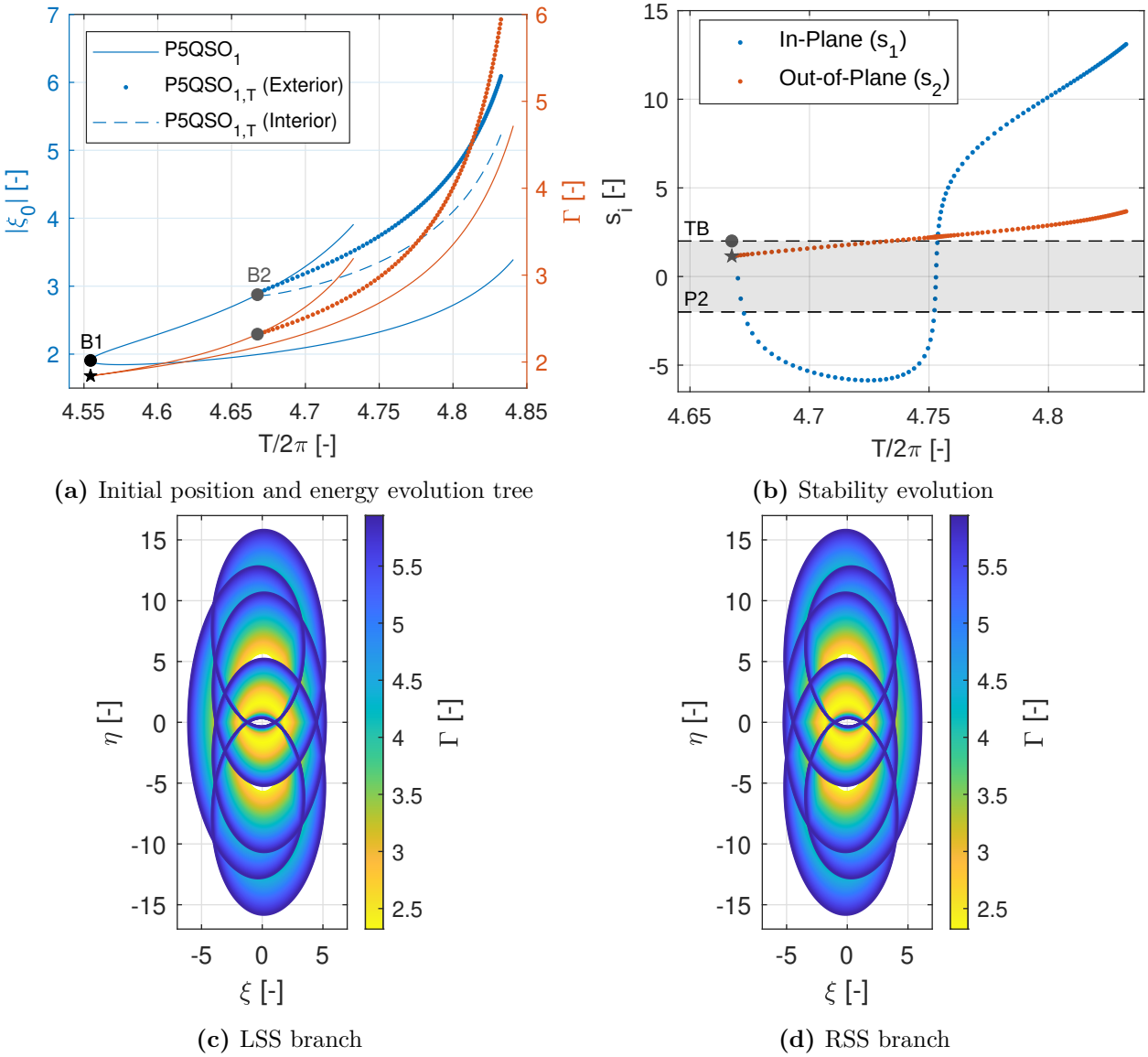

(a) Initial position and energy evolution tree

(b) Stability evolution

(c) LSS branch

(d) RSS branch

Figure 5.8: High-energy P5QSO$_{1,T}$ family in the H3BP

The following family studied is the P6QSO$_1$, presented in Figure 5.9. A comparison of this figure with Figure 5.6, illustrating the family P4QSO$_1$, clearly highlights the similarities. These two families have the same evolution and the same characteristics. Accordingly, everything said about the P4QSO$_1$ family applies to the P6QSO$_1$. Thus, the P4QSO$_1$ is a family of single-symmetric unstable orbits with two branches that mirror each other, one with LSS orbits and the other with RSS QSOs.

In Figure 5.10, the first of the two high-energy families with a multiplicity of 7, P7QSO$_1$, is shown. This family shares a lot of characteristics with the P5QSO$_1$ family. Like it, this family is composed of doubly-symmetric orbits with two different branches, one of EDS orbits, to which the 'O1' yellow colored orbit belongs, and another one with IDS ones, like 'O2' (represented by the purple color). However, there is a major difference regarding the role each

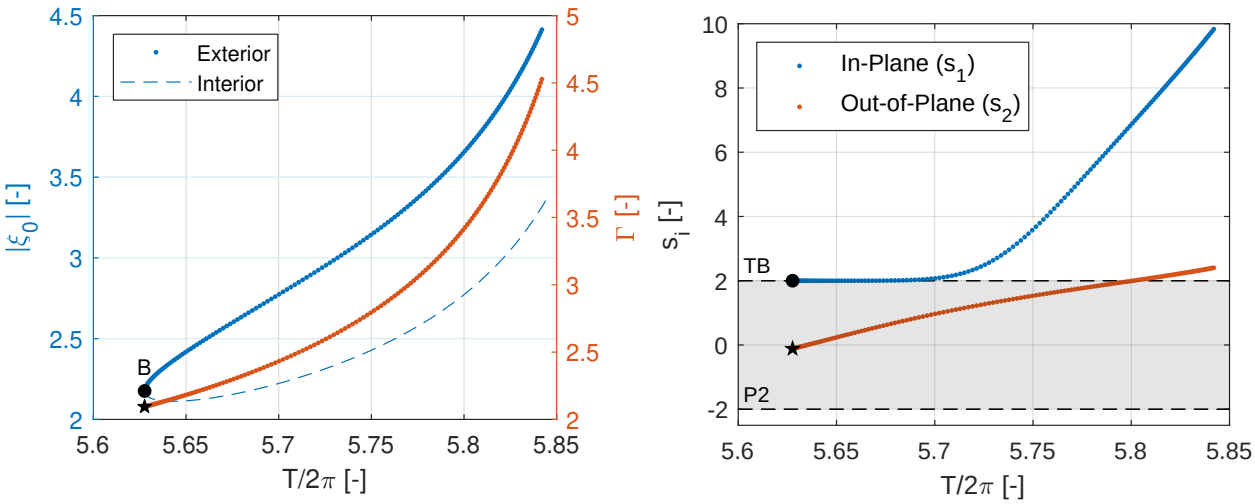

(a) Initial position and energy evolution

(b) Stability evolution

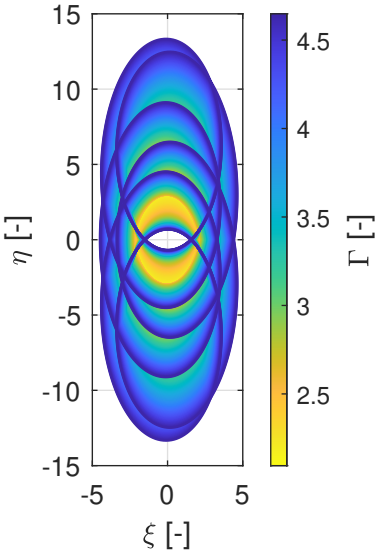

(c) LSS branch

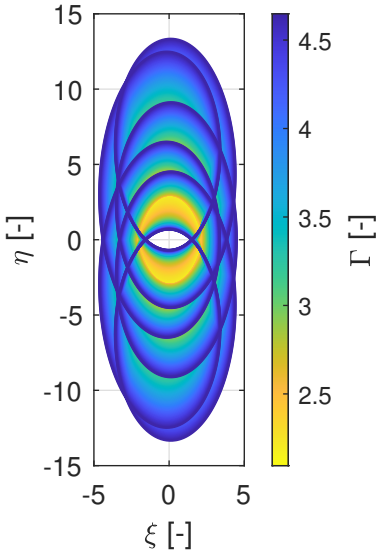

(d) RSS branch

Figure 5.9: High-energy P6QSO$_1$ family in the H3BP

branch has in the family. Concerning the energy and the stability of the branches, the roles of the EDS and IDS branches are reversed for this family with respect to the P5QSO$_1$ one. Hence, for this family the IDS branch possesses a higher energy and it is the one that has an in-plane tangent bifurcation, thanks to having stable orbits for part of the branch.

Following the expected trend, the P7QSO$_{1,T}$ family, depicted in Figure, consists of single-symmetric orbits with each of the perpendicular crossings located at opposite sides of the x-axis. The explanation of the figure is the same as the one of the P5QSO$_{1,T}$ family, with only one minor difference. As a consequence of this family bifurcating from the IDS branch, instead of the EDS branch, both perpendicular crossing points of the orbits of this family are interior points, in the sense of where they are placed with respect to the rest of the orbit. This should not be confused with the fact that one of the perpendicular crossings is called exterior

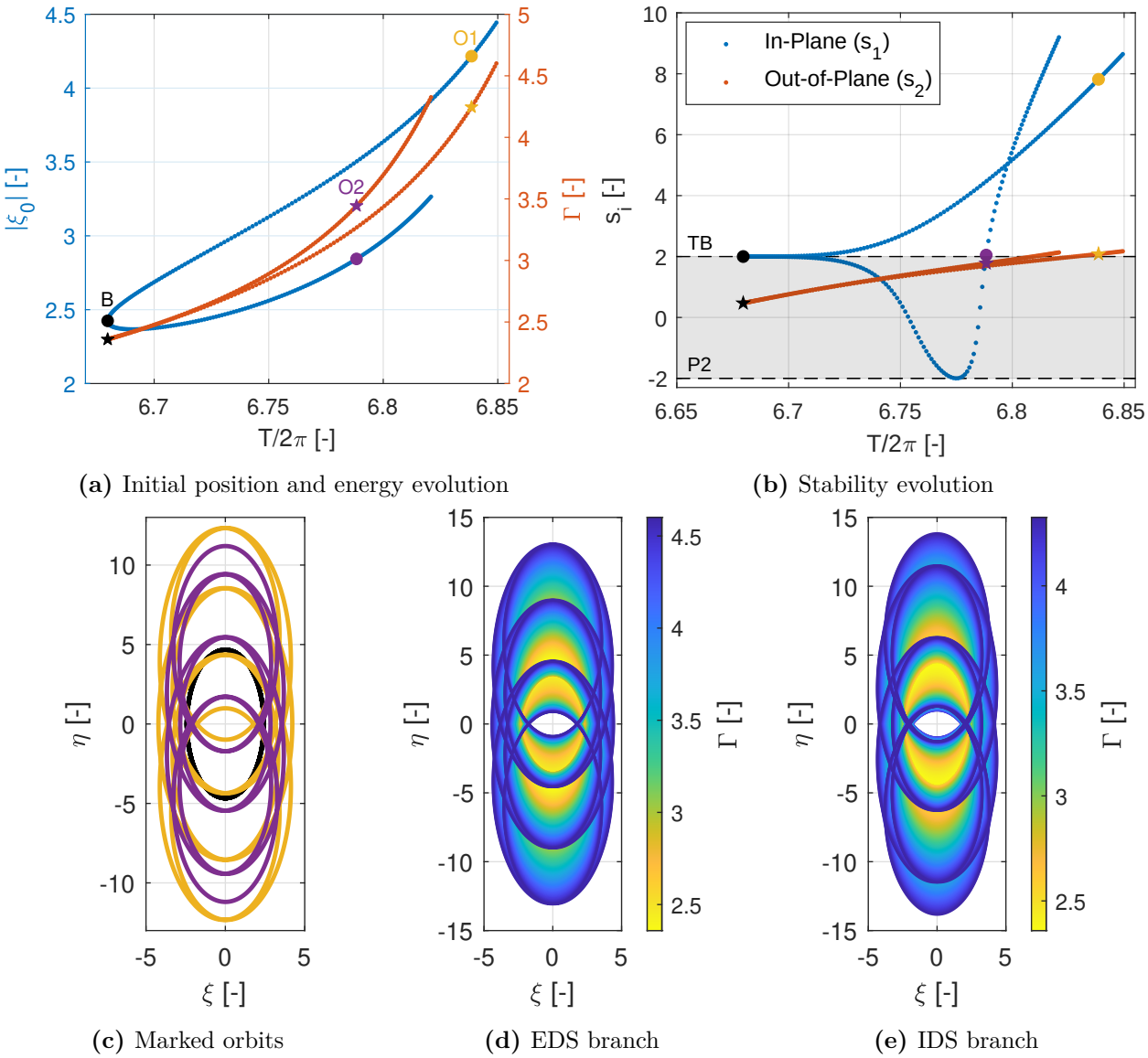

(a) Initial position and energy evolution

(b) Stability evolution

(c) Marked orbits

(d) EDS branch

(e) IDS branch

Figure 5.10: High-energy P7QSO$_1$ family in the H3BP

and the other one interior to differentiate them, with this classification depending only on the position of this two points. Another important thing to remark when comparing these two families is the fact that, even though they bifurcate from the opposite branch in terms of the shape, in both cases the bifurcation takes place at the branch with the higher energy.

The last high-energy family included in this work is the P7QSO$_3$ family, illustrated in Figure 5.12. Following the trend of the high-energy families bifurcating from the QSO, in which their symmetry alternate, this family is formed by single-symmetric orbits, as the P4QSO$_1$ and the P6QSO$_1$. In a similar way to what happened with these two families, and with the other single-symmetric families, it possesses two branches, one of LSS orbits and the other of RSS ones, composed of orbits that mirror each other with respect to the y-axis. However, this family has a couple of characteristics that contrast with those of these two

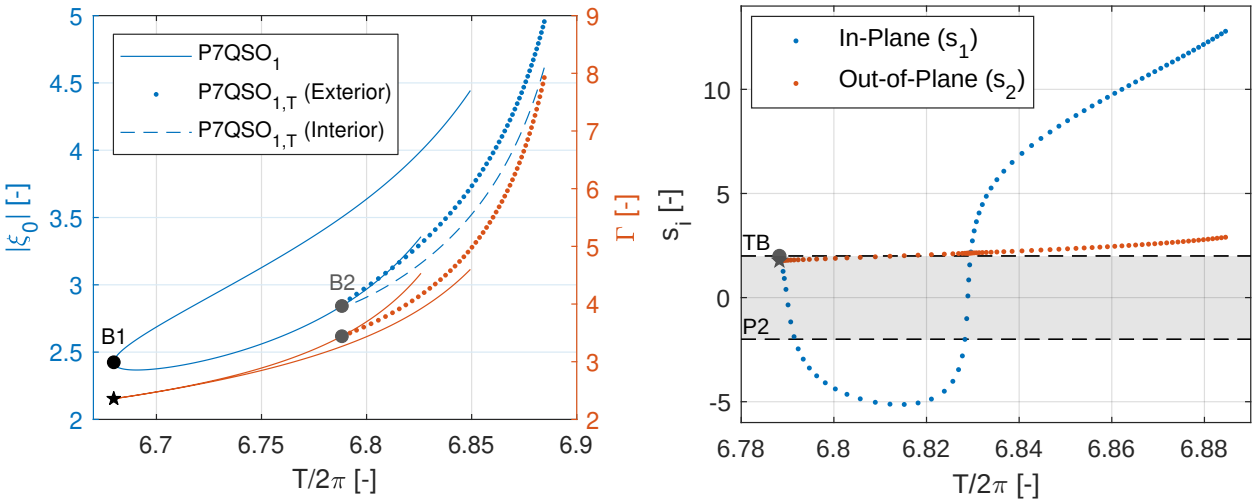

(a) Initial position and energy evolution tree

(b) Stability evolution

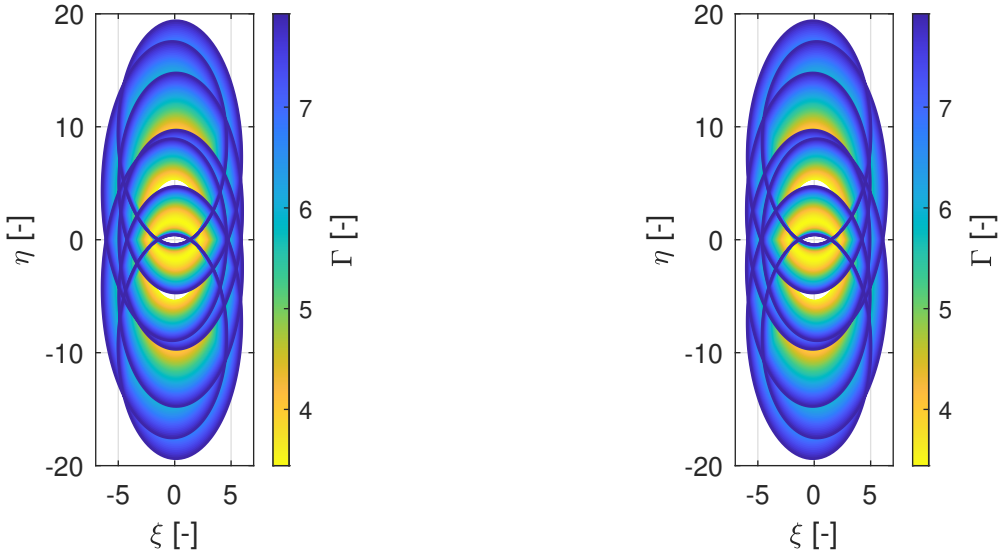

(c) LSS branch

(d) RSS branch

Figure 5.11: High-energy P7QSO$_{1,T}$ family in the H3BP

families. The first is related with the behavior of the out-of-plane stability index. Whereas for the P4QSO$_1$ and the P6QSO$_1$ this index was monotonically increasing, for the P7QSO$_3$ family it has a minimum at the line of the period-doubling bifurcation, before starts increasing indefinitely. After that, like it happened with the other two families the index eventually crosses the 'TB' line, which indicates a tangent bifurcation, becoming unstable. Nevertheless, the slope in this area is higher than those of the other two families.

The second characteristic that differs in this family is the position of the two perpendicular crossings, as these are located at opposite sides of the second primary. Looking at Figure 5.12c (the same applies to Figure 5.12d), it may seem like there are three perpendicular crossings. Sill, the crossing situated on the exterior part towards the negative x-axis is actually two different crossings that are not perpendicular to the axis. Therefore, the two perpendicular

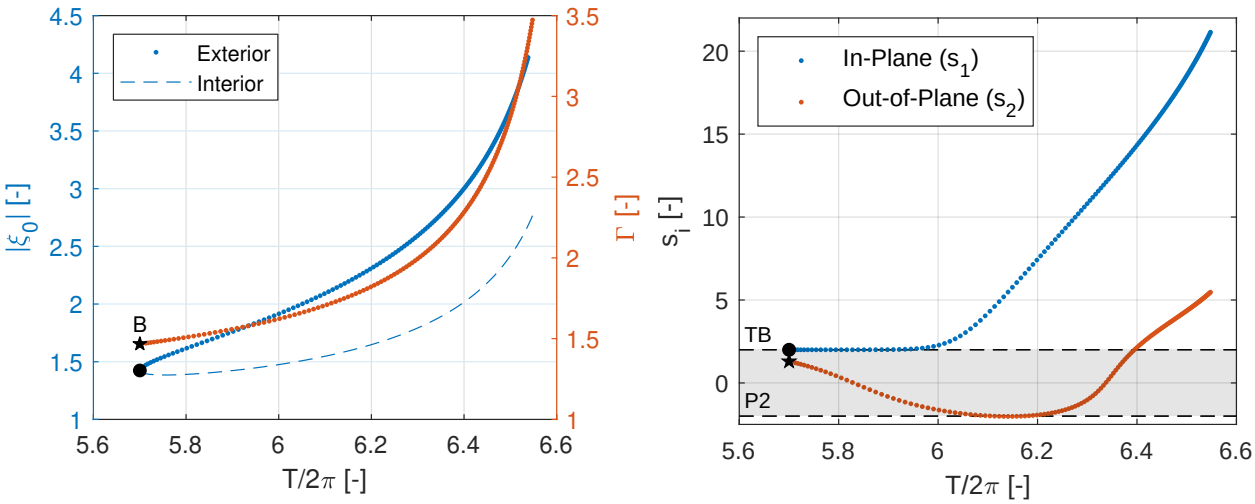

(a) Initial position and energy evolution

(b) Stability evolution

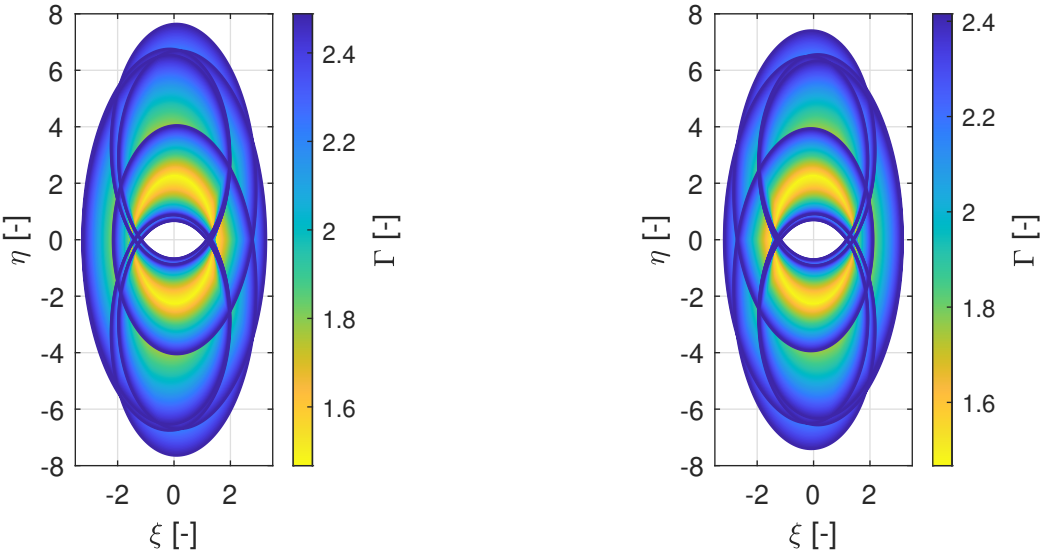

(c) LSS branch

(d) RSS branch

Figure 5.12: High-energy P7QSO$_3$ family in the H3BP

crossings correspond to the exterior crossing of the positive x-axis and the one located at the interior part of the orbit in the negative part of the axis. In fact, this also differs from the behavior of the P5QSO$_{1,T}$ and P7QSO$_{1,T}$ families. Recall that these two families were single-symmetric with the perpendicular crossings at opposite sides of the x-axis. Nevertheless, they had both of the crossings situated at the same area of the orbit, that is, or both were interior points or both were exterior ones.

The last final consideration that is important to address regarding the orbits of this family is a qualitative one, related to its concrete shape. While for the rest of the high-energy families up to this, they grow vertically as the multiplicity increases, in such a way that visually each family has more vertical loops than the precedent, this is not the case anymore with this family. Even though it actually possesses the same amount of loops as in the previous family,

due to the multiplicity, visually some of those loops are almost overlapped, giving a simpler appearance. In fact, taking a look at Figures 5.5a and 5.6c (or 5.6d), it can be observed a resemblance between those orbits and these ones, in such a way that it looks as if the orbits of the P7QSO$_3$ family where a combination of the orbits of the first branch of the P3QSO family and the orbits of the P4QSO$_1$ one.

Low-energy Families

In this section the other members of each pair of families will be studied. This sums up to 5 low-energy families. Contrasting high-energy families, the low-energy ones are characterized by a smaller size, a smaller period and, as its name implies, a smaller energy. As it could be expected, the energy is upper-bounded by the one of the bifurcating orbit, same as the period. Another important characteristic that will be analyzed is that these families possess collision orbits that provoke the existence of branches of the families where the motion is not fully retrograde, which reminds the behavior of part of the P3QSO family.

The first family studied in this section is again the one of multiplicity 4, that is, this time, the P4QSO$_2$. Figure 5.13 presents the plots needed to understand the behavior of this family. The family is composed of single-symmetric orbits, similarly to the P4QSO$_1$. Therefore, starting from the bifurcation orbit 'B', two different branches arise with exactly the same characteristics but the shape mirroring each other. Thus, there is a branch of LSS and another of RSS orbits. Nevertheless, the structure of this family is a bit more complicated than those of the high-energy single-symmetric families. As anticipated, the family possesses a collision orbit, labeled 'C', from which the orbits have a mixed motion. For this reason, in this work this family is divided into 4 different branches, but due to the symmetry of the branches, only two of them can be distinguished in Figures 5.13a and 5.13b, where 3 orbits are labeled. However, each of these branches and each of these orbits correspond actually to a pair of branches and orbits, the left version and the right one. The characteristic orbits of these branches are shown in Figures 5.13c, 5.13d, 5.13e and 5.13f.

The first two branches, (c) and (e), have 'O1' as an example of the characteristic shape, and have 'B' and the left and right 'C', respectively, as limiting orbits of the branches. These orbits are single-symmetric with both perpendicular crossings at the same side of the orbit. The shape of the orbits are similar to those of the P4QSO$_1$ family, but with an aspect ratio closer to 1. Each branch of the second pair, (d) and (f), is limited by the 'C' orbit and have 'O2' as an example of orbit. One side of these orbits (left on (d) and right on (d)) resembles the orbits of the last branch of the P3QSO family (maroon orbit of Figure 5.5e), with two horizontal loops, an exterior loop where the motion starts as retrograde and then a central loop with a prograde motion. The other side is composed of two vertical loops that are symmetric with respect to the x-axis. The continuation of these mixed branches is achieved until the interior perpendicular crossing tends to the second primary. This collision seems to indicate the end of the family, as it could not be continued beyond, but a regularization strategy should be implemented to make sure of it, which is out of the scope of this investigation.

Another important characteristic of the family, which was also anticipated, is that the energy decreases from its initial value at the bifurcating orbit. Moreover, the Γ function decreases monotonically, so the mixed orbits have a lower energy than the fully retrograde

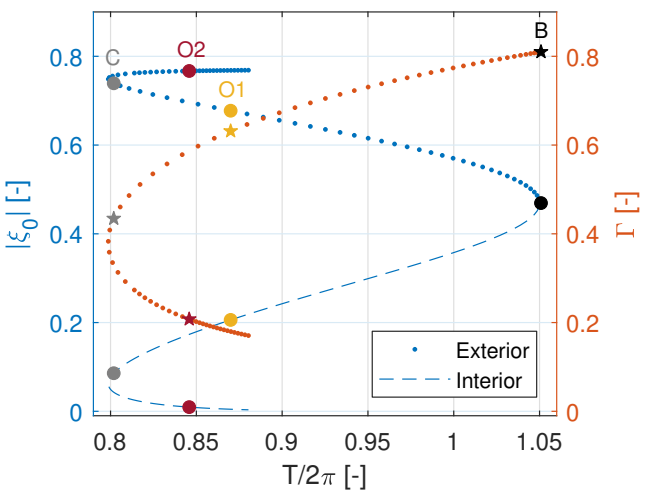

(a) Initial position and energy evolution

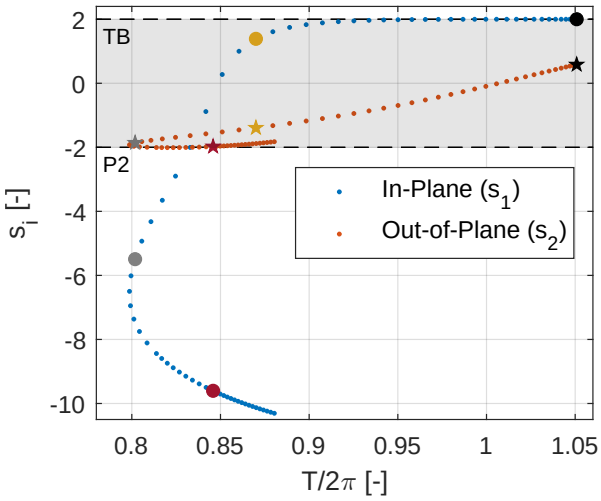

(b) Stability evolution

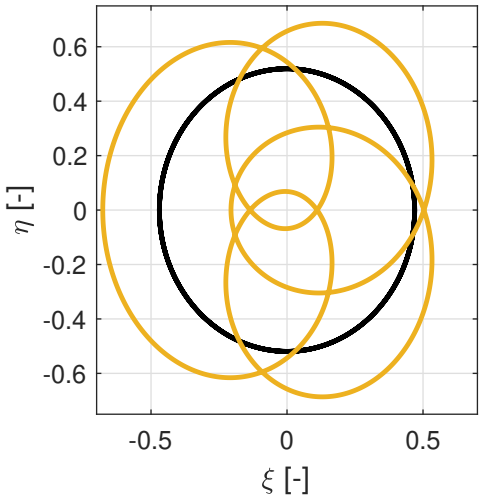

(c) Marked orbits of the LSS branch

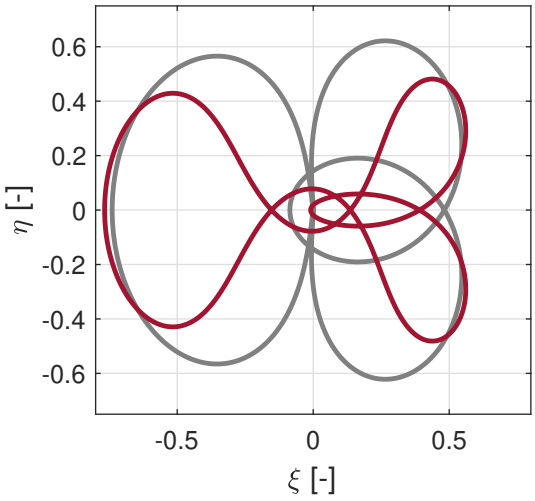

(d) Marked orbits of the mixed LSS branch

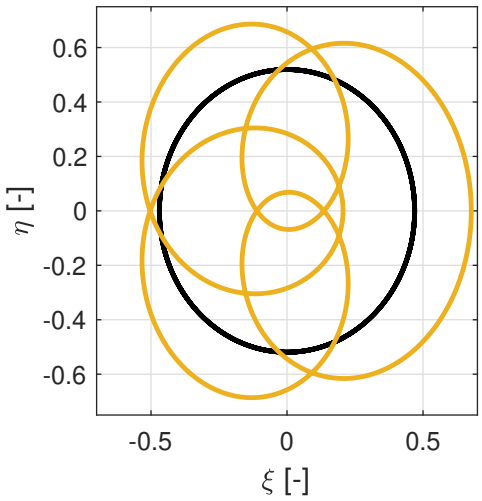

(e) Marked orbits of RSS branch

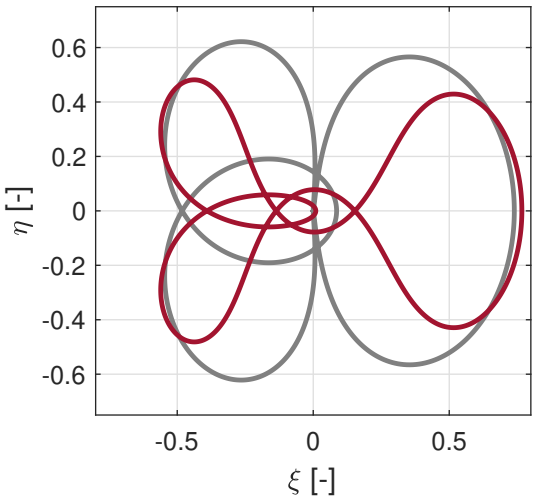

(f) Marked orbits of the mixed RSS branch

Figure 5.13: Low-energy P4QSO$_2$ family in the H3BP

ones. The final characteristic to be examined is the stability of the family. A great part of the fully retrograde branches is composed of stable orbits, grey shaded area, but towards the end of these branches the in-plane stability index decreases below $s_1 = b_1 = -2$ and the orbits become unstable. As the family evolves, the orbits get more unstable for the in-plane motion, reaching a great level of instability for the mixed orbits. As for the out-of-plane motion, all of the orbits are stable and the stability index possesses a minimum at around the period-doubling bifurcation, with two crossings to the 'P2'.

The next family studied is the P5QSO$_2$, depicted in Figures 5.14 and 5.15. Following the same pattern as with high-energy families, this family is formed by doubly-symmetric QSOs. The structure of the family is even more complicated than that of the P4QSO$_2$, so let analyze it first through Figure 5.14. Starting from 'B', two lines arise, both of them with an energy that monotonically decreases from 'B'. As for the initial distance, for one of the lines it monotonically increases, while for the other it decreases. The behavior of the period is a bit more complicated. In both parts of the family, it initially decreases from the one at 'B', but afterwards there is an inflection point and it starts increasing. Each of the two parts of the family is composed of two branches, so let study first the branches that come from 'B'. From these two branches, the upper one, exemplified by the orbit 'O1', is composed of EDS QSOs. The lower branch, conversely, is formed by IDS orbits like 'O2'. Both branches are limited by a collision orbit labeled as 'C1' and 'C2', respectively. These two branches can be further analyzed through Figures 5.15a and 5.15b. Following the typical characteristics of the low-energy families, the aspect ratio of both the EDS and IDS branches is close to 1. Regarding the in-plane stability, these two branches have an opposite behavior. While for the EDS one the index increases from 'B', so the branch is unstable, for the IDS branch the index decreases and remains within the stable area for all the branch. As for the out-of-plane stability index, the evolution for both branches is pretty similar, being both stables.

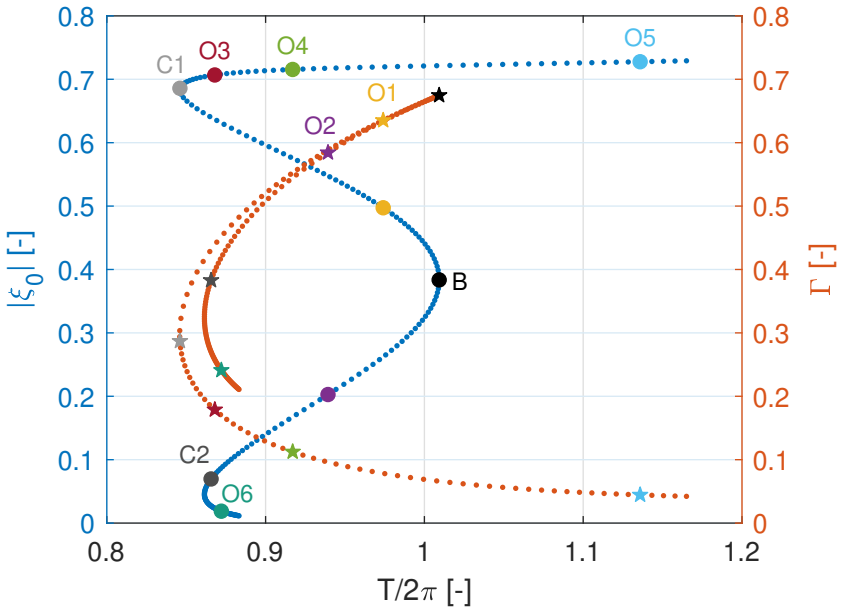

Figure 5.14: Initial position and energy evolution of the low-energy P5QSO$_2$ family in the H3BP

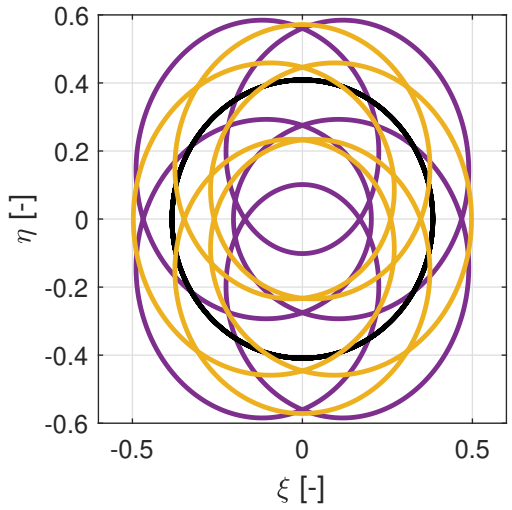

(a) Marked orbits of the EDS and IDS branches

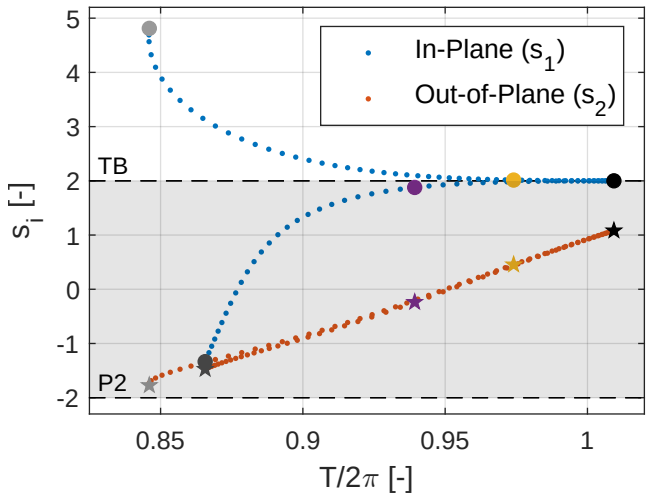

(b) Stability evolution of the EDS and IDS branches

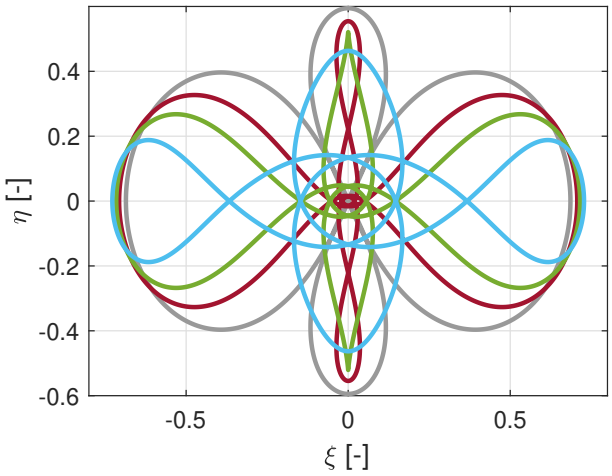

(c) Marked orbits of the mixed EDS branch

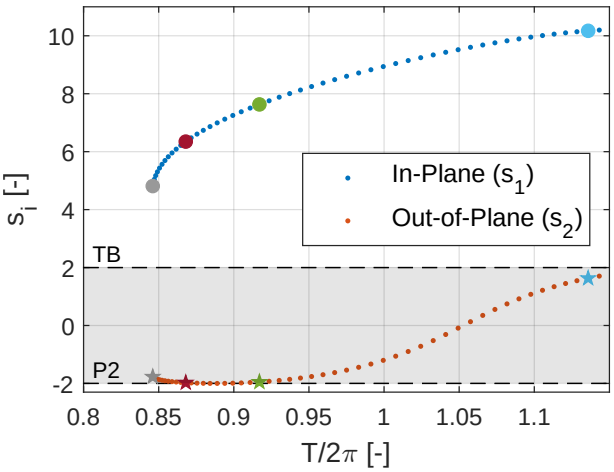

(d) Stability evolution of the mixed EDS branch

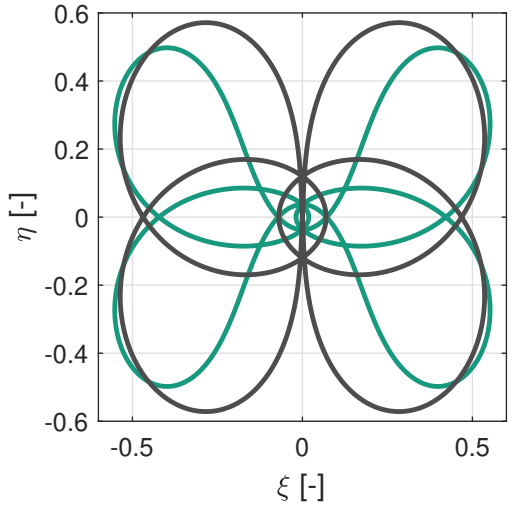

(e) Marked orbits of the mixed IDS branch

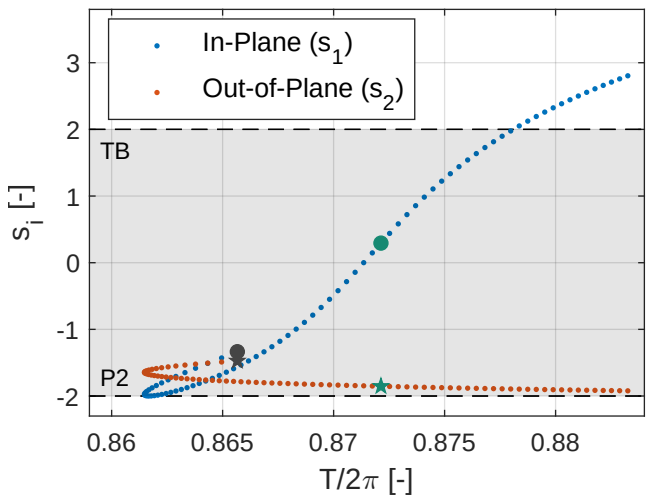

(f) Stability evolution of the mixed IDS branch

Figure 5.15: Low-energy P5QSO$_2$ family in the H3BP

Two more branches arise after the collision orbits, one after each. Let study first the one that starts after 'C1', i.e. as a continuation of the branch of EDS QSOs, and in which three different orbits are labeled, 'O3', 'O4' and 'O5', due to the complexity of the branch. Not only is the symmetry of the family maintained for this mixed branch, but also the orbits still have the two perpendicular crossings on the outer part of the orbit. Therefore, these orbits can be classified as EDS too. As said, the evolution of their shape is complex, so let define it with the help of the marked orbits. The light green 'O4' orbit is a limit one that separates a first area of the branch where the orbits resemble the maroon 'O3' and the last part where they look like the light blue colored 'O5'. The orbits that belong to the first part of the branch are formed by three horizontal loops placed around the x-axis and four vertical ones, around the y-axis. The behavior through them is complex, with several changes in the direction of the motion, from retrograde on the exterior parts to prograde on the inside. After the 'O4' orbit, two of this vertical loops disappear and the orbits become similar to the 'O5' marked orbit.

As for the linear stability of the EDS mixed branch (Figure 5.15d), the orbits are very unstable for the in-plane motion and stable for the out-of-plane motion. Another characteristic of the branch is that it does not seem to be bounded. Looking at Figure 5.14, it can be observed how, as the branch is continued, the period is increased with no apparent limitation, unlike what happened with high-energy families.However, for this branch what seems to be bounded is the initial distance and the energy, both with asymptotical behaviors.

The last branch is the mixed one after the 'C2' collision. Like the other mixed branch, the orbits of this branch keep the symmetry of the collision orbit and the orbits before it, so they are IDS orbits, as illustrated in Figure 5.15e with the dark green 'O6' orbit. As for the concrete shape of the orbits of this branch, curiously, each side of the orbits resemble one of the sides of the mixed branch of the $P4QSO_2$ family. More specifically, they look like the right side of Figure 5.6d. Unlike the EDS mixed branch, which could seemingly continue indefinitely, the continuation of this branch ceased once the perpendicular crossings became too close to the second primary. As for the stability, the most part of the branch is stable for both stability indices. Only by the end of the branch the orbits get unstable for the in-plane motion. During the evolution of the branch, the stability index has a minimum at the dashed 'P2' line and crosses the 'TB' one. Both cases indicate the existence of bifurcations, but the computation of the new families that may arise is out of the scope of this investigation.

The next family studied is the $P6QSO_2$, illustrated in Figure 5.16. Following the same trend seen with the high-energy families, this family shares many similarities with the $P4QSO_2$. The family is built out of single-symmetric orbits and has 4 different branches that come in pairs that are completely mirrored. Following the LSS part of the family, the first branch, (c), is limited by the 'B' and 'C1' orbits and is composed of orbits with both perpendicular crossings at the same side, one interior and the other exterior to the orbit. The second branch,(d) starts after the collision orbit 'C1' and is comprised of LSS mixed orbits. In this branch there is a second collision orbit, labeled as 'C2'. The other orbit marked for this branch is the 'O2' maroon one that represents the shape of the orbits after the second collision. The shape resembles that of the mixed branch of the $P4QSO_2$ with additional loops, corresponding to the higher multiplicity. Similarly to what happened with that branch, this cannot be continued further, as the interior perpendicular crossing moves too close to the second primary.

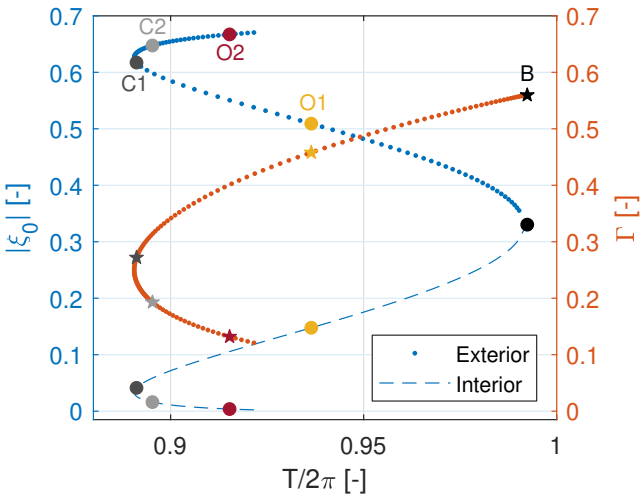

(a) Initial position and energy evolution

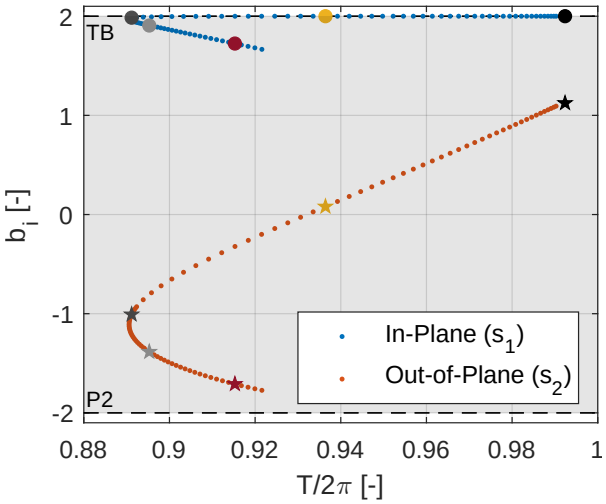

(b) Stability evolution

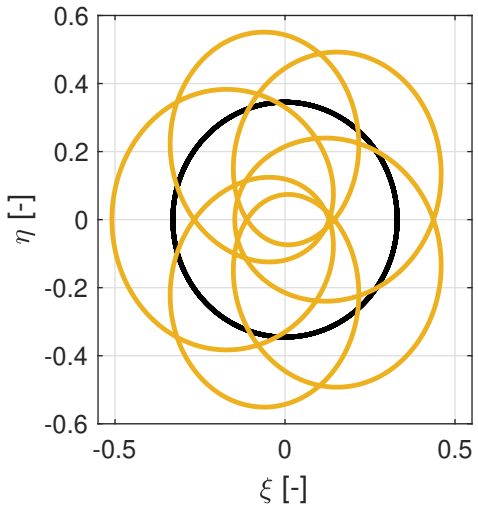

(c) Marked orbits of the LSS branch

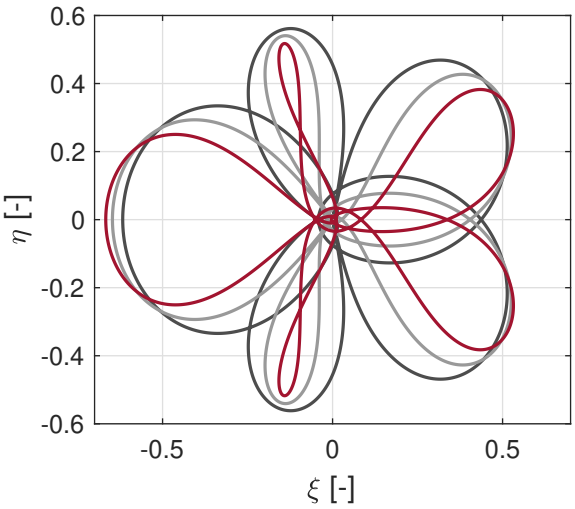

(d) Marked orbits of the mixed LSS branch

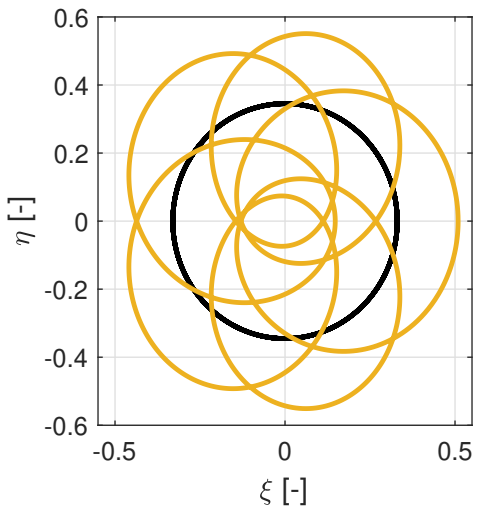

(e) Marked orbits of the RSS branch

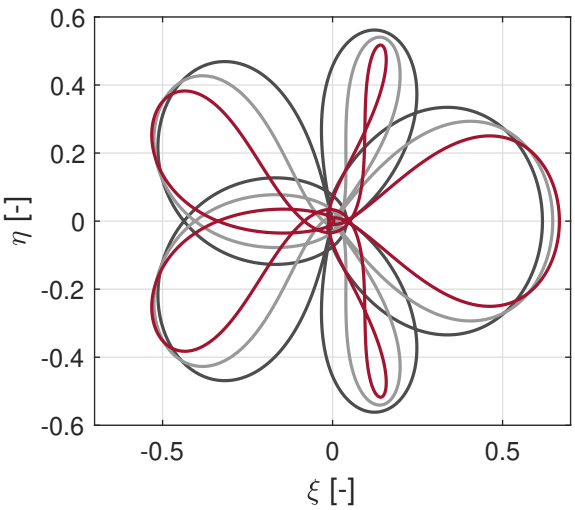

(f) Marked orbits of the mixed RSS branch

Figure 5.16: Low-energy P6QSO$_2$ family in the H3BP

The same considerations apply to the RSS branches, (e) and (f). Regarding the evolution of the characteristics of the whole family, the energy decreases monotonically from 'B' and all the orbits of the family are stable. It is important to note that in Figure 5.16, where the stability is depicted, the normal stability indices, b_i, are plotted, instead of the hyperbolic ones, s_i, used for the rest of families of swing QSOs.

The next low-energy family examined is the P7QSO$_2$ shown in Figures 5.17 and 5.18. Like with the P5QSO$_2$, this family consists of 4 branches of doubly-symmetric orbits: one composed of EDS retrograde QSOs, characterized by 'O1'; one with IDS retrograde orbits, like 'O2'; one formed by EDS mixed orbits, such as 'O3' and 'O4'; and finally the branch with IDS mixed orbits, illustrated by 'O5'. Due to the similarities of this family and the mentioned P5QSO$_2$ family, only the aspects that differentiate them are described here. The two retrograde branches' behavior is kept the same, with the only small difference being that the in-plane stability index stays very close to the 'TB' line. Consequently, the EDS retrograde orbits are unstable, as expected, but the instability is very small. When making a comparison with the P5QSO$_2$ family, it is important to notice that in Figure 5.15, the hyperbolic stability index is used, while in Figure 5.18 it is the normal one. As a result, the differences in instability are even higher than they may initially appear.

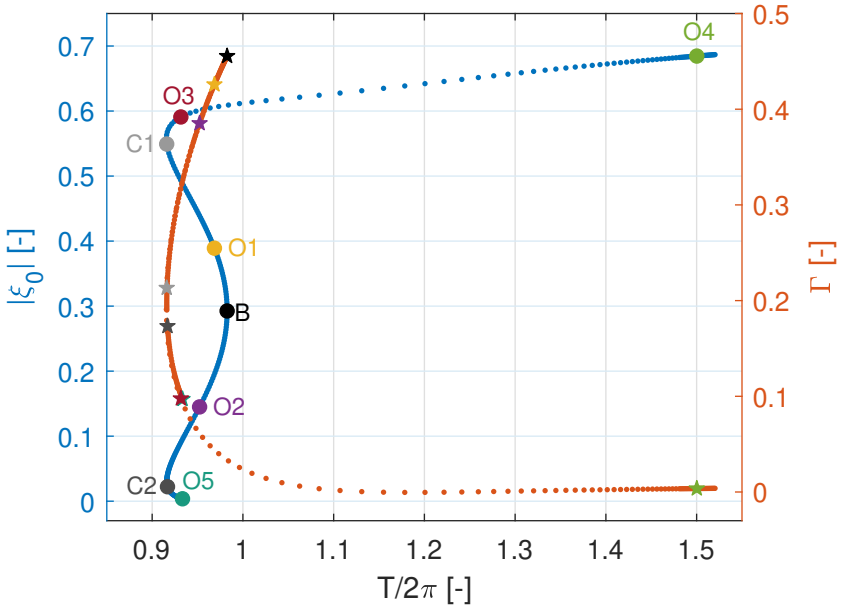

Figure 5.17: Initial position and energy evolution of the low-energy P7QSO$_2$ family in the H3BP

The behavior of the mixed branches varies more, so let study them separately. For the IDS mixed branch, there are two main differences with respect to the P5QSO$_2$ family. The first one lies in the stability too. Both the out-of-plane and the in-plane indices have an oscillatory behavior, with all the branch being stable for the out-of-plane motion. As for the in-plane, at the beginning of the branch the orbits are unstable, then there is a stable part and finally it goes back to unstable. Even though the instability remains controlled for the part of the family that is shown, the branch has no apparent limit and the slope of the index, with respect to the period, is steep towards the end of the branch, so it could become highly

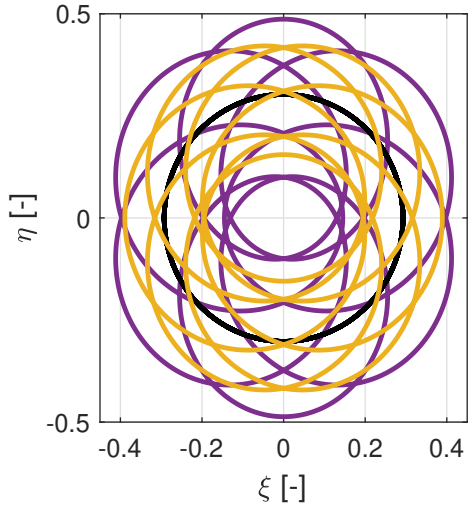

(a) Marked orbits of the EDS and IDS branches

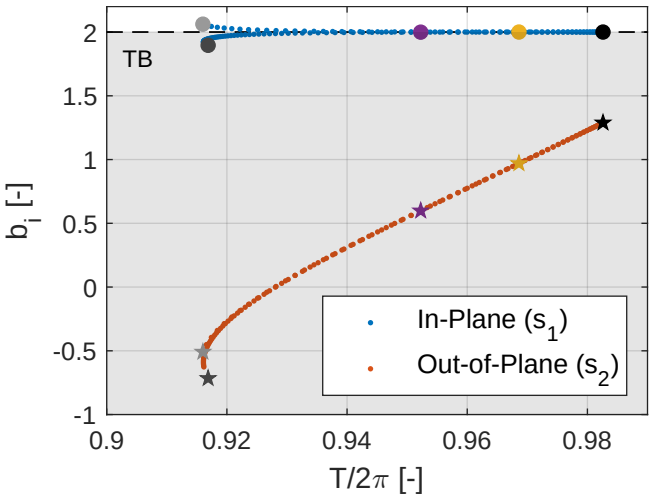

(b) Stability evolution of the EDS and IDS branches

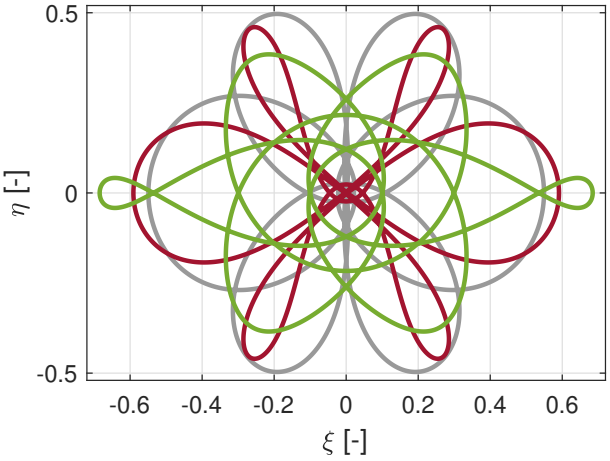

(c) Marked orbits of the mixed EDS branch

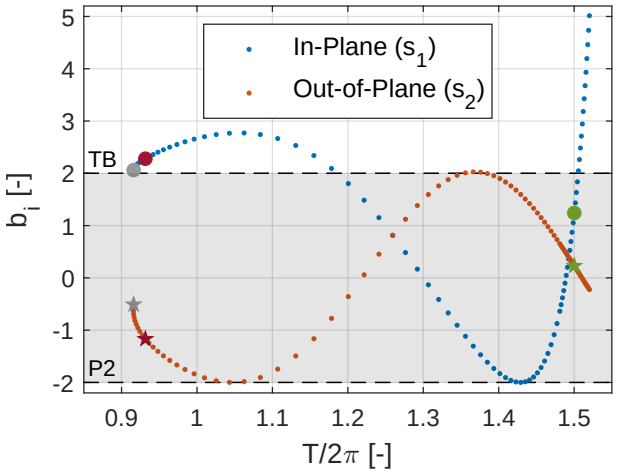

(d) Stability evolution of the mixed EDS branch

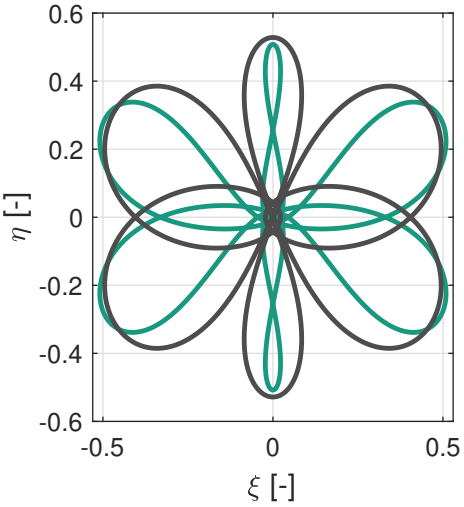

(e) Marked orbits of the mixed IDS branch

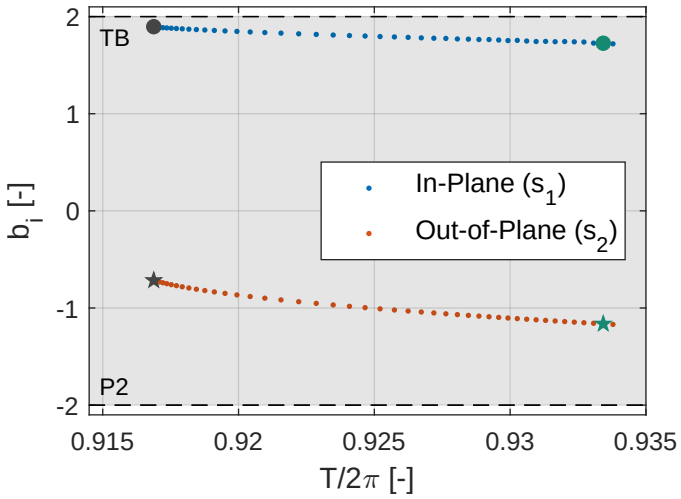

(f) Stability evolution of the mixed IDS branch

Figure 5.18: Low-energy P7QSO$_2$ family in the H3BP

unstable. All the families that may arise through the bifurcations found in this branch are out of the scope of this work. The second difference comes from the fact that for this family the period seems to be limited, while for the portion of the P5QSO$_2$ studied, no asymptotical behavior of the period was found. Regarding the shape, of the branch it is complex as well as its evolution, with some similarity with the shape of the corresponding P5QSO$_2$ family, but not enough to make a comparison. For the final branch, the EDS mixed one, the stability indices also differ from those to the family of multiplicity 5, as in this case all the branch is stable for both the in-plane and the out-of-plane motions. As for the shape of the orbits, they resemble that of the P6QSO$_2$ family, but with the expected differences that the different amount of loops and the different symmetry give them.

The final low-energy family included in this work is the P7QSO$_4$, illustrated in Figure 5.19. Following the same characteristics as the P4QSO$_2$ and the P6QSO$_2$ families, this family is composed of single-symmetric orbits structured in two pairs of branches that are a reflection from one another. One pair formed by retrograde QSOs and the other consisting of mixed orbits. The stability of this family has the same structure as that of the P4QSO$_2$ family. However, the evolution of the out-of-plane index differs, but with no consequences to the stability of the orbit as the eigenvalues remain inside the unit circle. Another difference is that for this family higher values of instability are reached.

Now, the focus is placed on each pair of branches separately to study the shape of their orbits. For the first pair of branches, the orbit marked in the figure is the yellow-colored 'O1'. Similarly to what happened with the orbits of the P7QSO$_3$, this orbit resembles those of Figures 5.5c and 5.13c (or 5.13e). So, in terms of shape, this branch of the P7QSO$_4$ family, resembles a composition of the third branch of the P3QSO family (composed of EDS QSOs) and the first branch of the P4QSO$_2$ family (formed by single-symmetric orbits). Another curious fact is that the LSS branch of this family resembles the RSS branch of the P4QSO$_2$ family, and vice-versa. For the second pair of branches, something similar happens but with a more complex behavior. This branch starts at the 'C1' collision orbit, but it possesses a second collision orbit labeled as 'C2'. The existence of two collision orbits is a characteristic that no branch of the P3QSO and the P4QSO$_2$ families have, but is consistent with the complexity introduced by having a multiplicity of 7. Accordingly, by examining the 'O2' maroon orbit of Figures 5.19d and 5.19f, a resemblance can be observed with the orbits seen in the mixed branch of the P3QSO family (Figure 5.5e) and the pair of mixed branches of the P4QSO$_2$ family (Figures 5.13d and 5.13f). More specifically, it resembles the maroon-colored orbit in Figure 5.5e. Similarly to the retrograde branch, the left-right behavior is reversed compared to that of the P4QSO$_2$ family.

5.3.2 Asymmetric Swing QSOs

As it has been advanced, as well as families of symmetric orbits, some families of asymmetric orbits also arise from the bifurcations founded in the steady QSO family. Nevertheless, not all the bifurcations lead to an asymmetric family, as only bifurcations that led to single-symmetric families give rise to asymmetric ones too. This difference between the amount of symmetric and asymmetric families could seem random, but it comes actually from the way the symmetric categories are defined. While symmetric orbits contain both the orbits that are only symmetric

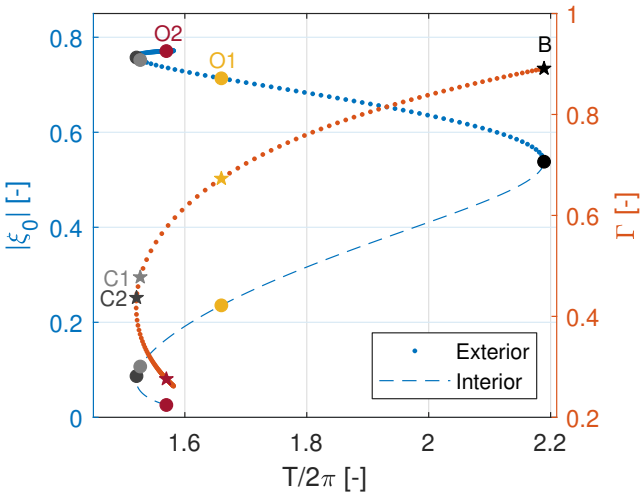

(a) Initial position and energy evolution

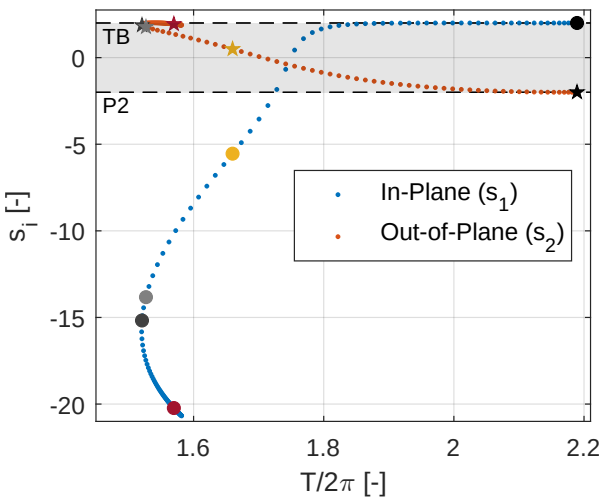

(b) Stability evolution

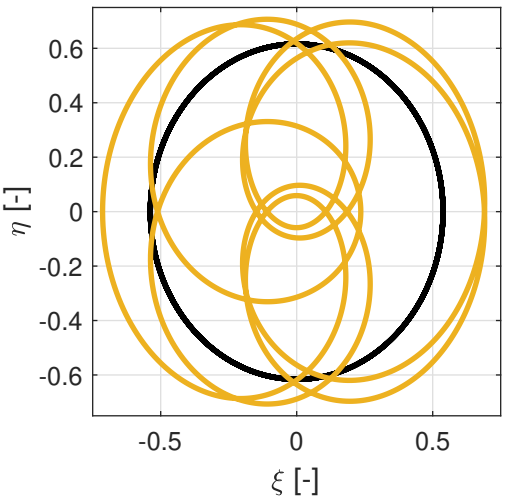

(c) Marked orbits of the LSS branch

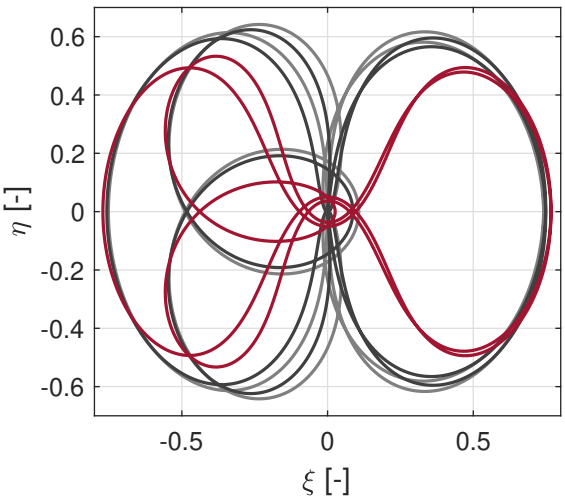

(d) Marked orbits of the mixed LSS branch

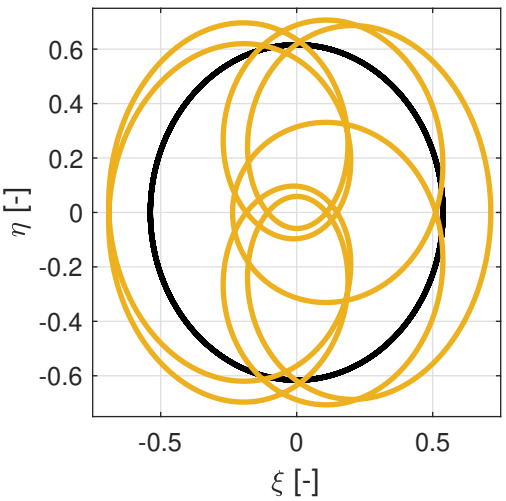

(e) Marked orbits of the RSS branch

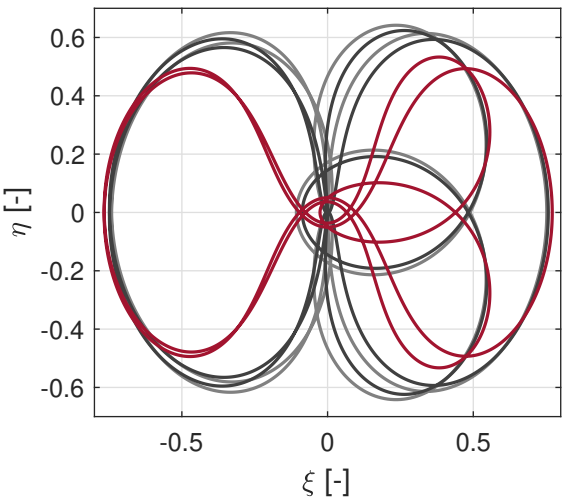

(f) Marked orbits of the mixed RSS branch

Figure 5.19: Low-energy P7QSO$_4$ family in the H3BP

with respect to the x-axis, single-symmetric, and the orbits that are symmetric to not only the x-axis but also the y-axis, doubly-symmetric, the asymmetric orbits contain only the orbits that are symmetric exclusively to the y-axis. If only the symmetry with respect to the y-axis were considered and a y-symmetric category of orbits were defined, there would be families of orbits arising from all the 12 in-plane bifurcation orbits. More concretely, there would be 11 families that would include the 5 doubly-symmetric families, presented in Section 5.3.1, and the 6 families of asymmetric orbits that are going to be presented in this section.

The six asymmetric families studied in this subsection are shown in Figure 5.20 together with the QSO family. For the QSO family, the initial conditions are changed with respect to the figures shown before. That is cause in here the initial condition is located in one of the two perpendicular crossings with respect to the y-axis. This is also where the initial conditions are placed for the orbits of the asymmetric swing QSOs families. For the continuation of these families, a perpendicular crossing algorithm is used, but this time with respect to the y-axis. For the QSO family a sigle-shooting algorithm is implemented and for the swing ones a multiple-shooter is applied. The dashed lines represent the interior perpendicular crossing on the y-axis, while the dot ones represent the exterior ones, in the same way that it did for the single-symmetric families. In fact, an asymmetric orbit is also by definition a single-symmetric orbit, just that with respect to the y-axis instead of the x-axis.

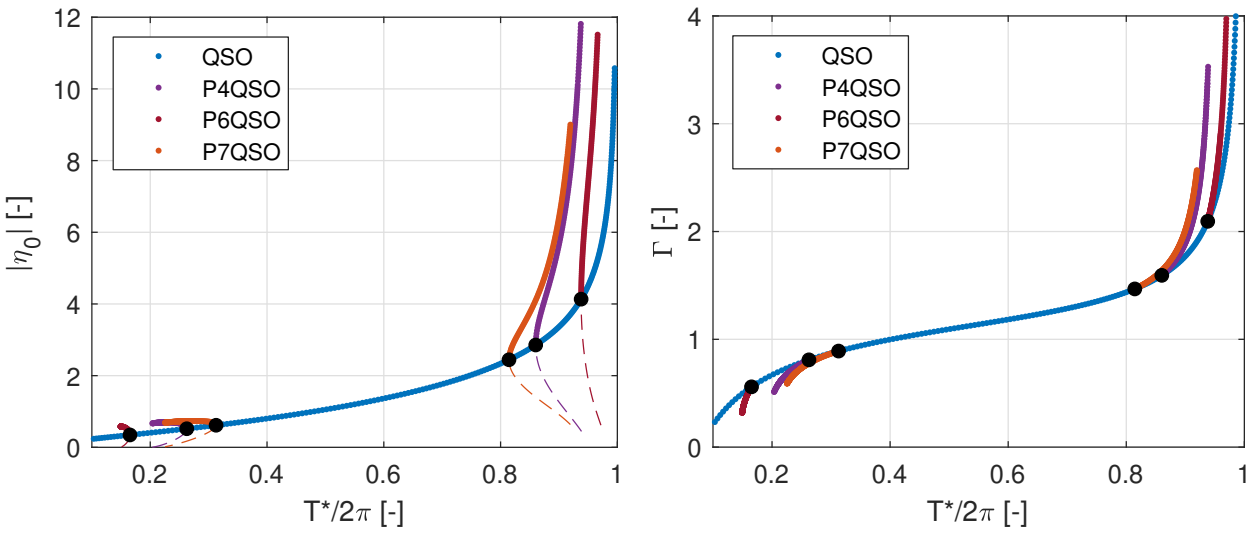

(a) Initial position evolution

(b) Energy evolution

Figure 5.20: Asymmetric swing and steady QSO families tree in the H3BP

Finally, the classification of these families has a similar pattern to what happened with the symmetric ones. Half of the families can be classified as high-energy families and the other half as low-energy ones. Each pair of families, regarding their multiplicity, is composed of one high-energy and one low-energy family. All these asymmetric swing families are studied in the following two separated subsections, corresponding to this energetic classification.

High-energy Families

In this section, the three high-energy asymmetric families shown in the upper-right side of Figure 5.20 are studied more in-depth. As with the symmetric high-energy families, the energy, period and size of the orbits increase from the bifurcating orbit. As for the name of the families, the same rule as for symmetric orbits will be used, where odd numbers are assigned to the high-energy families and even ones are for the families with low-energy.

The first high-energy asymmetric family is the $P4QSO_3$ depicted in Figure 5.21. This family has similar characteristics to the high-energy single-symmetric families. The family is composed of orbits that are symmetric to only one axis, in this case the y-axis, and that possess two perpendicular crossings along the y-axis, both placed at the same side of the orbits. It has two branches, one where the orbits extend more towards the upper-part of the plot, called 'up', and the other where they extend more to the low-part, referred to as 'down'. These two branches have exactly the same characteristics since the orbits of one branch are a perfect mirror with respect to the x-axis of the orbits of the other branch.

Regarding the initial position of Figure 5.21a, the branch composed of 'up' orbits, i.e. UA orbits, is obtained with the positive values of η_0, while the branch of down-asymmetric or DA orbits is obtained with negative values of the coordinate. As for the two lines observed, the dotted one corresponds to the exterior perpendicular crossings and the dashed line to the interior one. Like it was defined for the single-symmetric orbits, the exterior and interior perpendicular crossings depend just on the relative position to one another. However, for this family the exterior perpendicular crossing is the most exterior crossing of the y-axis and the interior perpendicular crossing is the most interior one.

Regarding the specific shape of the orbits of this family, curiously, they look like the orbits of the first branch of the P3QSO family (Figure 5.5a), which is composed of EDS orbits, with an extra vertical loop as the source of the asymmetry. Additionally, it also resembles the shape of the EDS branch of the $P5QSO_1$ family (Figure 5.7d), but this time with one less exterior vertical loop. As for the general characteristics of each of these branches, they have the typical evolution of a high-energy family. So, the branches are unbounded and keep growing with no apparent limit. Both the energy and the period are monotonically increasing, but the period appears to reach a maximum value asymptotically. As for the linear stability, the beginning of the family is stable for both in-plane and out-of-plane motion. Nevertheless, at one point each of the stability indices become unstable, the in-plane one in the negative axis and with a fast increase of instability and the out-of-plane index in the positive axis with a much more limit growth. With the change from stable to unstable, the family crosses a tangent bifurcation for the out-of-plane index and a doubling-period one for the in-plane, but the families that may arise from these bifurcations are out of the scope of this work.

The next family is the $P6QSO_3$ presented in Figure 5.22. The characteristics of this family are really similar to those of the $P4QSO_3$ family. It is composed of asymmetric orbits with the two perpendicular crossings at the same side. It has two mirrored branches, one branch formed by UA orbits and the other with DA QSOs. The orbits are stable at the beginning of the family, starting from 'B', and then become unstable first for the in-plane motion, in which the instability grows rapidly, and afterward for the out-of-plane motion with a much slower

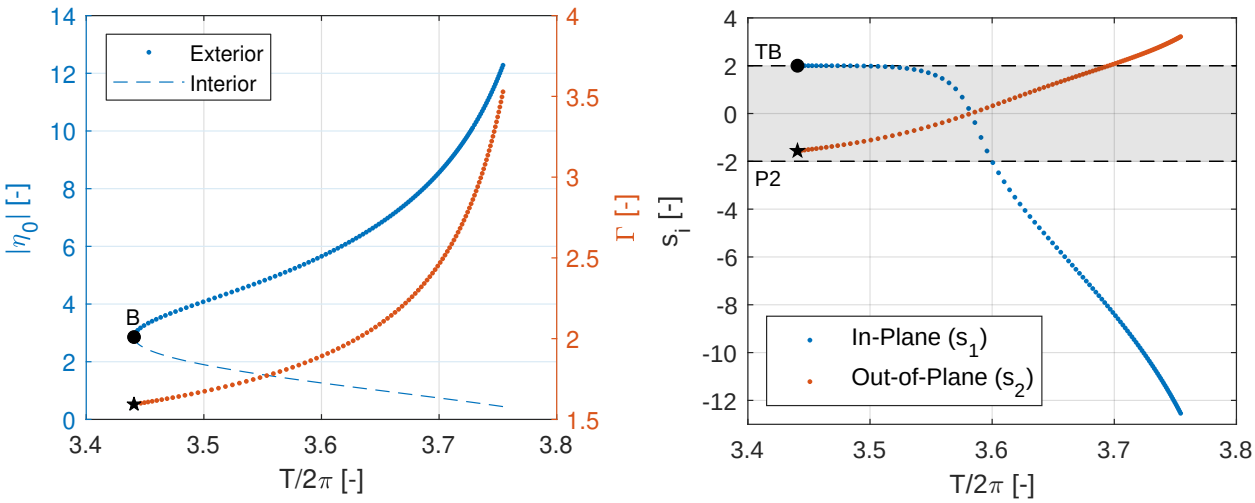

(a) Initial position and energy evolution

(b) Stability evolution

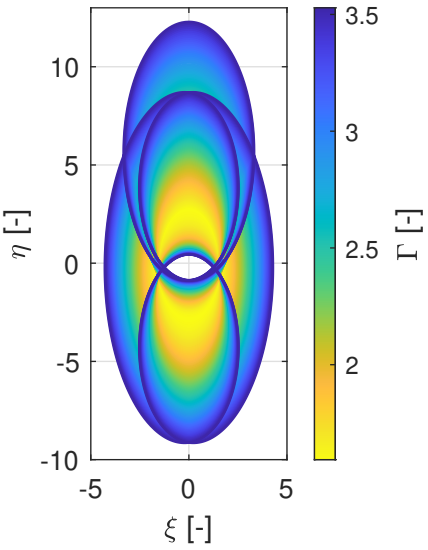

(c) UA branch

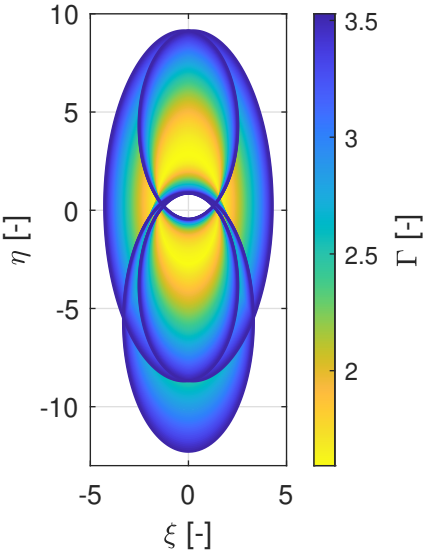

(d) DA branch

Figure 5.21: High-energy P4QSO$_3$ asymmetric family in the H3BP

growth rate. There is, however, one difference with respect to the P4QSO$_3$ family regarding the shape of the orbits. While the P4QSO$_3$ family is composed of orbits that resemble those of the EDS branches of the P3QSO and the P5QSO$_1$ families, the orbits of the P6QSO$_3$ family resemble the ones of the IDS branches of symmetric families. More specifically, they look like the IDS branch of the P5QSO$_1$ family (Figure 5.7e) with an extra vertical loop or like the IDS branch of the P7QSO$_1$ (Figure 5.10e) with one less vertical loop.

The final high-energy asymmetric family is the P7QSO$_5$ family shown in Figure 5.23. This family arises from one of the second-order period-septupling bifurcations of the QSO family. In particular, the same bifurcating orbit than the P7QSO$_3$ family. The initial position, the energy of the family and the period follow the same trend as the two previous families and the rest of high-energy families. In terms of the stability, the in-plane index has the same behavior

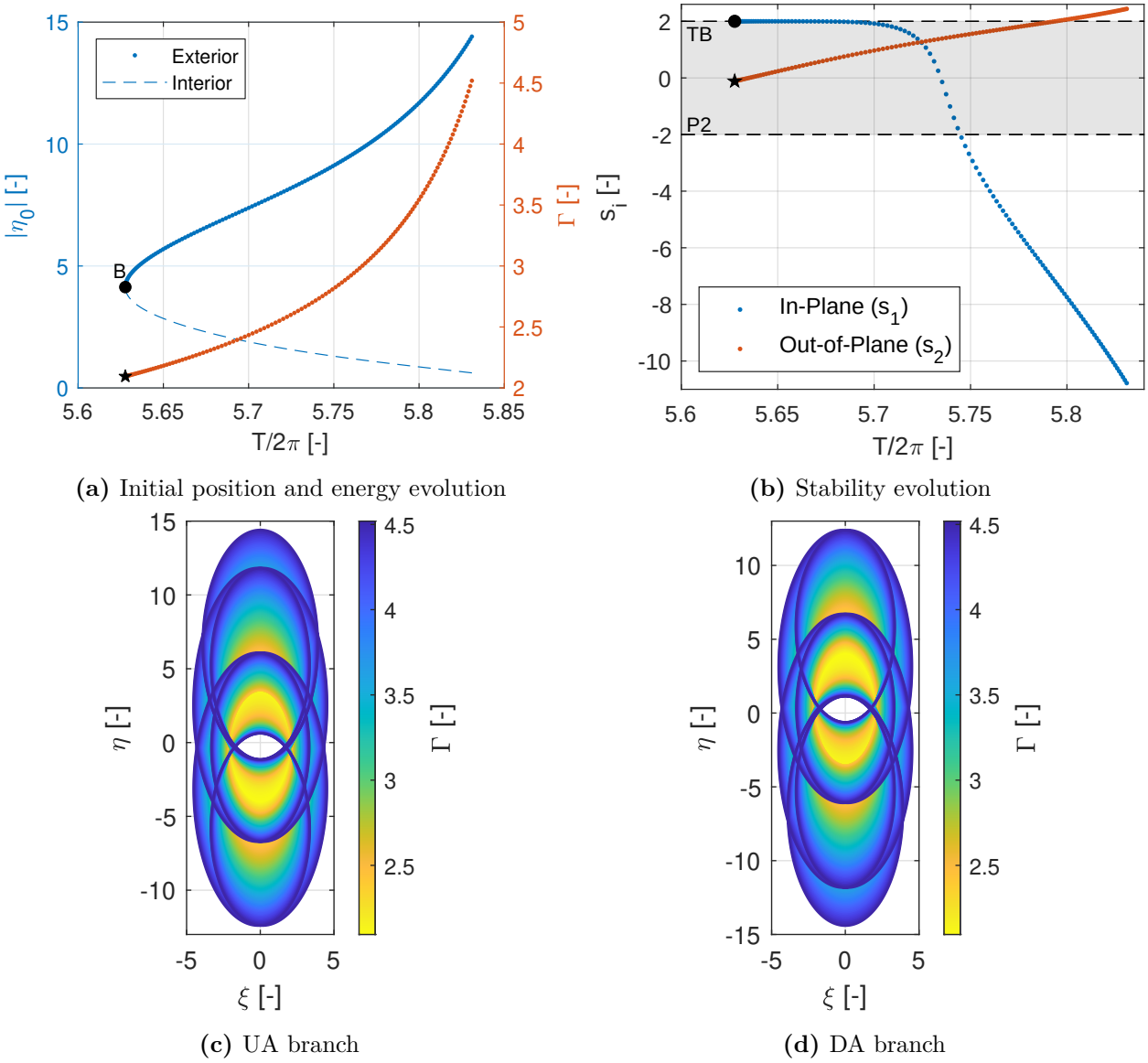

(a) Initial position and energy evolution

(b) Stability evolution

(c) UA branch

(d) DA branch

Figure 5.22: High-energy P6QSO$_3$ asymmetric family in the H3BP

as the other two high-energy asymmetric families, but the evolution of the out-of-plane one differs. While for the other two families this index increased monotonically, for this family it starts decreasing until it reaches a minimum in -2. After that, the index grows monotonically with a pretty high slope, leaving,at one point, the stable area. Finally, in terms of the shape, the orbits resemble a combination of the first EDS branch of the P3QSO family and the asymmetric P4QSO$_3$ family. This behavior is similar to the one experienced by the P7QSO$_3$.

Low-energy Families

The final group of planar orbits studied in this work is the one of the low-energy asymmetric families. Like what happened with the high-energy asymmetric families, there are three families that belong to this category. These families possess similar characteristics to those

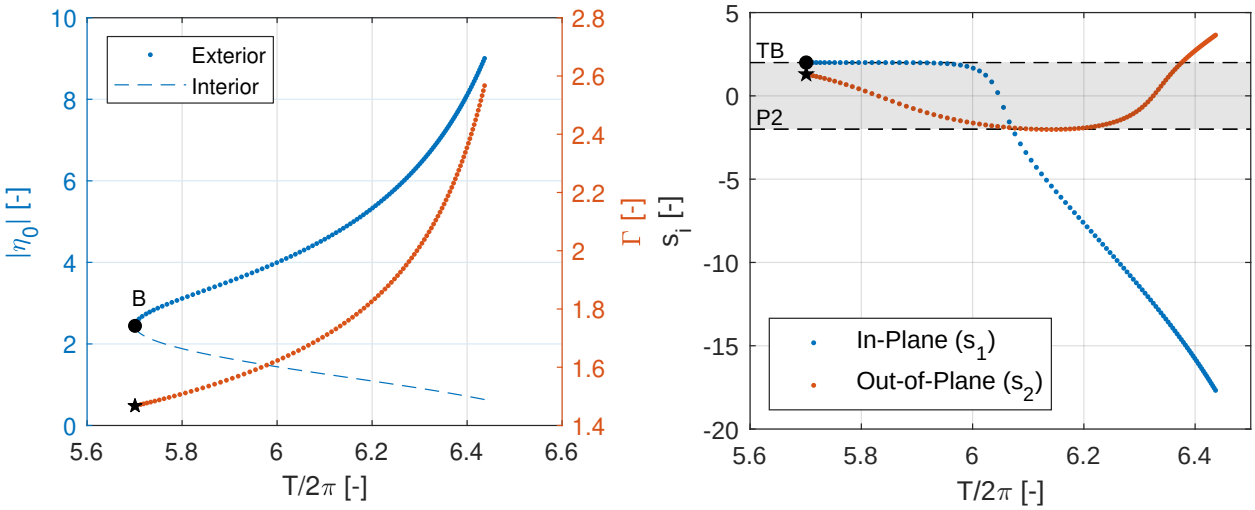

(a) Initial position and energy evolution

(b) Stability evolution

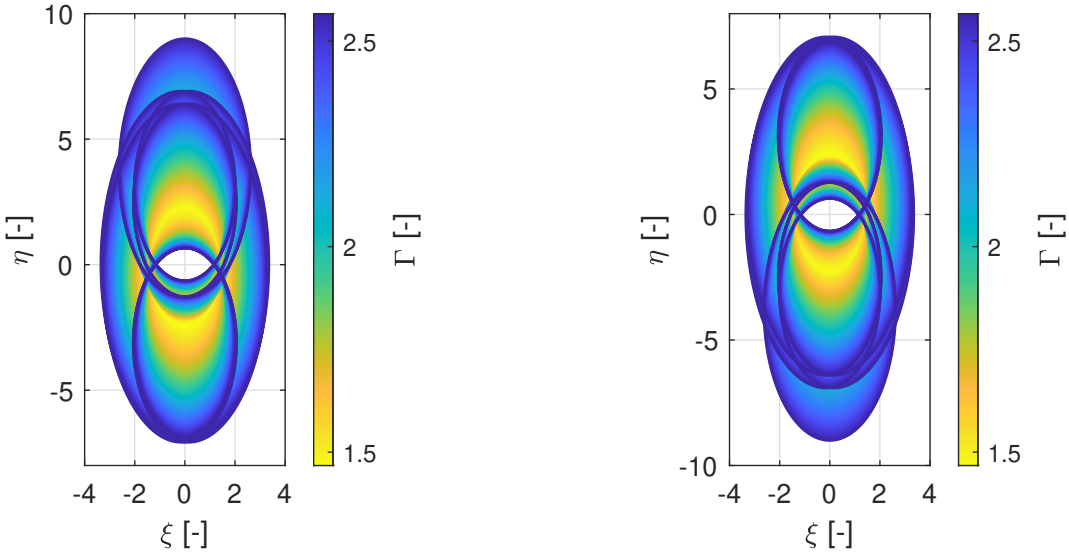

(c) UA branch

(d) DA branch

Figure 5.23: High-energy P7QSO$_5$ asymmetric family in the H3BP

of the symmetric low-energy families. They are upper-bounded in energy and period by the bifurcating orbit. However, while the symmetric families had collision orbits that led to mixed orbits, for the low-energy asymmetric families, this is not the case.

The first low-energy asymmetric family is the P4QSO$_4$, presented in Figure 5.24. As every other asymmetric family, it is composed of two branches that mirror each other with respect to the x-axis. Each orbit of this family has two perpendicular crossings placed on the same side of the y-axis, the positive side for the UA branch and the negative one for the DA. Due to the symmetry, both branches have the same exact characteristics and can be studied as a whole. The orbits of the family have a small size and a very rounded shape, with an aspect ratio of the orbits close to 1. As is characteristic of low-energy families, both the energy and the period of the branches decrease monotonically, starting from the bifurcating orbit.

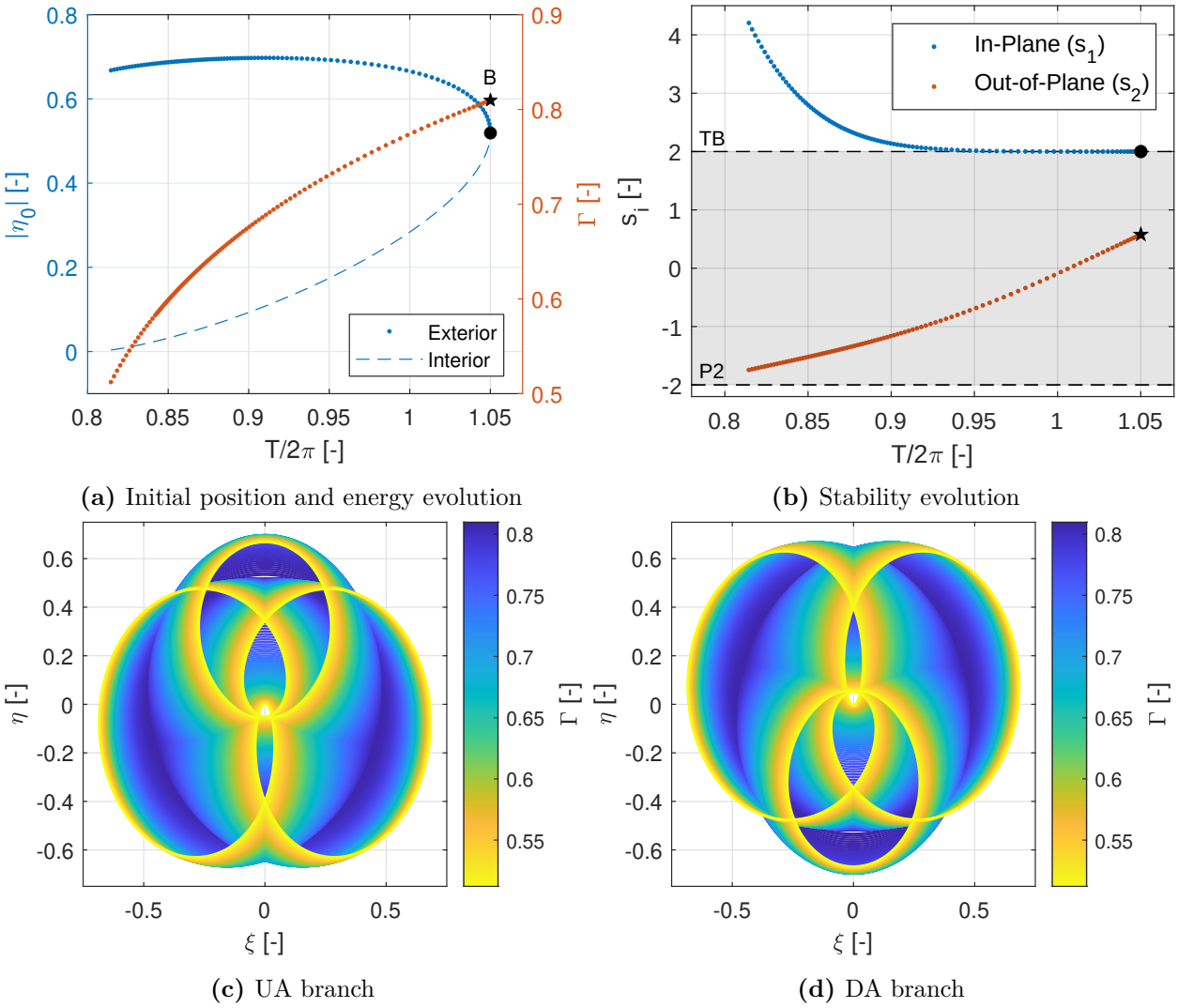

(a) Initial position and energy evolution

(b) Stability evolution

(c) UA branch

(d) DA branch

Figure 5.24: Low-energy P4QSO$_4$ asymmetric family in the H3BP

One characteristic that was common of all low-energy symmetric families, but that is not shared for the asymmetric ones, is the existence of mixed branches. While for the symmetric orbits at least one collision orbit existed and it was possible to continue beyond it, leading to mixed orbits. For this family that collision orbit is never reached. While the family evolves, the interior perpendicular crossing becomes closer to the second primary, but the collision is never reached as the continuation gets harder the closer the primary turns. The same situation took place for the symmetric orbits each time the perpendicular crossing became that close to the primary. Nevertheless, the difference in the fact that for the symmetric families, before this situation occurred, a collision orbit had already taken place thanks to a pair of non-perpendicular crossings. However, for the low-energy asymmetric families, the most interior crossing is the perpendicular one.

As for the stability, the orbits are unstable for the in-plane motion and stable for the out-of-plane one. Although the in-plane stability index is in the unstable area for all the

family (except for the bifurcating orbit that always has a value of 2), for most of the branch it remains really close to the 'TB' line and, even when it grows further from it, the instability remains controlled. Finally, the shape of the orbits of this family has a resemblance with the doubly-symmetric families. Specifically, they look like the orbits of the third branch of the P3QSO family (Figure 5.5c), with an extra vertical loop, or the ones of the EDS retrograde branch of the $P5QSO_2$ family (Figure 5.15a), without one of the exterior vertical loops.

The second low-energy asymmetric family is the $P6QSO_4$ family, shown in Figure 5.25. This family is very similar to the $P4QSO_4$, so, in general, everything that applied to that family can be applied here. The main difference lies in the in-plane stability index. Regarding the in-plane motion, the orbits are, being accurate, unstable, like in the $P4QSO_4$ family. However, this instability is almost despicable, as can be observed on (b). It is important to notice that in this figure the stability index represented is the b_i, instead of the hyperbolic one that was used in Figure 5.24b.

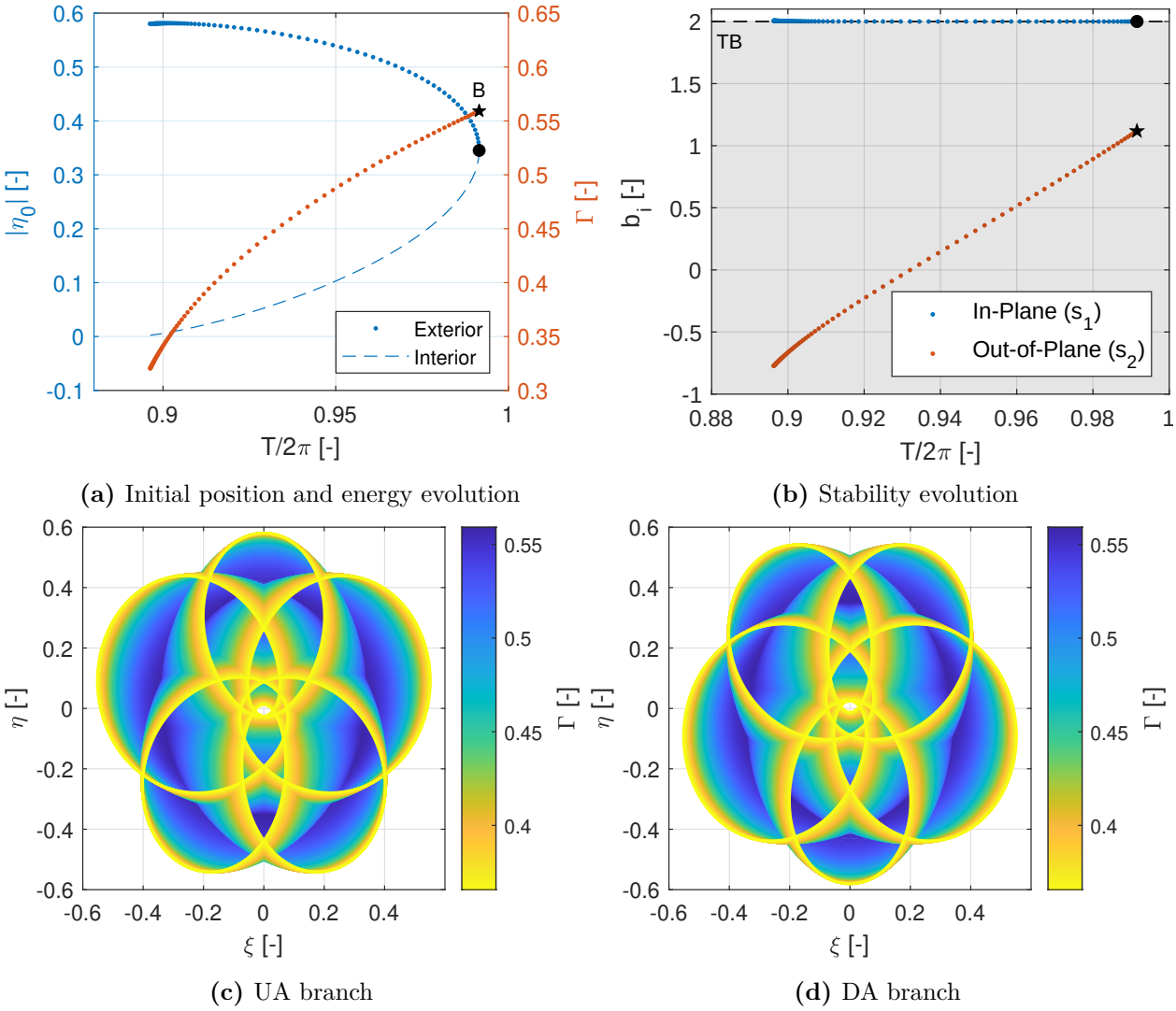

(a) Initial position and energy evolution

(b) Stability evolution

(c) UA branch

(d) DA branch

Figure 5.25: Low-energy $P6QSO_4$ asymmetric family in the H3BP

Finally, some comments are needed regarding the specific shape of the orbits. Like with the previous family, the shape reminds the one of the EDS branches of some of the symmetric families. More in particular, that of the P5QSO$_2$ family (Figure 5.15a) with an extra loop and that of the P7QSO$_2$ (Figure 5.18a) without one of the exterior vertical loops. Yet, this last added or subtracted loop deforms the shape of the orbit more than in previous cases, so this resemblance is more subtle. Another curious fact is that while for the high-energy asymmetric P6QSO$_3$ the orbits resembled IDS orbits, in here the similarity came from the EDS ones, like with the low-energy P4QSO$_4$ family.

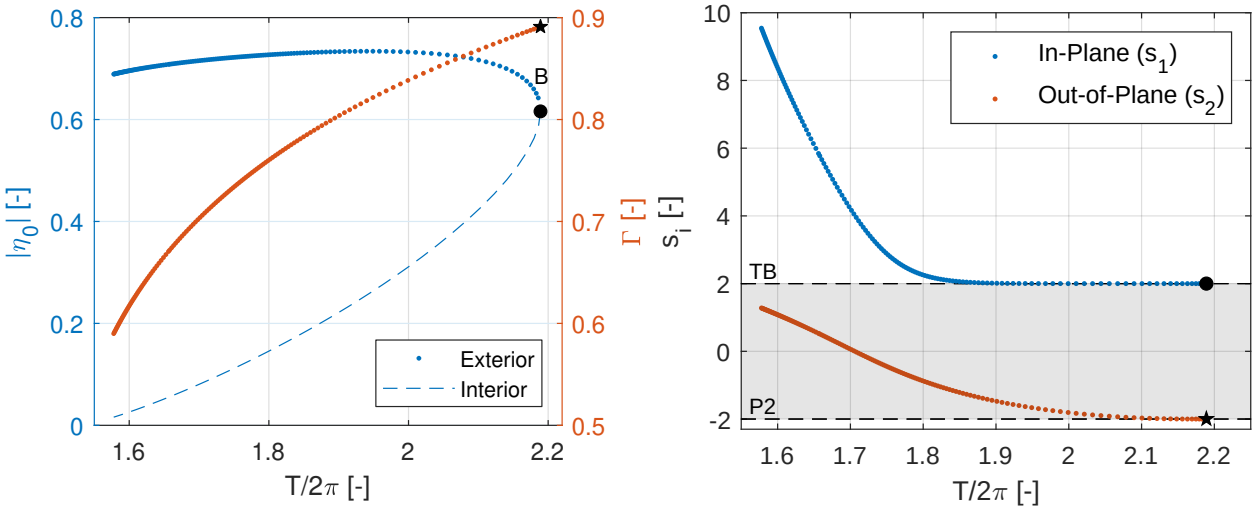

(a) Initial position and energy evolution

(b) Stability evolution

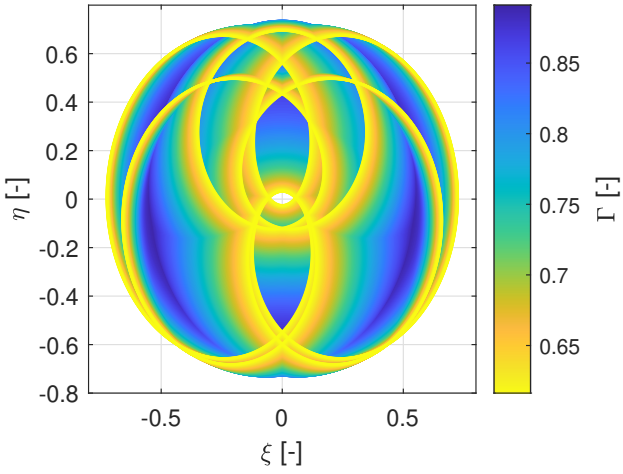

(c) UA branch

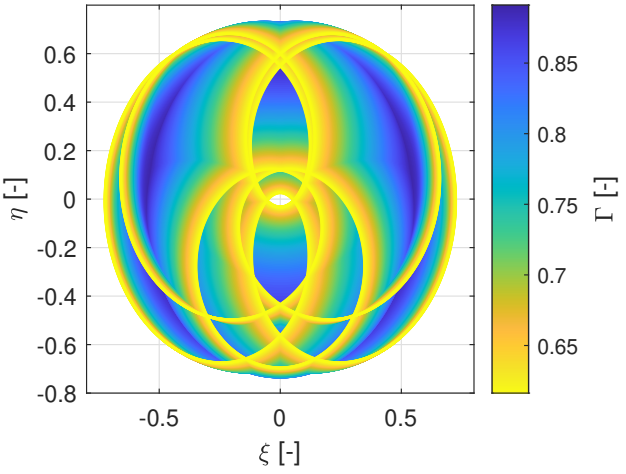

(d) DA branch

Figure 5.26: Low-energy P7QSO$_6$ family in the H3BP

The final asymmetric family is illustrated in Figure 5.26 and referred to as the P7QSO$_6$ family. Again, it shares the same characteristics as the other families in this section. One aspect that must be studied separately is the stability. The stability evolution of this family resembles that of the P4QSO$_4$ family, but reaches much higher in-plane instability values. As for the out-of-plane index, it increases instead of decreasing, starting from 'B', but without affecting orbital stability. However, it is noteworthy that for the 'B' orbit, not only does the

in-plane index have the expected value of 2, but the out-of-plane one also lies on a special line, specifically, the period-doubling one. Finally, as it is typical of orbits arising from a second-order period-septupling bifurcation, the orbit shape resembles a composition of a family of multiplicity 3 and another of multiplicity 4. Specifically, it seems like a composition of the third branch of the P3QSO family (Figure 5.5c) and the first asymmetric family of this section, the P4QSO$_4$ family (Figures 5.24c and 5.24d).

5.4 Families of 3D QSOs

Although this work focuses on planar QSOs, this section briefly analyzes the 3D QSOs families that arise from the steady QSO family by the bifurcations detected on the out-of-plane index in Figure 5.2c. This time, neither the period-tripling nor the period-quadrupling bifurcation lines are crossed, so the smaller multiplicity found is 5. In addition, the second-order period-septupling bifurcation line is not crossed either, leading to a 6 bifurcating orbits, again distributed in pairs. The 6 symmetric families of 3D-QSO that arise from these bifurcations are studied here. As in the planar case, the families can be subdivided into high-energy and low-energy families, to differentiate each member of the pair.

5.4.1 High-energy Families

The first high-energy family is the one coming from a period-quintupling bifurcation and it is called 3D-P5QSO$_1$ family. All the relevant characteristics of this family are shown in Figures 5.27 and 5.28. Among these, Figures 5.27a and 5.27b show the initial position, energy and stability evolution of the family, like it was done with all swing QSO families, but with two important differences. The first is related to the initial position of each orbit. As this family has 3D orbits, each perpendicular crossing to the x-z plane has two coordinates, ξ_0 and ζ_0. Nevertheless, for conciseness only the initial out-of-plane coordinate ζ_0 is shown in the plot. In addition, like with the planar symmetric orbits, the initial condition can be placed equally in any of the perpendicular crossings. For this specific family, the orbits are doubly-symmetric with respect to the 2D projection, as observed in Figure 5.28, so both perpendicular crossings have the same ζ_0. However, the family is z-asymmetric, so it has two branches, one composed by northern QSOs (Figure 5.28a) and the other with southern ones (Figure 5.28b). So, $|\zeta_0|$ is plotted in Figure 5.2a, representing both branches: the northern branch for positive ζ_0 values and the southern for negative ones. The second difference is that, this time, the stability indices cannot be separated in in-plane and out-of-plane motion as with the planar orbits.

In these two subfigures, it can be observed how the evolution of the family is much more complex than for the planar families, so only the most important characteristics will be commented. Among these, a key aspect is that while most of the family consist of highly unstable orbits, there is a portion where the orbits are stable or nearly stable. These occur at the beginning of the family, making them the most suitable as parking orbits.

In addition, to represent the evolution of the family, three different orbits have been marked. Their trajectory in the LVLH frame is shown in Figure 5.27c (in their northern version), while in Figure 5.27c the planar projection of their rotating angular momentum $\mathbf{h}$ is shown. This

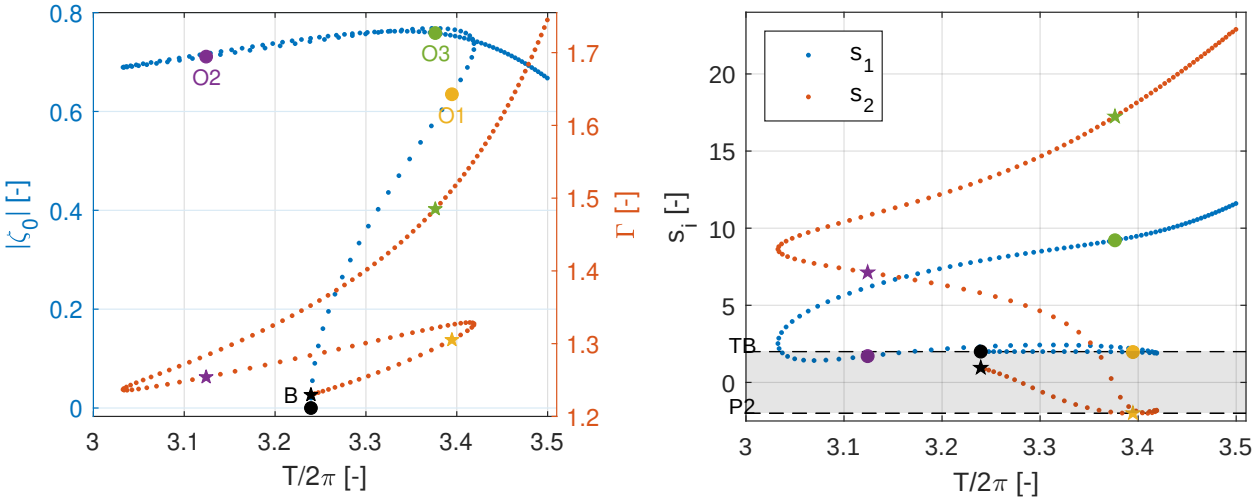

(a) Initial position and energy evolution

(b) Stability evolution

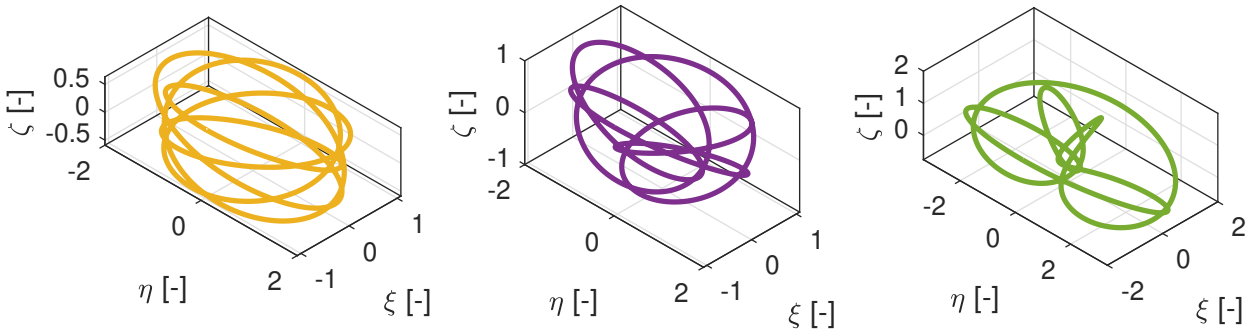

(c) Marked orbits

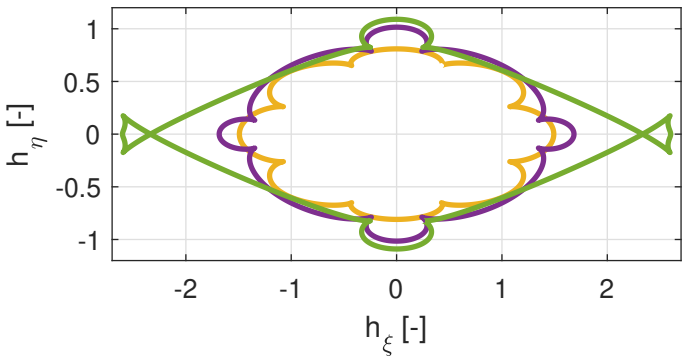

(d) Marked QSOs' rotating angular momentum

Figure 5.27: High-energy 3D-P5QSO$_1$ family in the H3BP

angular momentum is obtained with the Cartesian position and velocity in the LVLH frame, thus the "rotating" in the name. The yellow 'O1' orbit is placed at the beginning of the family. This orbit, composed by 5 loops, has a roughly "cylindrical" shape with negligible swing motion in its planar projection. Its angular momentum completes one retrograde revolution per period, with the $\xi - \eta$ projection consisting of 8 similarly sized arcs. The 'O2' orbit, in purple, is placed further in the family. Accordingly, the swing motion is more pronounced, and the arcs in the angular momentum projection vary in lenght. Finally, the green 'O3'